PERGAMON

Progress in Surface Science 61 (1999) 127–198

Progress in SURFACE SCIENCE

www.elsevier.com/locate/progsurf

Metal deposits on well-ordered oxide films

Marcus Bäumer*, Hans-Joachim Freund [1]

Fritz-Haber-Institut der Max-Planck-Gesellschaft, Abteilung Chemische Physik, Faradayweg 4–6, 14195 Berlin, Germany

Abstract

Metal oxide interfaces, metal coatings or dispersed metals on oxide supports play an important part in many technological areas. Nevertheless, there is still a lack of fundamental knowledge about the essential properties of thin metal films and small metal particles on oxide supports, although a deeper understanding could help to improve the electronic, mechanical or catalytic performance of such systems. In the past, a number of different approaches have been proposed and explored aiming at the preparation of suitable model systems. In this review, we discuss the possibility to use thin, well-ordered oxide films as supports for the study of deposited metal particles. This approach offers the advantage to permit the unrestricted application of all experimental methods, which rely on a good electrical or thermal conductivity of the sample, like PES, LEED, STM or TDS. With the help of several examples taken from our own work on a thin alumina film, we show that it is feasible to characterise such systems on a microscopic level with respect to all relevant structural, electronic and adsorption properties. In this way, correlations between these features can be established helping to understand the particular chemistry and physics of small metal aggregates.

Keywords: (Deposited) metal particles; (Deposited) metal clusters; Metal deposition; (Ordered) oxide films; Scanning tunneling microscopy; Spot profile analysis LEED; Transmission electron microscopy; Photoelectron spectroscopy; Infrared spectroscopy; Structure; Electronic structure; Adsorption

* Corresponding author. Tel.: +49-30-8413-4220; fax: +49-30-8413-4312.

E-mail addresses: baeumer@fhi-berlin.mpg.de (M. Bäumer), freund@fhi-berlin.mpg.de (H.-J. Freund)

[1] Tel.: +49-30-8413-4100/02/04; fax: +49-30-8413-4101.

0079-6816/99
PII: S0079-6816(99)00012-X

Nomenclature

AES	Auger electron spectroscopy
AFM	atomic force microscopy
BE	binding energy
CB	conduction band
CCT	constant current topography
ESR	electron spin resonance
HREELS	high resolution electron energy loss spectroscopy
HRTEM	high resolution transmission electron microscopy
IR(A)S	infrared reflection (absorption) spectroscopy
ISS	ion scattering spectroscopy
KE	kinetic energy
LEED	low energy electron diffraction
ML	monolayer
PE	photon energy
PES	photoelectron spectroscopy
SPA-LEED	spot profile analysis of LEED spots
SPM	scanning probe microscopy
STM	scanning tunneling microscopy
TDS	thermal desorption spectroscopy
TED	transmission electron diffraction
TEM	transmission electron microscopy
UHV	ultrahigh vacuum
UPS	ultraviolet photoelectron spectroscopy
VB	valence band
XAS	X-ray absorption spectroscopy
XPD	X-ray photoelectron diffraction
XPS	X-ray photoelectron spectroscopy

Contents

1. Introduction

The structure and properties of small metal particles represent a field of research which has attracted a lot of attention during the last years. As an intermediate state of matter between atoms in the gas phase and the solid state, they often exhibit exceptional physical and chemical properties. While these properties are essentially determined by aggregate size in the case of free unsupported clusters, for deposited systems the interaction with the substrate can play an important part as well, modifying, changing or strengthening certain features.

One of the areas where deposited metal particles are technically employed to a large extent is heterogeneous catalysis. Here, a catalytically active component,

such as a transition metal, is dispersed over a suitable support material, usually an oxide like alumina or silica. In the first place, this is done in order to achieve the highest possible surface area of the active phase. Because of the high degree of dispersion, however, particle-size effects, originating from specific structural or electronic features and metal substrate interactions can influence the catalytic behaviour significantly. Of course, it has always been a central question in catalytic research as to how these effects can be exploited to improve the catalytic activity or the selectivity of a supported catalyst [1].

Nevertheless, there is still only very limited fundamental knowledge about the relationship and the interplay between structure, adsorption behaviour and chemical or catalytic activity of small deposited metal aggregates. Since the complex structure of real catalysts often hampers the attempt to connect macroscopic effects with the microscopic processes taking place on the surface, an increasing number of model studies have been conducted so far to tackle these questions. One approach comes from *ultrahigh vacuum* (UHV) surface science aiming at an understanding of the elementary steps involved on a microscopic level. For studies of that kind planar substrates, instead of the technically used porous materials, are needed in order to take full advantage of modern surface spectroscopic and microscopic techniques.

Recently, a number of excellent reviews concerning this 'surface science approach' have been published taking a critical look at the different strategies to compose and explore model catalysts [2–7,189,190,254]. The spectrum ranges from studies based on polycrystalline or amorphous oxide substrates [2] to investigations on oxide single crystals or well-ordered films [5–7,189,190,254]. Also with respect to the preparation of the particles, different concepts have been proposed. One approach is to apply techniques which come as close as possible to industrial catalyst manufacture, such as wet impregnation or exchange in solution [2]. Unfortunately, this often involves the disadvantage that structure and morphology of the deposits are rather difficult to control, though. Thus, vapour deposition of metals [4,7,190] or deposition of metal clusters from the gas phase [8] under UHV conditions have been preferred in experiments keyed to more fundamental questions about the correlation between structure and properties of small metal particles.

In these cases, also well-ordered substrates are desirable. The most straightforward choice in this context are single crystal samples of course. Studies of bulk oxides, however, can be connected with severe experimental problems. Their insulating character can restrict or even prevent electron and ion spectroscopic, as well as *low-energy electron diffraction* (LEED) and *scanning tunneling microscopic* (STM) measurements. Only in cases where the oxide can be made sufficiently bulk conducting (e.g. TiO_2), this limitation may not apply [6,189]. Other difficulties encountered are related to sample mounting and cleaning (adjustment of surface stoichiometry) or arise from the poor thermal conductivity associated with oxide materials.

In this context, ultra-thin oxide films grown on a metallic substrate are an excellent alternative in order to circumvent all these problems [5,7,190,254]. It has

been shown that even films with a thickness of just a few Ångstroms can exhibit physical properties characteristic of the bulk material [9]. The traditional method to prepare such films is the oxidation of the native metal [9], although this often results in amorphous or polycrystalline overlayers (e.g. Al_2O_3 on Al [10,11,191,255], or SiO_2 on Si [12,192]) or films with a rather high defect density. This is due to the large mismatch which usually exists between the metal and the oxide lattice (e.g. NiO(100)/Ni(100) [13]). There are only a few examples where well-ordered crystalline films can be obtained in this way (e.g. Cr_2O_3(111) on Cr(110) [14,193,256]).

Therefore, other routes have been proposed. Goodman et al., for example, extensively explored preparation techniques based on the evaporation of a metal (or non-metal) onto a host crystal, mostly a refractory metal, in an ambient oxygen atmosphere [5,15,254]. Another promising possibility is the oxidation of a suitable alloy sample containing the metal which should be oxidised. A well-known example of that kind is the formation of well-ordered thin alumina films on the low index surfaces of certain Al alloys [16–22,194]. However, it is likely that this approach also works in other cases [23].

An overview of some well-ordered thin oxide films described in the literature can be found in Table 1. Here, all three types of preparation have been considered. Although a lot of effort has been undertaken to make thin oxide films of high quality, structural flaws can sometimes occur. As shown in Table 1, the two most frequently observed imperfections are holes in the film where the metallic substrate is exposed or limited long-range order. One of the examples not featuring these problems is the system Al_2O_3/NiAl(110) [16,17]. This thin alumina film is exceptionally well-ordered and can be reproducibly prepared with a thickness of just 5 Å. It grows with a structure, including the defect structure, which is rather uniform and only subject to minor variations with respect to different samples and slightly different preparation conditions.

The central question now is what can be learnt about the basic properties of small deposited metal particles by means of a model system such as the one depicted in Fig. 1. In this article, we try to give an answer by taking some examples from our recent work. Our intention is not to present a complete overview of this field but to give the reader an idea of the potential of this approach to provide information about particle-size effects and the role of metal–support interactions. It should become evident, for example, how such investigations can be conducted in order to decide whether certain adsorption phenomena have their origin in specific electronic or structural features of the small aggregates.

The review is organised as follows. In Section 2, experimental techniques for the characterisation of such model systems will be described with respect to the benefits resulting from the employment of thin well-ordered oxide films. Section 3 deals with the structure of the thin alumina film grown on NiAl(110) already mentioned. Because of its structural virtues, it was used as a support for all case studies discussed in the following sections. For these studies, particle ensembles were generated by vapour deposition of the corresponding metal. Section 4

Table 1
Ordered thin oxide films grown on metal substrates and exhibiting a LEED pattern (MBE growth techniques not included, D: thickness)

System	Preparation	D (Å)	Possible problems	Refs.
MgO				
MgO(100)/Mo(100)	$Mg + O_2$ at 200–600 K		[a]	[24,25,195,196]
MgO(100)/Mo(100)	$Mg + O_2$ at 300 K	25	film grows in domains[a]	[26]
MgO(100)/Ag(100)	$Mg + O_2$		mosaic structure	[27]
MgO(111)/Mo(110)	$Mg + O_2$ at 300 K, ↑ 800 K	∽ 50		[28]
Al_2O_3				
Al_2O_3/NiAl(110)	O_2 at 550 K, ↑ 1100 K	5		[16,17]
Al_2O_3/NiAl(100)	O_2 at 300 K, ↑ 1200 K	∽ 10	amorphous Al_2O_3 areas	[18,29,194]
Al_2O_3/NiAl(111)	O_2 at 300 K, ↑ 900–1100 K	∽ 15		[19]
Al_2O_3/Ni_3Al	O_2 at 900 K	∽ 5		[20,21]
Al_2O_3/FeAl	O_2 at elevated T	5–8	some lateral disorder	[22]
Al_2O_3/Re(0001)	$Al + O_2$ at 970–1170 K	> 16		[30]
Al_2O_3/Re(0001)	Al, O_2 at 970 K	5–20	thick films: some disorder	[31]
Al_2O_3/Ta(110)	$Al + O_2$ at 900 K	5–40		[32]
Al_2O_3/Mo(110)	$Al + O_2$, ↑ 1200 K in O_2	4–20	some degree of disorder	[33]
Al_2O_3/Ru(0001)	$Al + O_2$ at 1170 K	25	some degree of disorder	[30]
NiO				
NiO(100)/Ni(100)	O_2 at elevated T, annealing	∽ 50	high degree of disorder	[13]
NiO(111)/Ni(111)	O_2 at elevated T, annealing	∽ 50		[34,197]
NiO(111)/Au(111)	$Ni + O_2$ at 573 K	∽ 5		[35]
NiO(100)/Mo(100)	$Ni + O_2$, annealing in O_2			[36]
Fe_2O_3				
FeO/Pt(111)	Fe, O_2 at 900 K	∽ 5		[37,38,198]
Fe_2O_3/Pt(111)	Fe_3O_4, O_2 (1 Torr) at 1100 K	∽ 100		[37,39,199]
Fe_3O_4/Pt(111)	Fe, O_2 at 900 K	∽ 100		[37,40,200]
CoO				
CoO(100)/Co(100)	O_2, annealing	∽ 20	some degree of disorder	[41]
TiO_2				
TiO_2/Pt(111)	Ti, O_2 at 573 K, annealing		holes	[42]
ZrO_2				
ZrO_2/Pt(111)	$Zr + O_2$, annealing in O_2		high degree of disorder	[43]
Cr_2O_3				
Cr_2O_3/Cr(110)	O_2 at elevated T, annealing	∽ 50		[14,193,256]

[a] The MgO films may contain a higher defect density as compared to MgO single crystals. This suspicion has been put forward by CO TDS experiments on vacuum cleaved MgO crystals. These show no CO adsorption above 90 K. The films, however, give rise to a desorption peak at about 120 K [44].

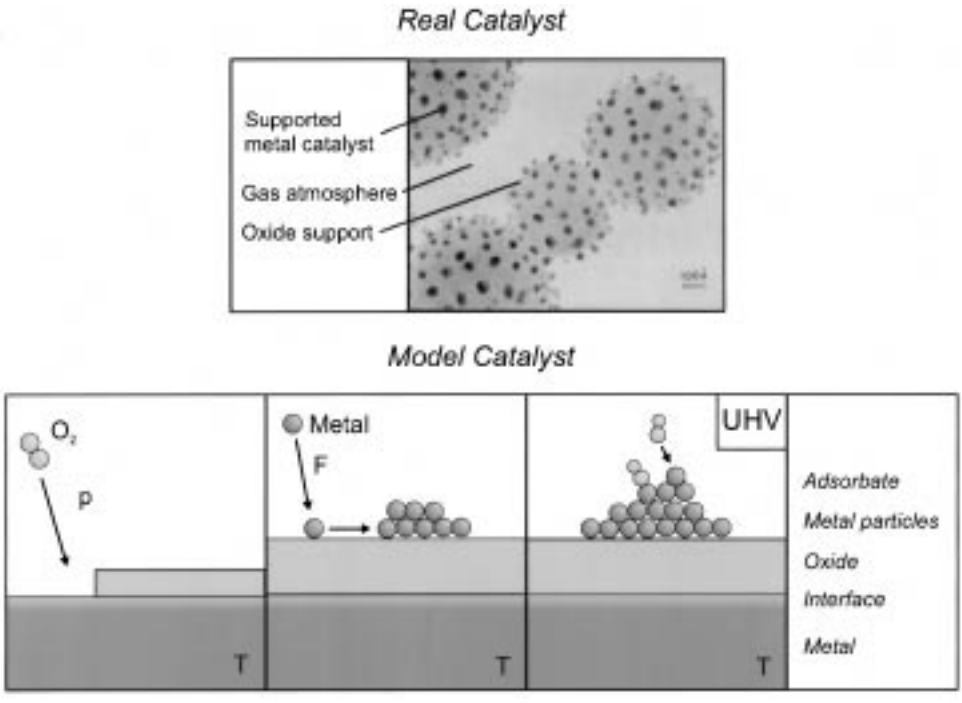

Fig. 1. Supported metal catalyst: real and model system (T: temperature, p: partial pressure, F: flux).

provides a survey of the structure and morphology of the systems obtainable in this way, including the growth behaviour at different temperatures, the thermal stability and the growth in ambient gas atmospheres. The subject of Section 5 is the electronic structure of the deposits. Finally, adsorption and reaction of CO as a probe molecule will be dealt with in Section 6.

2. Experimental details

In Sections 2.1–2.5, some experimental details will be discussed, which are of relevance if standard surface science techniques, such as LEED, STM and *photoelectron spectroscopy* (PES), are applied to small deposited particles and thin oxide films. Furthermore, we will also briefly comment on the use of *transmission electron microscopy* (TEM) and *infra-red reflection absorption spectroscopy* (IRAS) for the characterisation of such systems.

2.1. Profile analysis of low energy electron diffraction spots

Since the first studies in the sixties and seventies, the *spot profile analysis* of LEED (SPA-LEED) beams has developed into a technique which can be

extremely useful for the characterisation of surface defects. In this context, we refer the reader to a number of reviews explaining in more detail the relationship between certain defect structures such as steps, facets, mosaics, domains and the resulting spot profile on the other hand [45,46,201,202]. A description of the SPA-LEED instrument can also be found in the literature [47].

The case of a deposit on a well-ordered substrate represents a situation of an 'inhomogeneous surface', where we have areas with different scatterers A (substrate) and B (adsorbate) distributed over the surface [48]. Generally speaking, three scenarios have to be distinguished: (a) two-dimensional (2D) islands, (b) three-dimensional (3D) ordered aggregates exhibiting steps and terraces and (c) three-dimensional disordered particles. These situations are schematically depicted in Fig. 2.

It has been shown that an arrangement of type (a) gives rise to a spot profile consisting of a central peak at the Bragg position and a broad 'diffuse' shoulder, representing the Fourier transform of the island pair correlation, i.e. the probability to find two islands at a certain distance [48]. In this context, it is important to note that the *shape* of the diffuse shoulder is independent of the scattering factors f_A and f_B involved [48]. Case (b) is more complicated than (a), because the second and following adsorbate layers cause additional contributions to the diffuse shoulder [49,203]. At electron energies, however, where all layers scatter in-phase (so-called *in-phase energies*), these contributions vanish due to constructive interference. Consequently, the arrangement can be described with a two-layer model under these circumstances as well: one layer being the substrate and one layer being the adsorbate covered areas. Finally, disordered or amorphous areas on a surface usually cause a diffuse background in the diffraction pattern so that for the purpose of the spot profile analysis they can be

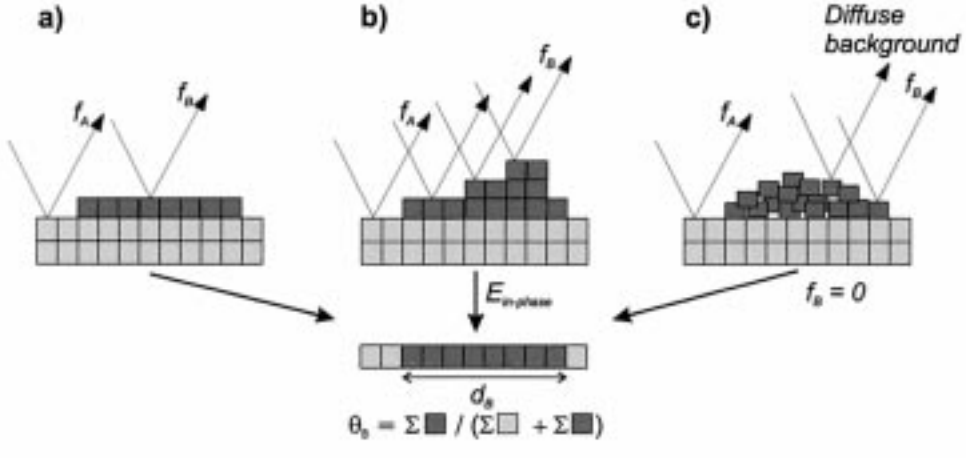

Fig. 2. Schematic drawing of the three situations encountered in the case of deposited particles on an ordered substrate (commensurate systems, explanations in the text).

regarded as 'black holes'. Therefore, the third situation (c) is often also identical to (a) assuming that $f_B = 0$.

The LEED profiles recorded for such systems now contain valuable information about their structure. Provided for example that $f_A \gg f_B$, the portion of the substrate covered with islands is easily obtainable from the intensity of the central peak: $I_{Peak}/I_{Total} = 1-\theta_B$, with $I_{Total} = I_{Peak} + I_{Shoulder}$ [48,50]. If this condition is not met but the adsorbate does not scatter into the beams of the substrate (non-epitaxial growth), it is alternatively possible to get the coverage θ from the damping of the substrate spots: $\theta_B = 1 - (I/I_0)^{0.5}$, with $I_0 = I(\theta = 0)$.

Another source of information can be the energy dependence of the profiles. As already indicated, 3D ordered aggregates give rise to an energy dependent behaviour, due to in-phase or out-of-phase scattering between adjacent adsorbate layers. Typically, this is connected with variations of the halfwidth of the shoulder (minimum: in-phase energy, maximum: out-of-phase energy). From the corresponding in- and out-of-phase energies, the interlayer distance d is directly inferable [45,201,202]. Of course, the formation of large crystallites may finally lead to extra spots in the LEED pattern as well.

Moreover, it is advantageous to check the shape of the LEED spot. Since the diffuse shoulder depends on the island arrangement, an anisotropic shoulder also reveals an anisotropic spatial distribution of the adsorbate islands.

Apart from a qualitative analysis, also a quantitative evaluation of the profiles is possible providing statistical parameters like the mean island size and mean island distance as schematically illustrated in Fig. 3. In order to enable a 1D treatment of the problem, the 2D intensity distribution of the beam (which has to be isotropic for this purpose!) has to be subjected to a 1D integration first. In this way, a profile is obtained which corresponds to the Fourier transform of the 1D pair correlation along straight lines on the surface (see Fig. 3). The only additional parameter needed for the calculation is the fraction of the surface covered by islands. With some assumptions, the diffuse shoulder for a 1D problem can be easily calculated, even for arbitrary size distributions, as described in the literature [51,204]. By means of such a formalism, the way is now open for a quantitive analysis of the data by calculating profiles from suitable model size distribution functions and comparing them to the experimental results. Using a fitting algorithm, the parameters of the distribution functions can be varied until the best agreement between experiment and theory is achieved. It is important to note though that the island diameters determined by this procedure will deviate from the real diameters. Because of the 1D treatment, all possible cuts through the islands, also those not going through the centre (see Fig. 3), are considered, resulting in a mean island length which is too small. This error, however, can be properly corrected.

2.2. Scanning tunneling microscopy

STM is a technique which has been very successfully employed to study the structure and topography of surfaces down to atomic dimensions [52,205]. Of

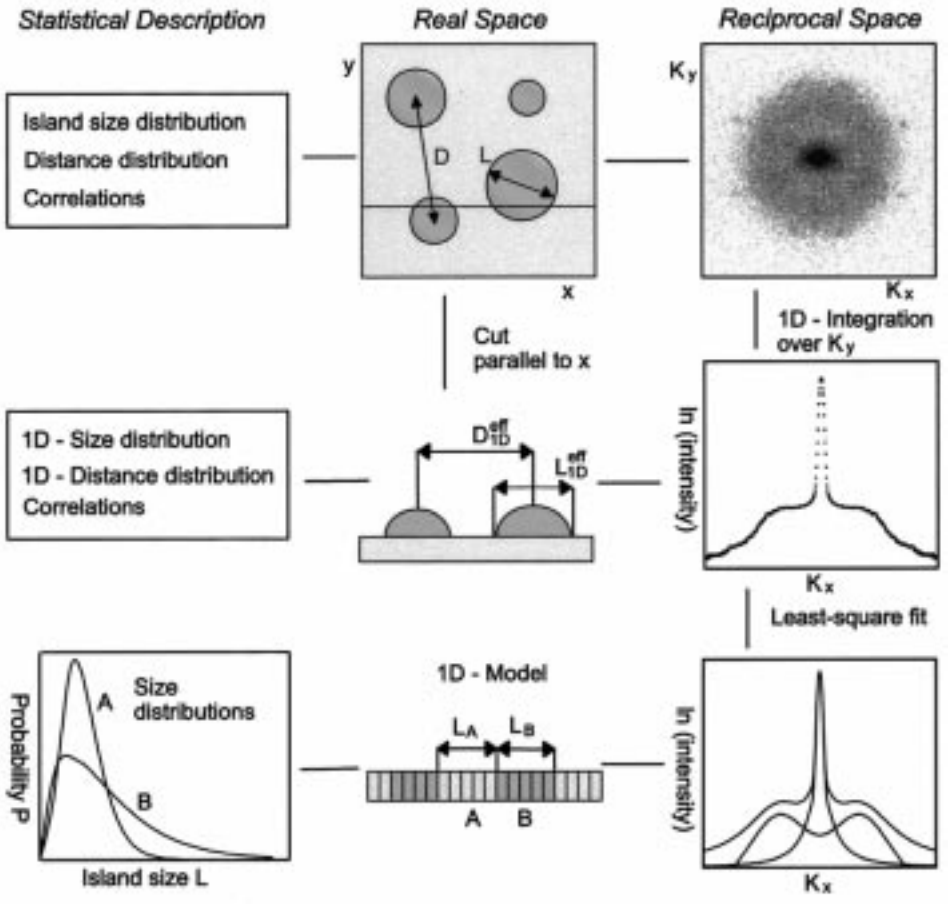

Fig. 3. Diagram illustrating the LEED spot profile analysis for a two layer system: adsorbate islands B on a substrate A. This scheme is valid for commensurate and incommesurate systems. In the latter case, however, only for the specular beam.

course, its mode of operation relies on the electrical conductivity of the samples. Therefore, the vast majority of investigations has been carried out on metal and semiconductor surfaces. Nevertheless, it has been shown that STM studies on oxide samples are feasible, if the material can be made sufficiently bulk conducting (like TiO_2) [53,54]. As pointed out in Section 1, another approach is the use of thin-oxide films on metallic substrates. In this case, the composite structure involves some particularities with respect to the tunneling conditions, which ought to be explained here [17,26,55,206].

Due to the band gap of the oxide, we have to distinguish between two situations illustrated in Fig. 4, by means of potential diagrams. At low bias

voltages U, electronic states of the oxide (VB: *valence band*, CB: *conduction band*) are not accessible, so that the electrons can only tunnel between the tip and the metal support. In this case, the oxide just modulates the potential barrier as a function of position, possibly giving rise to a weak contrast in the STM picture. Generally speaking, however, it must be kept in mind that, under these conditions, STM is more sensitive to the topography at the *film–substrate* interface.

In contrast, the electrons can tunnel directly into or out of oxide states at higher bias voltages beyond the band gap. Then, STM is more sensitive to the *vacuum–overlayer* interface and it is expected that the data provide information about the topography of the insulating film itself. This effect is clearly demonstrated in Fig. 4, where *constant current topography* (CCT) images of the alumina film on NiAl(110) are presented [55,206]. At voltages below 4 V (the band gap of alumina is about 7–8 V, see Section 3), no change of the tip height is

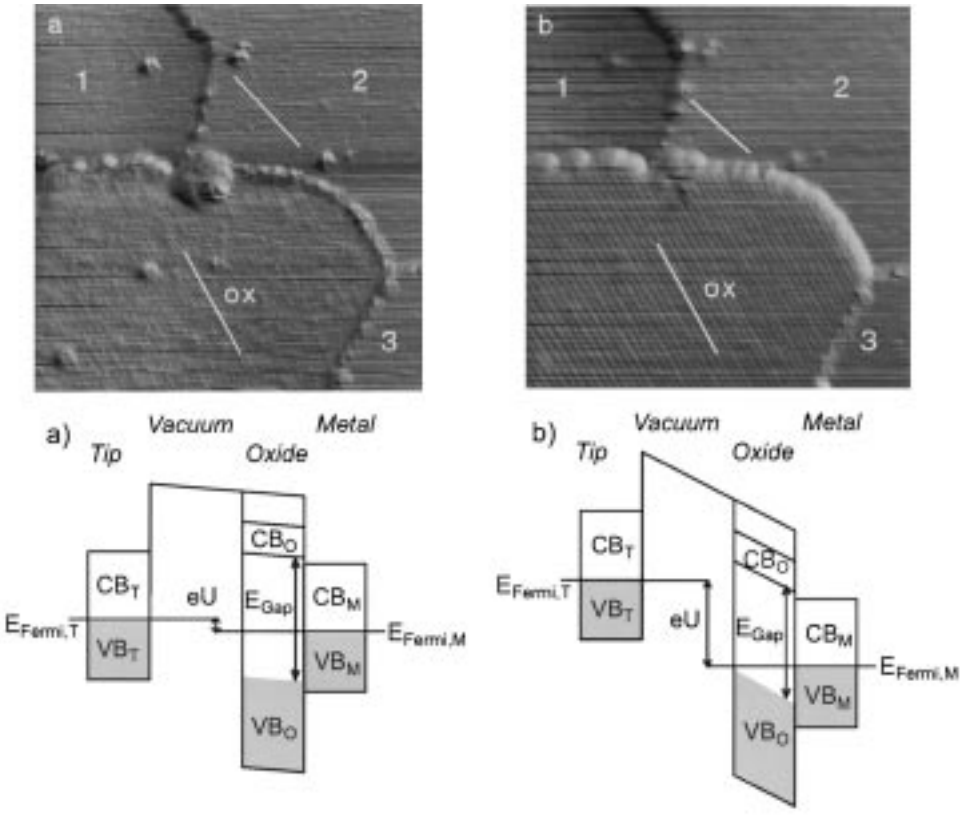

Fig. 4. STM (CCT, 500 × 500 Å) images of an Al_2O_3 island (ox) on NiAl(110) (areas: 1, 2, 3) taken at (a) $U = 0.4$ V and (b) 4 V [55,206]. The potential diagrams elucidate the different tunneling conditions.

detected when moving between an Al_2O_3 island and the bare NiAl substrate. But, upon raising the voltage above 4 V, an image is obtained which shows the island with an apparent height of 3.5 Å with respect to the metal support.

Although considerations of this kind are generally sufficient to interpret STM data from thin-oxide films, a third imaging mode operative at *low* bias voltages sometimes comes into play, probing the *topography of the film* rather than the interface [56]. This happens if the tip comes very close to the surface, so that repulsive forces between tip and surface become important for the imaging process. As shown in the next section, a very sharp contrast and large corrugations are attainable in this way.

If such thin-oxide films, such as the system Al_2O_3/NiAl(110), are used as a support for small metal particles and clusters, a number of interesting questions can be dealt with. First of all, the *morphology of the aggregates* can be studied in detail:

- Do they exhibit a crystalline structure or are they disordered?
- What faces are exposed, provided they are crystalline?
- What is the overall shape?

Apart from the deposit, it is also interesting to have a look at possible *modifications of the substrate*:

- Is the structure of the oxide modified in the vicinity of the deposit pointing to direct metal support interactions?

Last, but not least, it is, of course, also possible to extract *statistical data* about particle sizes and heights, although this kind of information is much harder to get as compared to methods directly providing average values, such as SPA-LEED, for example.

In spite of the fact that STM, in principle, is capable of scanning structures with atomic scale resolution, it is often difficult to reach this standard in the case of deposited particles. Consequently, some of the questions raised above may, in practice, not be answerable. The reason for this is the comparatively large overall corrugation of these systems, which usually precludes the imaging of atomic corrugations under the continuously changing tunneling conditions.

Another issue to be mentioned in this context concerns the influence of the tip on the measured particle shape [57]. Due to the finite tip size, it has to be taken into account that the particles may be noticeably smeared out in the STM image. Naturally, this effect is more drastic the larger the diameter of the tip apex and the larger the overall corrugation of the system. In Fig. 5, an example is presented which illustrates the problem [58]. While recording the two STM pictures shown, a sudden tip change occurred in both cases nearly at the same position. Obviously, the first modification resulted in a larger tip apex: increased particle diameters are observed now and the deposit seems to cover a larger fraction of the support (see line scans). After the second change obviously connected with a reduction of the apex diameter, the particles appear to be smaller again. The schematic diagram in Fig. 5 helps to envision this effect more clearly and to

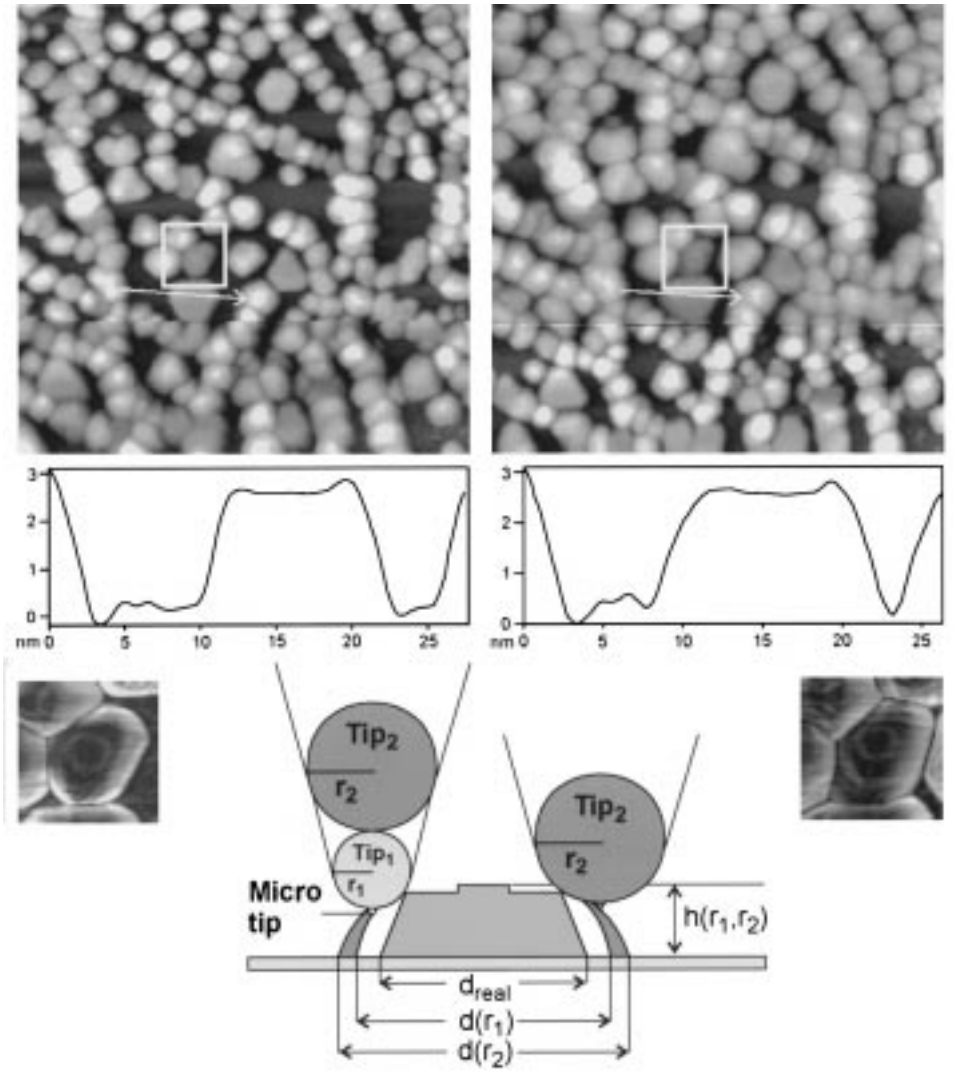

Fig. 5. STM data (CCT images, line scans, close ups) showing the influence of different tip radii r on shape and diameter d of small deposited particles ($Rh/Al_2O_3/NiAl(110)$, 1000 Å × 1000 Å). As shown in the schematic drawing, *d* is dependent on *r*; the height *h* and the resolution on flat areas, however, is unaffected.

understand that it has nothing to do with the resolution on a flat surface. With the help of a micro tip, even a large tip can resolve atomic steps, as proven by the two close ups in Fig. 5, showing an ad-island on the top of an aggregate which is resolved in both cases.

2.3. Transmission electron microscopy

TEM is perhaps the most often applied microscopic technique in heterogeneous catalysis for the structural characterisation of supported-metal catalysts [59,207]. In the same way, it also plays an important part in investigations of model catalysts (see some recent reviews [2,3,60]). It has, for example, been very successfully employed in studies concerning the nucleation and growth of metals on oxides (determination of particle sizes, densities). Other aspects, however, are perhaps even more attractive and unique: on the one hand, the *internal structure* and epitaxy of deposited aggregates are accessible, i.e. lattice parameters of individual crystallites and epitaxial relationships can be relatively easily determined either by *high resolution* images (HRTEM) or *transmission electron diffraction* (TED). On the other hand, it is possible to study *particle morphologies* (shape, exposed facets, contact angles with the substrate) in detail by means of HRTEM profiles (direct transmission in different directions) or *weak beam dark field imaging* (WBDF) (see Ref. [61]).

Therefore, TEM is certainly a very powerful technique, due to its extraordinary resolution capabilities, but it also has some disadvantages if compared to STM or SPA-LEED, for example. One of them is the ex situ character, i.e. the samples usually have to be transferred into the microscope through air involving the danger of structural changes of the deposits. Another problem could be radiation damage in case of very sensitive oxide samples [62].

In Fig. 6 a schematic drawing is presented showing how to prepare a thin-oxide film support for a TEM analysis [63,64] (see Ref. [2] and references therein for further preparation techniques). After growing the film and depositing the particles, the sample is ion-milled from the back, so that a small hole is finally formed. In this way, a wedge is obtained, which is thin enough for the imaging process. A positive side effect of this procedure is the fact that the unsupported film next to the edge can also be studied. This opens the opportunity to judge whether the metal substrate has any structural effect on the deposits [63].

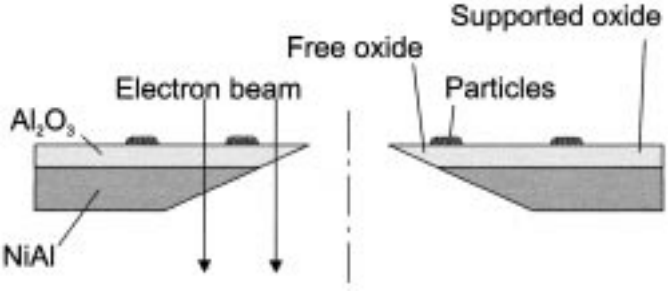

Fig. 6. Schematic drawing of a thin film support prepared for a TEM investigation [63].

2.4. Photoelectron spectroscopy

As already alluded to in the introduction, the transition from a single atom to an extended metal crystal involves drastic changes of the electronic structure, which are schematically illustrated in Fig. 7 with respect to a photoemission experiment [65]. On the one hand, the development of metallic bands is observed in the region of the valence electrons with increasing cluster size. For the core electrons and the Fermi edge, on the other hand, characteristic shifts of the *binding energies* (BE) can be detected.

Some effort has been made in the past to understand these shifts, which are often observed in the photoelectron spectra of deposited metal particles. Apart from oxides, weakly interacting supports, in the first place graphite, have been used for this purpose [65–70,208]. It has turned out though that it is actually a difficult matter to distinguish between initial [67] and final state effects in this case [65]. Regarding the initial state, reduced metal–metal co-ordination, rehybridisation in the VB (changes of the electron configuration) or specific metal–support interactions (e.g. oxidation of a metal upon deposition on an oxide) can play a role. Naturally, information about these issues is essential in order to assess the *size dependence* of the electronic properties or the nature of the *metal–support interaction*.

The final state, however, is also influenced by the size of the particle, because screening and delocalisation of the positive charge left on the aggregate during the photoemission process is limited as compared to an extended metallic system. This effect results in a shift of the entire PE spectrum which corresponds to the Coulomb energy of the localised charge and is therefore proportional to the reciprocal particle diameter [65,66,208]. In other words, binding energies of small metal aggregates should be found at higher values as is indeed observed in many cases. For very small clusters, of course, a transition to a molecular screening mechanism has to be taken into consideration as well [71,209].

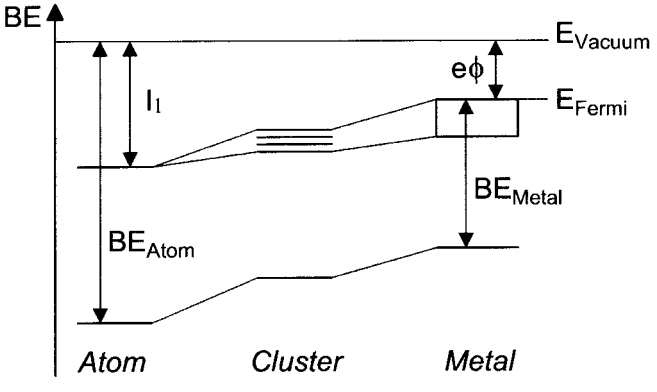

Fig. 7. Diagram illustrating the transition from an atom to a metal [65].

In this context, it is worthwhile mentioning that it is, in principle, feasible to separate final and initial state effects by determining the so-called *Auger parameter* [72]. This index is defined as the sum of the BE of a core level and the *kinetic energy* (KE) of the Auger transition belonging to the decay of the corresponding core hole: $\alpha = \mathrm{BE} + \mathrm{KE}$. Concerning the choice of the Auger transition, it is advisable not to take a line involving valence electrons as this can severely complicate the interpretation (e.g. due to many body effects). A problem resulting from this requirement may be that a rather deep lying core level ought to be chosen, which is perhaps not accessible with standard radiation sources. Without going into details now, an initial state contribution $\Delta\varepsilon$ may be estimated by: $\Delta\varepsilon = \Delta\mathrm{BE} + \Delta\alpha/2$ [73], with Δ = difference with respect to the bulk material.

If thin oxide films are used as a support for studies regarding the electronic structure of small metal particles, a decisive question arises: are their properties influenced by the metal substrate underneath, i.e. is the situation actually comparable to bulk oxides? We have intensively dealt with this question in the case of the thin alumina film on NiAl(110) by help of various electron spectroscopic techniques. It has, for example, been shown for Pd and Rh deposits that the binding energies strictly obey a $\langle d \rangle^{-1}$ law ($\langle d \rangle$: mean particle diameter) ruling out substantial tunneling from the substrate on the time scale of the core ionisation process ($\backsim 10^{-17}$ s) [7,190] (see also Section 5). Moreover, a comparison of Auger and autoionisation spectra of CO covered Pd particles revealed that, even on the time scale of the core hole lifetime ($\backsim 10^{-15}$ s), no detectable charge transfer occurs [74]. As schematically summarised in Fig. 8, electron tunneling from the NiAl substrate can thus be safely disregarded for *sufficiently fast* perturbations in the electronic structure (such as the creation of a core hole) of the deposit. (On the other hand, the charge transfer times are short enough to avoid static charging on the surface, as pointed out before!) Nevertheless, it is important to note that this is not necessarily true for all thin-film supports and must be checked from case to case [75].

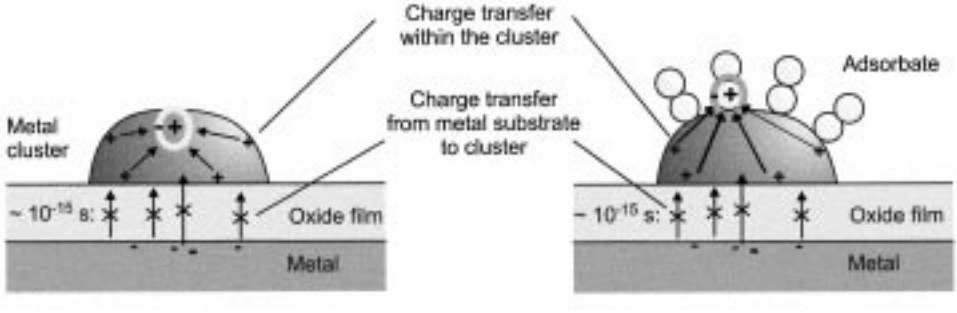

Fig. 8. Drawing illustrating the screening mechanisms after creation of a core hole within the cluster (left) and within an adsorbate layer (right). Charge transfer screening provided by the metal underneath the oxide is not observed during the core hole lifetime.

2.5. Infrared spectroscopy

Since the pioneering work of Eischens, who first studied supported-metal catalysts by infrared spectroscopy [76,210], this technique has been one of the primary tools to investigate the bonding of molecules to solid substrates. From the spectral features of the system under investigation, information on the *identity of the adsorbate*, its *interaction with the substrate*, most notably on the nature of its *adsorption site*, and on *intermolecular interactions* may be extracted.

The application of IR spectroscopy to the study of supported-metal particles on planar dielectric supports started much later, though. As oxides are usually weakly absorbing in the mid-IR regime, *transmission* IR spectroscopy may be applied to model catalysts prepared on bulk oxide single crystals [77,78]. Such systems have also been studied in a grazing reflection geometry [79,80]. More often, however, thin-oxide films on metal single crystals, either polycrystalline [81,211] or ordered [8,82–85,212], have been the subject of such experiments.

Infrared reflection absorption spectroscopy (IRAS) is a technique originally devised to investigate molecular adsorbates on metal surfaces [86,87]. When applied to thin dielectric films, it provides simultaneous benefits from several advantages, as compared to measurements on bulk oxide samples. The *grazing reflection geometry* results in a large accessible sample area with a correspondingly high number of adsorbed molecules, thus yielding strong absorption bands. A large signal intensity is ensured by the high reflectivity of the metal substrate.

As the film thickness is much smaller than the IR wavelengths used, the well-known surface selection rule for IRAS studies of adsorbates on metal surfaces applies, i.e. absorption bands due to vibrational modes with dynamic dipole moments parallel to the surface are extremely weak and, therefore, in general, not observable. Consequently, access to information on adsorbate orientation, as obtained by polarisation dependent measurements [88,213], is limited, although this shortcoming may be less severe for supported 3D metal particle systems than for molecular adlayers on crystalline planar surfaces.

An example which illustrates the potential of the technique is given in Fig. 9, displaying an IR spectrum acquired after CO saturation of a Rh deposit on the thin alumina film mentioned above [83,89]. In the spectral region around 2000 cm^{-1}, absorption bands due to the stretch vibration of CO adsorbed in various sites of different nature are observed. In this way, molecular bonding to the metal particles can be characterised in detail. In turn, the admolecules constitute structural probes to, for example, close-packed facets on the aggregates. Here, use is made of corresponding data from adlayers on metal single crystals. For molecules with large dynamic dipole moments, such as CO or NO, IRAS possesses an extraordinary sensitivity, also rendering studies at extremely low metal or adsorbate exposures possible.

Apart from molecular vibrations, IRAS also provides access to the vibrational properties of the oxide support. The Fuchs–Kliewer phonon modes of the alumina film, for example, are observed at wavenumbers below 1000 cm^{-1} in the spectrum shown in Fig. 9 [89]. When monitored as a function of metal exposure and further

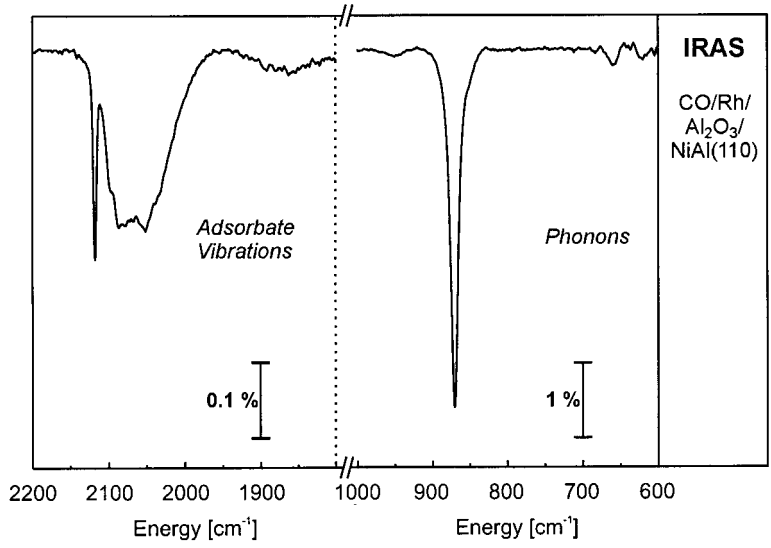

Fig. 9. Example of an IR spectrum taken after metal deposition onto a thin oxide film support and subsequent saturation with CO ($Rh/Al_2O_3/NiAl(110)$).

sample treatment, damping and characteristic shifts of these modes are detected. Thus, IRAS constitutes a tool to study the metal–oxide interaction as well.

3. Substrate: Al_2O_3/NiAl(110)

As already mentioned in Section 1, the support material of all systems discussed in this article is a thin alumina film, which can easily be prepared on the (110) surface of a NiAl alloy single crystal [16]. The most prominent feature of this film is its high degree of long-range order setting it apart from the amorphous alumina films grown on aluminium single crystals [90,91,214,215,257]. This is, to a large extent, due to the higher melting point of the alloy allowing preparation temperatures, which are sufficiently high to order the oxide overlayer [16]. Another advantage of the system is the excellent reproducibility of its structure, thickness and defect density. In Sections 3.1 and 3.2, these properties will be described in more detail.

3.1. Electronic and geometric structure

The oxidation of a NiAl(110) surface results in a characteristic LEED pattern with a surprisingly large number of very sharp extra spots in addition to the substrate spots [16,17]. Fig. 10 shows the pattern as well as the geometry and the dimensions of the oxide unit cell. Due to the two-fold symmetry of the substrate, the formation of two domains A and B rotated by $\backsim 48^\circ$ with respect to each other

is observed. Furthermore, a closer look at the pattern reveals that the oxide grows commensurably along the [1$\bar{1}$0] and incommensurably along the [001] direction of the NiAl(110) surface.

As the unit cell is exceptionally large, it has not been possible to determine the atomic arrangement within the unit cell by LEED until now. By a combination of *ion scattering spectroscopy* (ISS) and photoemission, however, it has been proven unambiguously that the film does not contain any Ni (see Fig. 11) [92,93]. In addition, several electron spectroscopies have been employed in order to get information about certain structural elements. Angular resolved photoemission, for example, allows the conclusion that the oxygen ions form a quasi-hexagonal

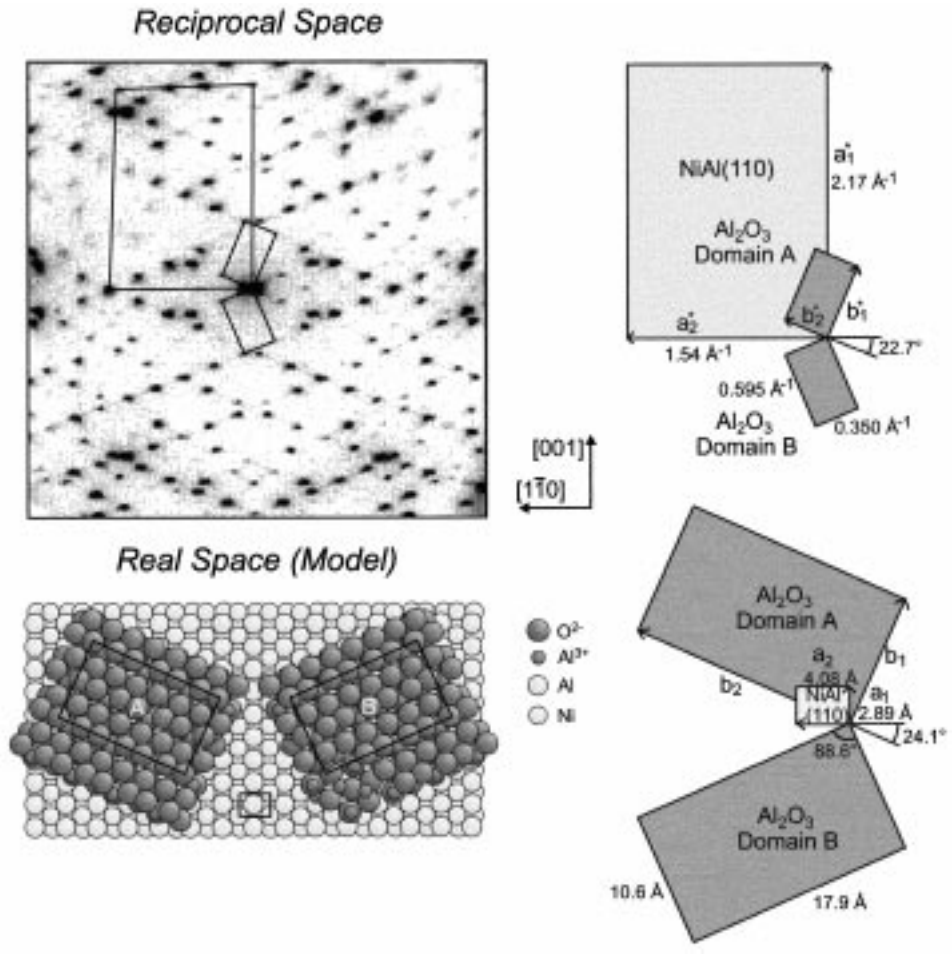

Fig. 10. LEED pattern (slightly distorted due to instrumental reasons) and schematic model of the system Al_2O_3/NiAl(110) as well as the dimensions of the unit cells of substrate and oxide overlayer in real and reciprocal space.

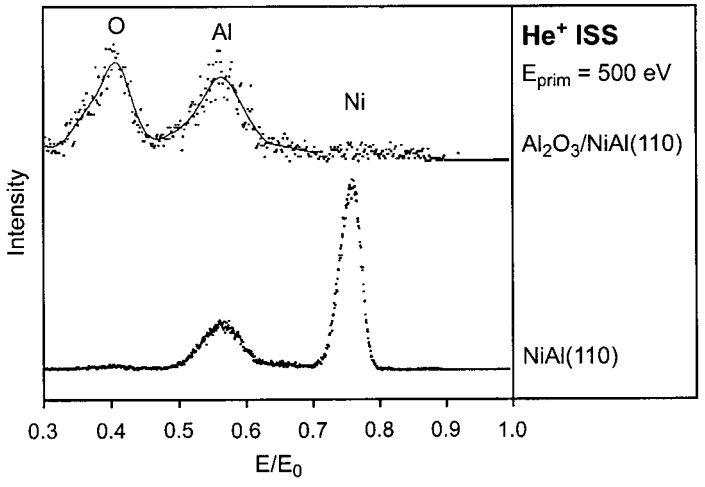

Fig. 11. He^+ ion scattering spectra of the clean and oxidised NiAl(110) surface.

structure [16]. Concerning the co-ordination of the aluminium ions, *electron energy loss spectroscopy* (EELS) data suggest a situation similar to γ-alumina where the ions reside in tetrahedral and octahedral sites [16]. Meanwhile, a γ-alumina like structure has also been corroborated by TEM [64]. The thickness of the oxide layer has been determined by *Auger electron spectroscopy* (AES) and LEED (damping of the substrate spots) [16,94]. The value of about 5 Å estimated in both cases points to an oxygen double layer.

Fig. 12 provides an overview of all relevant photoelectron spectra of the core and valence band states taken at normal and grazing emission [16,95]. In all spectra, several spectral components can be identified, which belong to species in different layers of the composite system as inferred from their dependence on the emission angle. The broad feature at 75.0 eV in the Al 2p spectrum can be assigned to the oxide film, whereas the narrow peaks at 72.55 and 72.95 eV are due to the Al $2p_{3/2}$ and $2p_{1/2}$ emissions of the NiAl substrate. Since the weak shoulder on the low BE side of the oxide peak shows a similar dependence on the emission angle as the substrate, it has been attributed to Al in an interface layer between the oxide and the metal [95], in analogy to results regarding the oxidation of Al(111) [96,216]. Interestingly, also the O 1s peak exhibits a shoulder, but in this case on the high BE side. Taking the intensity increase at high emission angles into account, an assignment to O^{2-} in the topmost layer was suggested [97,217].

The VB region is dominated by O 2p bands emitting between ∽5 and 12 eV BE. Strong band dispersions are observed parallel to the surface pointing to a well-developed band structure along these directions [16]. (Not surprisingly, no dispersion is detected perpendicular to the surface, though.) At about 4 eV, the onset of the band gap of the oxide is found. The width of the band gap as determined by EELS is about 7.5–8 eV [98] in reasonable agreement with the

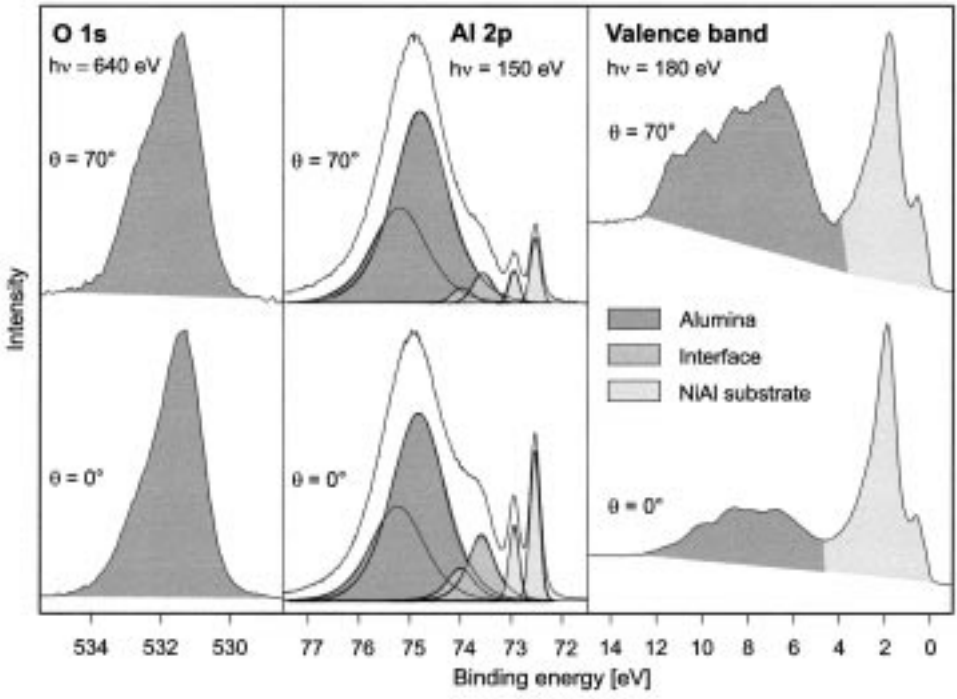

Fig. 12. Al 2p, O 1s and valence band photoelectron spectra of the alumina film taken at normal and grazing emission. Note that each Al 2p emission consists of two components (spin-orbit splitting).

band gap of γ-Al_2O_3 (8.7 eV) [99]. The features appearing between 4 eV and the Fermi edge are due to the Ni 3d states of the substrate. Of course, this also means that the Fermi edge of the NiAl can be used to reference the BE scale of all photoelectron spectra. This is one of the advantages when using thin oxide films instead of single crystals.

Owing to the fact that the film is so thin, it is ideally suited for STM measurements. Fig. 13 shows a number of images measured at varying tunneling voltages [17,100,218]. It is interesting to note that the appearance of the system is rather different in all three cases (cf. discussion in Section 2.2). At $+4.1$ V (a), tunneling into the unoccupied states of the oxide takes place. Here, a regular succession of stripes (distance: about 9 Å) is visible. After a closer look at the structure, the unit cell of the oxide can be identified as indicated in the close-up. If the voltage is switched to -4.1 V so that the occupied states are probed, an image (b) consisting of protrusions (diameter: about 9 Å) in a quasi-hexagonal arrangement is obtained, reflecting the hexagonal symmetry of the oxygen sublattice. The last picture in the series is the result of a measurement at -1.0 V. Taking the electronic structure into consideration, it is obvious that no states of the oxide can contribute to the tunneling process. Rather the metallic substrate is involved here. In a former investigation, it has been convincingly demonstrated

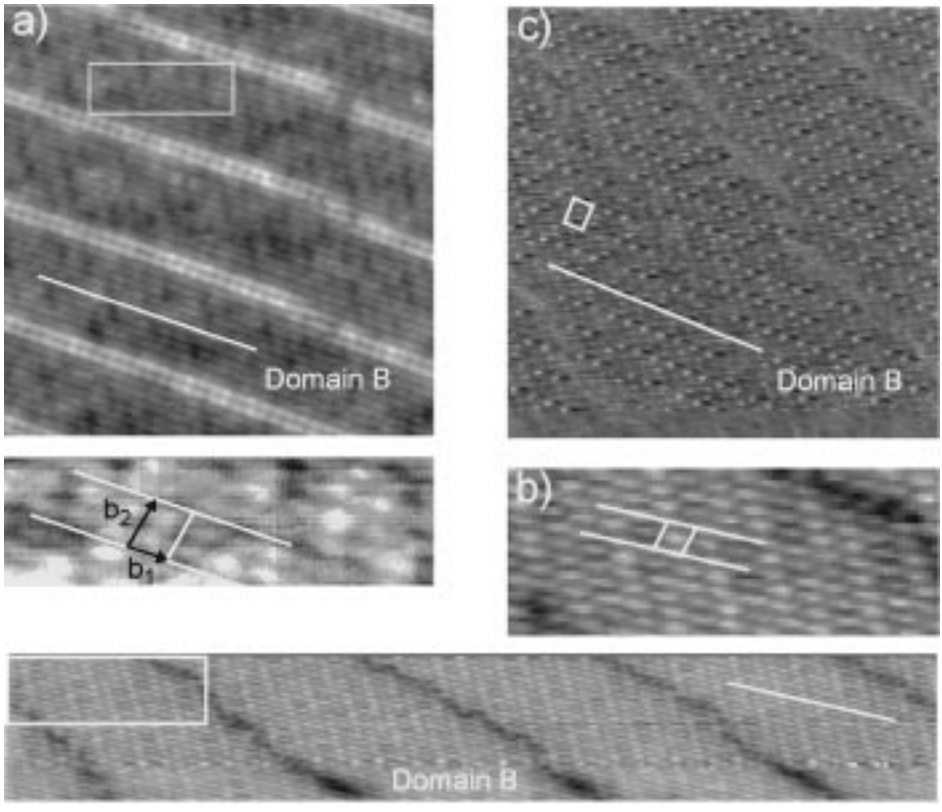

Fig. 13. STM (CCT) images of Al_2O_3 film on NiAl(110) taken at different voltages: (a) $U = +4.1$ V, $I = 0.8$ nA, 500 × 500 Å, close up: 180 × 100 Å; (b) $U = -4.1$ V, $I = 0.5$ nA, 1000 × 160 Å, close up: 100 × 160 Å; (c) $U = -1.0$ V, $I = 0.55$ nA, 300 × 300Å. The linear protrusions (a) and indentations (b) are antiphase domain boundaries discussed in Section 3.2. The distortion of the unit cells is caused by thermal drift.

that it is possible to image the interface (cf. Al 2p spectra) under these conditions [17]. From the large corrugation of about 1 Å and the sharp contrast, however, it can be concluded that in the present case the other mode mentioned in Section 2 is operative, i.e. the tip is in mechanical contact probing repulsive interactions with the surface. It is noteworthy that only in this mode the periodicity along the short side of the unit cell is resolved that clearly.

With respect to the adsorption experiments on the metal particles discussed in Section 6, it is also important to know the behaviour of the alumina support. The adsorption properties have been characterised for a number of molecules and it has turned out that the interaction is usually rather weak [16,98,101]. According to the *thermal desorption spectroscopy* (TDS) results, shown in Fig. 14, CO, for example, desorbs in the temperature regime between 30 and 70 K [98]. This weak interaction may be taken as an indication of an oxygen termination of the film,

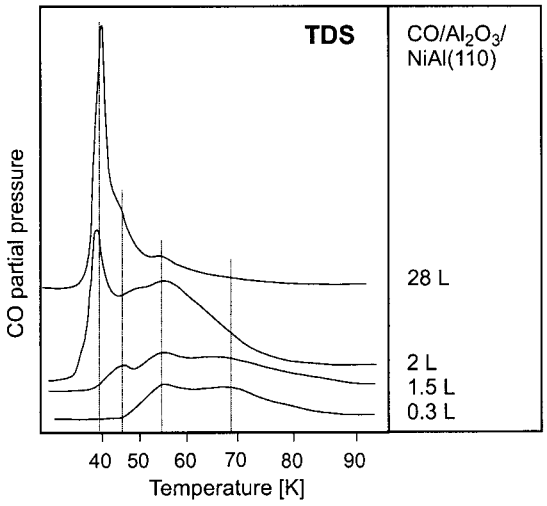

Fig. 14. Thermal desorption spectra of the system $CO/Al_2O_3/NiAl(110)$ (heating rate: ~0.3 K/s).

since stronger interaction could be expected in the presence of co-ordinatively unsaturated Al^{3+} ions [102].

3.2. Defects

According to the data discussed so far, the thin alumina film grown on NiAl(110) has a well-defined structure and an exceptionally high degree of long-range order. Nevertheless, STM and SPA-LEED measurements have also provided evidence for a number of characteristic defects, which play a role for the nucleation and growth of metal particles, as shown in Section 4 [17,100,218]. Three different types of them can clearly be identified in the STM images compiled in Fig. 15 [100,218].

The most prominent defect type are antiphase domain boundaries, which are usually only visible as a network of protruding lines (Fig. 15a), but actually have the appearance of double lines in better resolved measurements, such as those presented in Fig. 13(a) and Fig. 15(b). Moreover, these images reveal that each of these lines in turn consists of individual protrusions exhibiting the periodicity of the shorter unit mesh vector of the oxide. In contrast, some STM images, such as Fig. 13(b), show the boundaries as indentations. Since this is the topography which is found in *atomic force microscopy* (AFM) measurements as well [100,218], it is clear that the protrusions are due to the electronic structure rather than to the geometric structure of these line defects.

As seen in the line scan of Fig. 15(b), the boundaries separate oxide areas with a certain lattice mismatch, i.e. domains which are laterally shifted with respect to each other. It can be assumed that this defect type is caused by strain between the

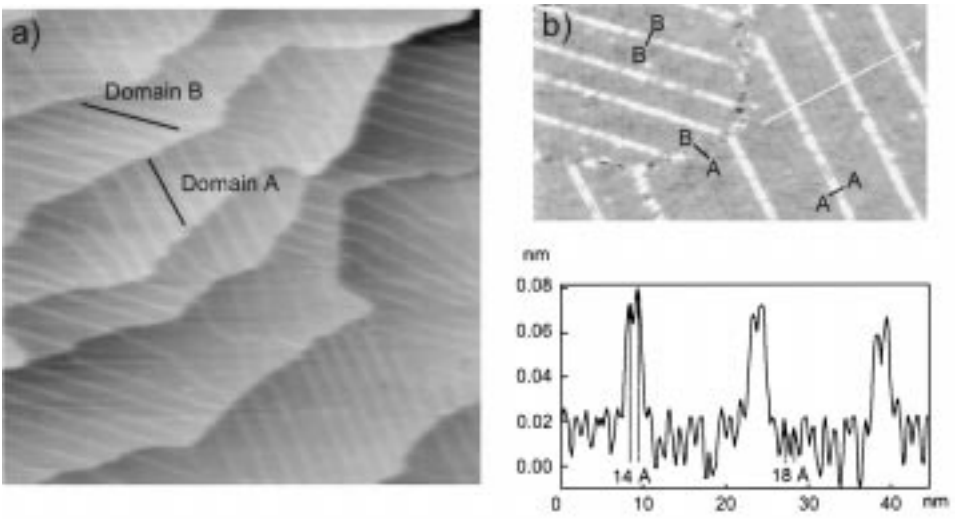

Fig. 15. STM (CCT) images of the Al_2O_3 film on NiAl(110) showing different kinds of line defects: (a) Antiphase domain boundaries and steps (+8.0 V, 1.0 nA, 3000 × 3000 Å); (b) Antiphase (A–A, B–B) and reflection domain boundaries (A–B) (+4.0 V, 0.5 nA, 1000 × 550 Å).

oxide and the substrate occurring during the growth process. Since the boundaries preferentially run along the direction of the short oxide unit mesh vector, a lot of domains have the shape of elongated stripes with an orientation that depends on whether they belong to reflection domain A or B (see Fig. 15a). Consequently, the angle between the two directions amounts to 48°. Apart from these straight lined boundaries, however, others running more irregularly have been observed with STM as well [17,100,218]. Therefore, an spot profile analysis of the LEED pattern has been carried out in order to obtain information about the mean orientation and dimension of the domains [17]. In this case, the existence of the antiphase domain boundaries gives rise to an oscillation of the halfwidth or a periodic spitting of the oxide superstructure spots as a function of the parallel scattering vector. It turns out that, on average, the domains have their minimum lateral extension of about 120 Å along the $[1\bar{1}0]$ direction of the substrate. Additionally, the mean lateral displacement of two adjacent domains has been determined in this study. The obtained value of about 3.6 Å along $[1\bar{1}0]$ is in agreement with the displacement of $\backsim$4 Å (18−14 Å) visible in the STM line scan of Fig. 15(b), if projected into the $[1\bar{1}0]$ direction.

The other two types of line defects noticeable in Fig. 15 are steps and boundaries between domains of type A and B. With respect to the steps, it is remarkable that only step heights have been measured, which correspond to monoatomic steps *of the NiAl substrate* [17,100,218]. Obviously, the growth of the oxide film is entirely 2D. Regarding the reflection domain boundaries, it is interesting to note that they, perhaps not unexpected, seem to be more disordered than their antiphase counterparts.

Apart from the line defects considered so far, the film must contain a certain density of point defects as well. Their existence could not be proven with STM or SPA-LEED, but has been inferred from other experiments. *Electron spin resonance* (ESR) spectra of the film, for example, show a paramagnetic resonance pointing to colour centres (removal of oxygen atoms) [103]. In fact, cathodo luminescence experiments lead to the same conclusion [104]. On the other hand, it is very likely that other types of point defects like neutral vacancies are also present. However, these are, in general, difficult to characterise.

4. Metal particles: structure and morphology

This section deals with the structure and morphology of metal particles grown on the thin alumina film by *vapour deposition*. It is divided into three subsections. Section 4.1 is concerned with the nucleation and growth at different temperatures, but focuses on the behaviour at 90 and 300 K. Various transition metals ranging from the early more reactive to the late noble transition metals will be considered. In Section 4.2, the thermal stability will be discussed, because this is a crucial point for adsorption and reaction studies at elevated temperatures or with temperature programmed techniques, such as TDS. Finally, in Section 4.3 we will briefly describe some growth experiments in ambient gas atmospheres. These demonstrate that certain gases can alter the growth mode drastically, and are sometimes connected with the formation of a compound on the surface.

4.1. Nucleation and growth at different temperatures

Before turning to the case studies, we would like to recall the processes taking place on the surface when a metal is vapour deposited onto an oxide support (see also reviews in Refs. [60,105,106]). This is schematically depicted in Fig. 16.

The first important step is the *adsorption* of the incoming metal atoms on the surface. In order to stick, the atoms have to get thermally accommodated to the surface. Otherwise, they would be elastically scattered. Since this has actually

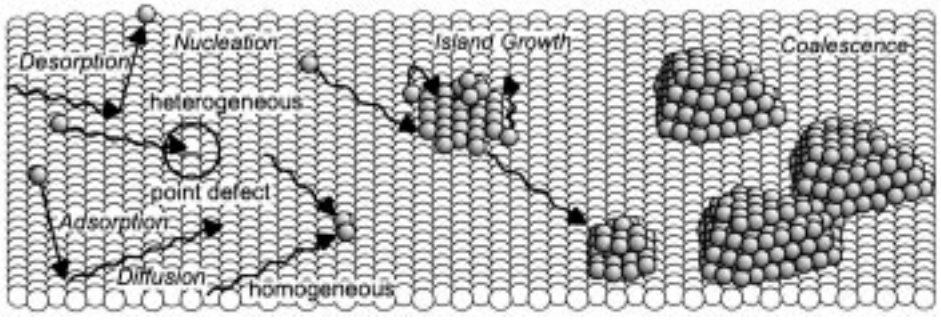

Fig. 16. Visualisation of the elementary steps taking place during the deposition of a metal.

never been observed, it can be safely assumed that every incoming atom initially sticks with unit probability [3,4]. This does not mean, however, that every adatom will be trapped on the surface. Due to re-evaporation, i.e. desorption, a net sticking coefficient may be obtained, which is smaller than one (incomplete condensation). As expected, this effect is the more important the higher the substrate temperature, but it has been shown that it is still near to one for many transition metals on oxides at room temperature (complete condensation) [107,219,220].

Once adsorbed, the atoms move across the surface depending on their *diffusion* coefficient:

$$D = \frac{1}{4}(\nu_0 a^2) \exp(-\varepsilon_{\mathrm{Diff}}/kT), \tag{1}$$

where $\varepsilon_{\mathrm{Diff}}$ is the activation energy for diffusion (which usually scales with the adsorption energy), ν_0 is the prefactor, a is the distance between two adjacent adsorption sites, T is the temperature and k is the Boltzmann constant. In order to travel a distance l, they need an average time, which is then given by:

$$\tau = l^2/(4D). \tag{2}$$

If defects are present on the surface, the adatoms may be trapped at these sites forming nuclei for subsequent growth processes, which is called *heterogeneous nucleation*. The other borderline case is *homogeneous nucleation*, where a stable nucleus is generated by aggregation of several (at least two) adatoms on regular sites. The minimum number of atoms a single diffusing atom must find for this process is called *critical cluster size*. By addition of further adatoms, these nuclei will then grow. In contrast, islands up to that size can dissolve again.

In the case of homogeneous nucleation, the saturation density of nuclei N is dependent on the diffusion coefficient and on the vapour flux F. For a critical cluster size of one atom, meaning that a dimer is already stable, the following proportionality can be derived [4]:

$$N \sim (F/D)^{1/3}. \tag{3}$$

(A more general derivation yields $i/(i+2)$ for the exponent, with i = critical cluster size [106]). Provided that heterogeneous nucleation prevails, the saturation density is independent of both the flux and the diffusion coefficient and, therefore, also of the temperature. This is observed in cases where the attraction between adatoms and defects is strong and the defect density comparatively high (i.e. distance between defects < distance L between islands expected for homogeneous nucleation: $L = (1/N)^{1/2}$) [3,108].

After reaching the saturation density of particles, no further nuclei form and all diffusing adatoms are captured by existing islands, i.e. only *growth processes* occur now. (Note that adatoms can also land on an existing island, if they have attained a certain size.) In this context, the question arises, which kind of growth mode

(3D or 2D) is expected for a given combination of a metal and an oxide. From the thermodynamic point of view, this question can be answered with the help of the surface free energies of the metal, γ_{Metal}, and the oxide, γ_{Oxide}, and the free energy of the metal–oxide interface, $\gamma_{\text{Interface}}$ [105,106,109]. If then

$$\gamma_{\text{Interface}} + \gamma_{\text{Metal}} \leq \gamma_{\text{Oxide}} \tag{4}$$

(free energy is gained by formation of the oxide–metal and a metal–vacuum interface), the metal wets the oxide at equilibrium corresponding to a layer-by-layer growth mode (*Frank-van-der-Merwe* growth mode). In the opposite case, i.e. the sum of $\gamma_{\text{Interface}}$ and γ_{Metal} is larger than γ_{Oxide}, wetting is thermodynamically forbidden and the metal is expected to form thick 3D aggregates (Volmer–Weber growth mode). Since surface free energies of metals (especially of transition metals) are often larger than those of oxides [4,110], Eq. (4) means that a layer-by-layer growth mode should be an exception and that the growth of 3D particles is very likely, which has indeed been observed in many deposition studies of metals on oxides [3–7,189,190,254].

In the case of a Volmer–Weber growth mode, the equilibrium shape of the aggregates can also be predicted. As shown in Fig. 17, it is a *Wulff polyhedron* truncated at the interface in accordance with the following equation [3]:

$$\Delta h/h_i = E_{\text{Adh}}/\gamma_{\text{Metal}(i)}, \tag{5}$$

where $\gamma_{\text{Metal}(i)}$ is the surface free energy of the corresponding crystal face i and E_{Adh} is the adhesion energy, given by [111]:

$$E_{\text{Adh}} = \gamma_{\text{Metal}(i)} + \gamma_{\text{Oxide}} - \gamma_{\text{Interface}}. \tag{6}$$

On the basis of Eq. (5), it is evident that the particles become flatter, when the adhesion energy increases. As concluded from Eq. (6), the adhesion energy is in turn dependent on the strength of the metal–oxide interaction. If this interaction increases, for example, by partial oxidation, $\gamma_{\text{Interface}}$ will decrease, resulting in larger values of E_{Adh}. Therefore, it is not surprising that adhesion energies have been found to roughly correlate with the negative enthalpies of formation of the oxide of the metal (per mole of oxygen) [6,112,189].

While it might be possible to describe growth at elevated temperatures within

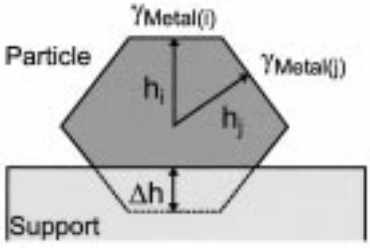

Fig. 17. Schematic representation of the Wulff–Kaichew construction (explanation in the text) [3].

the thermodynamic picture, thermodynamic equilibrium is usually not reached at room temperature or below, due simply to kinetic limitations. In order to elucidate this aspect, we refer to Fig. 18 from Campbell's work [4,113,221]. It shows the energy barriers a metal atom may experience when diffusing along the surface. E_1 and E_{-1} are the activation energies for upstepping and downstepping, respectively. The difference between the energies released upon adsorption on a metal island and the oxide is denoted ΔE. (It is worth mentioning, in this context, that it has meanwhile been possible to measure the heat of adsorption for metal deposition on oxides calorimetrically [114,222].) The essential quantity in the scheme is the large value of E_i, which is the energy gained by the capture of the adatom at the island edge. This strong attraction naturally results from the lateral metal–metal bonding. It is now easily understood that (a) upstepping is difficult and could be kinetically disallowed, while (b) downstepping is facile. Both effects lead to a 2D growth of the island and prevent their thermodynamic equilibrium shape, being attained.

This does not mean of course that 3D growth is generally impossible. If the islands are large enough, the homogeneous nucleation of atoms land on the island will overcome the downstepping, and a second layer will start to grow. In the following, 'assisted upstepping' processes can also cause material transport from the substrate level to higher layers of the aggregate (see Refs. [4,113,221] for further details). It is important to note that islands may thicken, even after the evaporation has stopped, by such processes (*self-thickening*) [4].

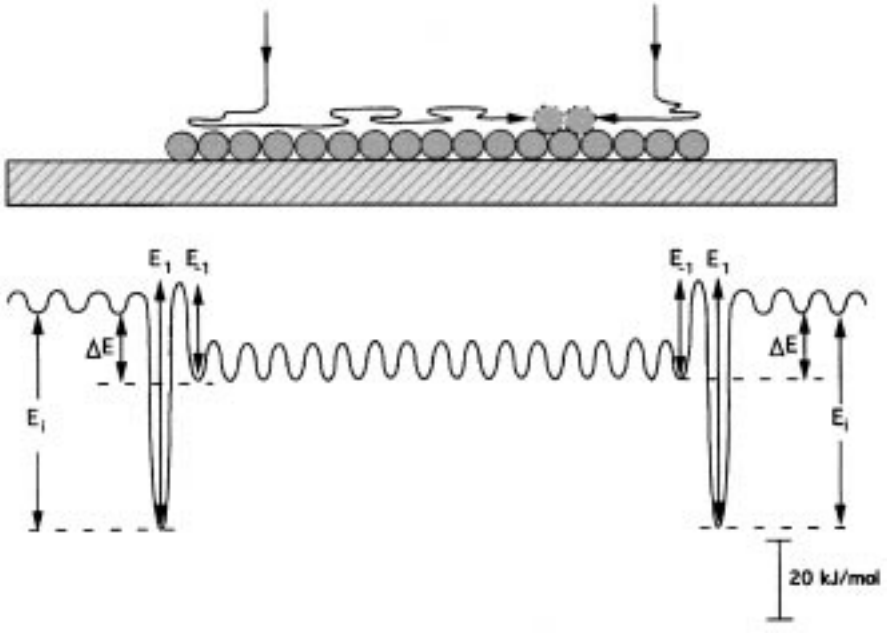

Fig. 18. Surface potential experienced by a diffusing adatom (explanation in the text, from [4]).

The last stage of the growth, shown in Fig. 16 is *coalescence* of particles at high coverages, which is characterised by a sudden decrease of the island density and an increase of the island size [3]. If deposition is continued, a granular film is the final result.

Having provided these introductory remarks, we now describe through several case studies. Our intention is to show how the interplay of all the steps, discussed so far, works for different metals on the same oxide and how it changes as a function of temperature.

4.1.1. Rhodium

The growth of Rh on a thin alumina film has been studied with SPA-LEED, as well as with STM. Starting with the diffraction results for deposition at 90 and 300 K, a number of interesting observations, regarding the spot profiles, are worth mentioning [115]. For both temperatures, neither an energy dependence of the profiles nor extra spots at higher Rh exposures have been detected, indicating the growth of predominantly disordered deposits, under these conditions. The shapes of the profiles reveal distinct differences, though. Whereas, an isotropic shoulder in the shape of a ring is recorded for the (00) spot at 90 K, deposition at 300 K leads to a strongly anisotropic profile as shown in Fig. 19.

In order to understand these differences, it is instructive to consult the results of the STM investigation [9,115]. The corresponding STM images are displayed in Fig. 19, next to the LEED spot profiles (Fig. 19b and d), proving that an anisotropic distribution of particles is the reason for the anisotropic spot profile at 300 K. Apparently, Rh has a strong tendency to decorate the line defects of the film, i.e. the antiphase and reflection domain boundaries, as well as steps [100,218]. The particles formed at 90 K, on the other hand, seem to be evenly distributed over the surface. No preferential decoration of the antiphase domain boundaries, visible in the picture as protruding lines, is observable. It is worthwhile noting that in both pictures (90 and 300 K), the characteristic stripes of the oxide are partly resolved, even in the immediate vicinity of the particles.

For the growth behaviour at 90 K, the question arises, which kind of nucleation mechanism (homogeneous or heterogeneous) is active. Therefore, experiments at different evaporation fluxes have been conducted [100,218], the results are displayed in Fig. 20. Without doubt, no significant difference can be noticed (island density in both cases: 3.5×10^{12} cm^{-2}), so that a homogeneous nucleation mechanism can be ruled out. Obviously, the point defects of the film (see Section 3) act as nucleation centres, under these conditions. Their interaction with the Rh atoms, however, must be somewhat weaker, as compared to the attraction, which the line defects exert. Owing to the higher mobility of the adatoms, the influence of the point defects is, therefore, nearly suppressed at room temperature.

If larger amounts of Rh are deposited at 300 K, some interesting features are discovered [100,218] in STM images, such as those displayed in Fig. 21, which prove, for instance, that the formation of particles on the antiphase domains themselves is rare at 300 K, but still occurs. As clearly demonstrated in Fig. 21(a), the number of particles on the domains is strongly dependent on the domain size.

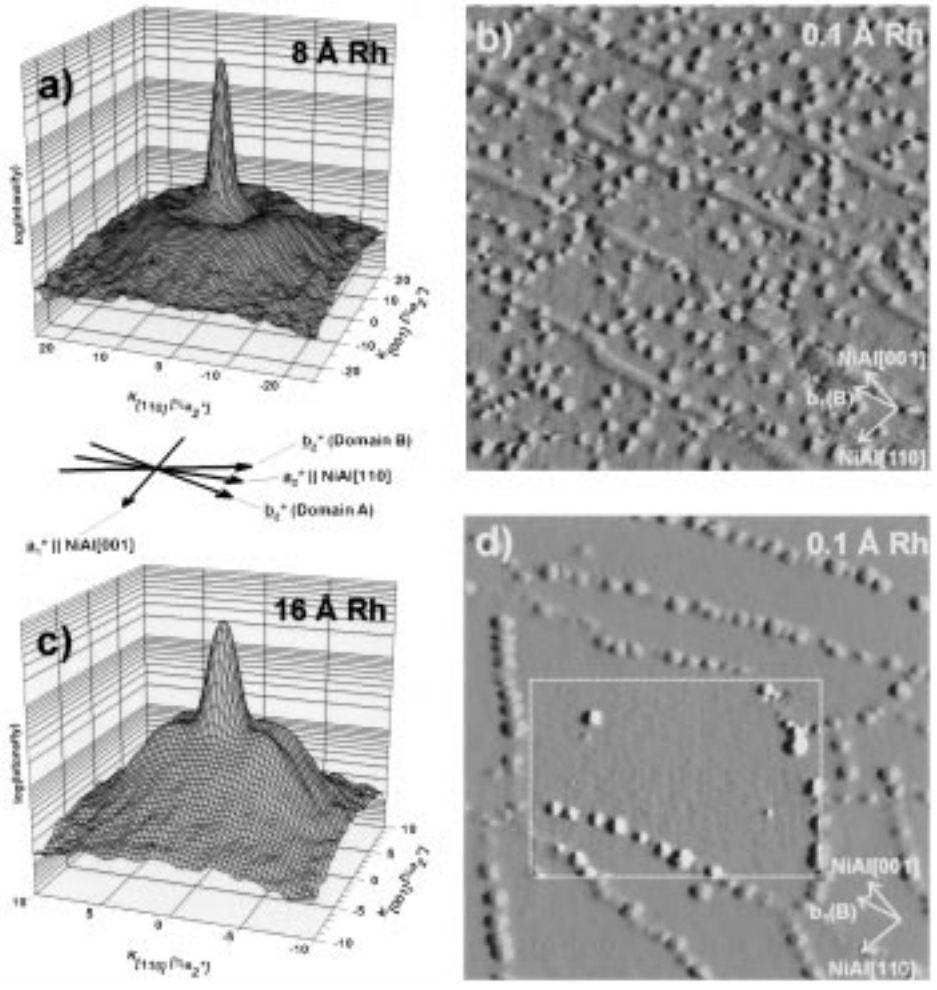

Fig. 19. Specular beam LEED profiles (40 eV) and STM images (CCT, 5 V, 800 × 800Å, inset scanned with higher resolution) after Rh deposition onto Al_2O_3/NiAl(110) at 90 K (a and b, STM image taken after warming up to 300 K) and 300 K (c and d) (Normal film thicknesses as obtained by a quartz microbalance are used to denote the different situations, 1 Å Rh = 7.3×10^{14} atoms cm^{-2}).

Only if the domains are large enough, can nucleation on the domains compete with nucleation at the boundaries. The resulting lower density of nuclei also explains why the particles on the domains are usually larger. In addition, Fig. 21(b) reveals that, at higher coverages, crystalline aggregates are occasionally formed (mainly on the domains), which are easily recognised by their regular shape. The aggregate presented in the close up (Fig. 21b), for instance, exhibits monoatomic steps, which are consistent with the Rh(111) interlayer distance of 2.4 Å. Last, but not least, it is noteworthy that Fig. 21(b) also shows a few examples of particles already influenced by coalescence processes.

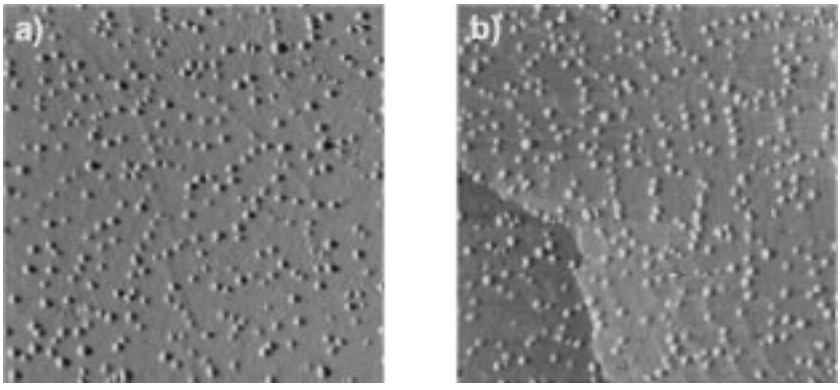

Fig. 20. STM images (CCT, 4.1 V, 0.5 nA, 1000 × 1000 Å) after depositing 0.05 Å Rh onto Al_2O_3/NiAl(110) at 90 K (pictures taken at 300 K). Evaporation rates: (a) 0.6 Å min^{-1}; (b) 0.006 Å min^{-1}.

Apart from the qualitative analysis of the STM data, a quantitative evaluation has been carried out for the growth behaviour at room temperature. For this purpose, particle densities, particle heights and diameters have been determined for a number of Rh exposures [100,218]. Regarding the diameter, the influence of the tip has been estimated and eventually corrected. The results are compiled in Fig. 22 (particle density, average diameter, aspect ratio and average number of atoms per particle) and Fig. 23 (correlation between height and diameter). In this connection, we would like to draw the reader's attention to the following aspects:

- As judged by the development of the *island densities*, two growth regimes can

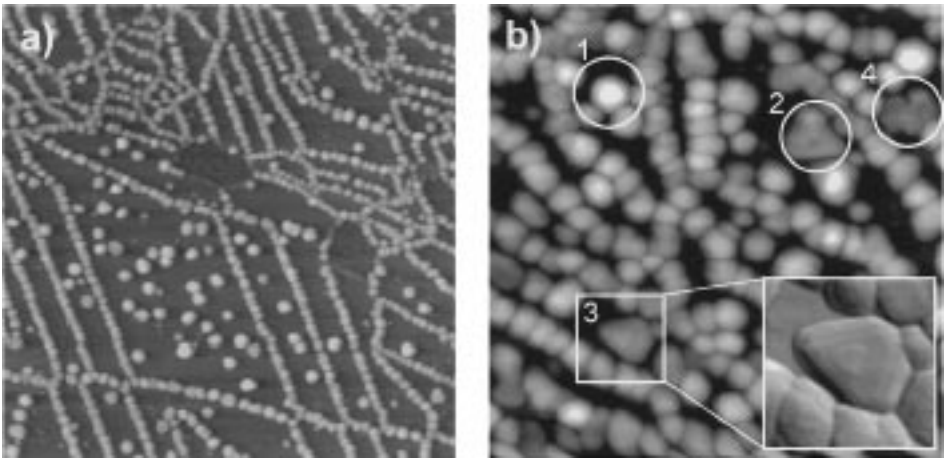

Fig. 21. STM images (CCT) showing the growth behaviour of Rh on Al_2O_3/NiAl(110) at 300 K for larger exposures: (a) 1.4 Å Rh (2.2 V, 1.2 nA, 2000 × 2000 Å); (b) 6 Å Rh (0.9 V, 1.2 nA, 1000 × 1000 Å): (1): disordered aggregate; (2), (3): Rh(111) crystallites; (4): particle formed by coalescence.

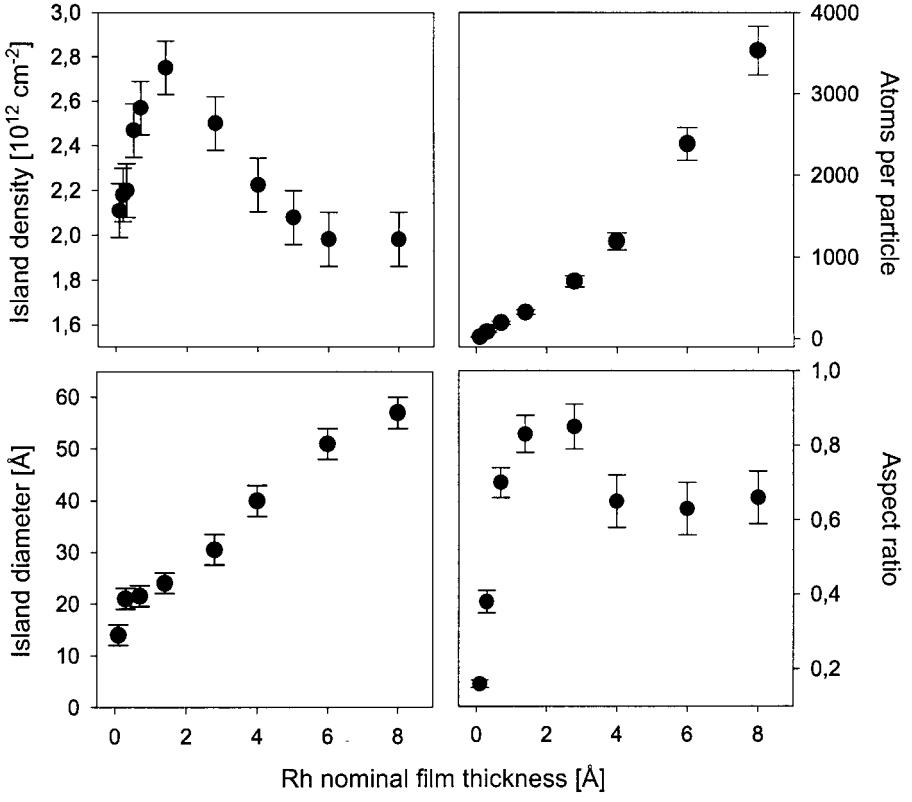

Fig. 22. Plots of the particle density, the average diameter, the average number of atoms per particle and the average aspect ratio as a function of the nominal film thickness for Rh growth at 300 K on Al_2O_3/NiAl(110).

be distinguished (see also average number of atoms per particle). First, nucleation and growth processes are predominant as indicated by the increasing island density. At a nominal thickness above 1 Å, however, coalescence of particles becomes important, resulting in a decline again.

- Up to a nominal film thickness of about 1.4 Å, a linear *correlation between the particle height and diameter* is clearly observed which can be interpreted in terms of a uniform particle shape with fixed proportions. Due to the coalescence of particles, this correlation breaks down for higher coverages.
- The *aspect ratio*, defined as the ratio between mean particle height and diameter, passes through a maximum at the same point. While this result can be explained by coalescence as well, the steep increase and the high value reached is rather remarkable. Obviously, Rh has a strong tendency to form thick 3D particles at 300 K.

Although the latter topic has not been not studied so systematically at 90 K,

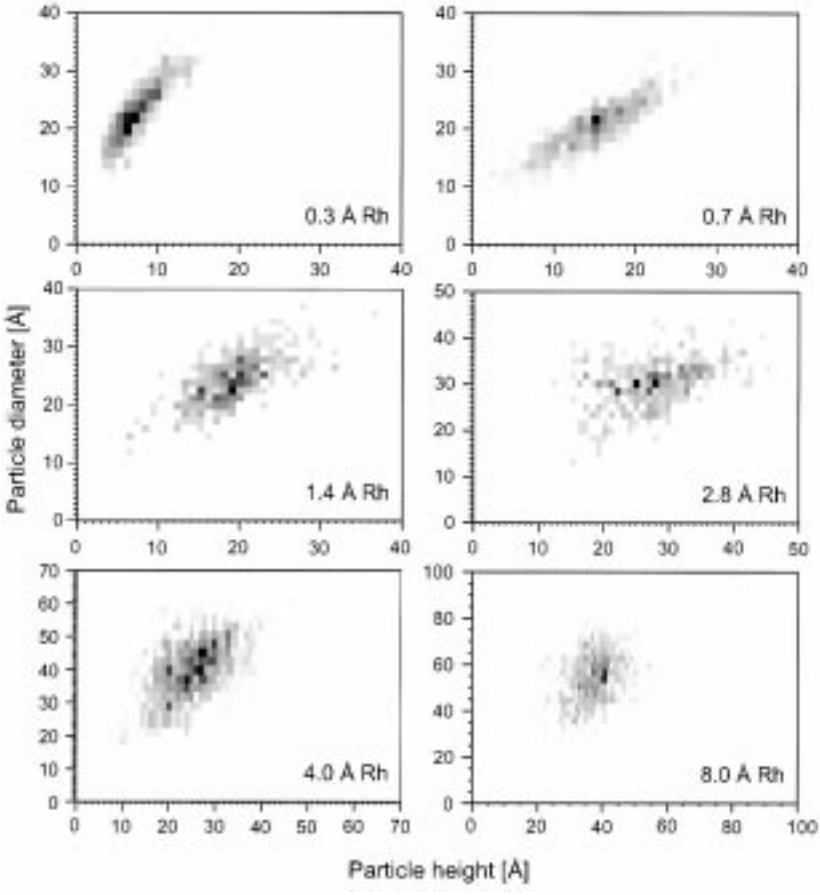

Fig. 23. Correlation between the particle height and diameter for Rh particles grown at 300 K on Al_2O_3/NiAl(110). (Grey scale according to number of particles).

the STM data prove that the growth of thick 3D particles is likewise preferred. At a nominal film thickness of 1 Å, for example, particle heights up to 20 Å were already measured.

To complete the discussion for Rh, we finally turn to the growth at elevated temperatures. An STM image showing the situation after deposition of Rh at 600 K is found in Fig. 24. As might be expected, ordered aggregates with flat tops are now preferentially formed which can be identified as Rh(111) crystallites [100,218]. Nevertheless, the antiphase domain boundaries still govern the nucleation behaviour.

4.1.2. Palladium

At 300 K, the growth of Pd on the alumina film features some interesting differences, as compared to Rh [116]. Here, deposition leads to the formation of

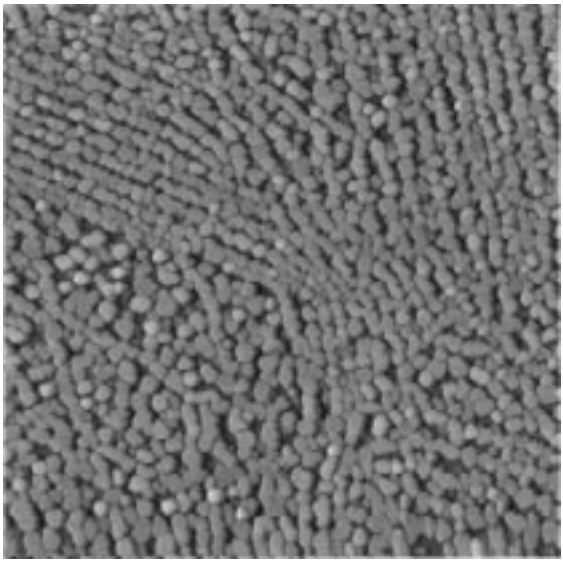

Fig. 24. STM image (CCT, 1.3 V, 1.3 nA, 3000 × 3000 Å) of 8 Å Rh deposited onto Al_2O_3/NiAl(110) at 600 K.

extra spots in the LEED pattern in the high-coverage regime. The symmetry and the dimensions of the pattern allow the conclusion that large 3D Pd(111) aggregates preferentially grow under these conditions, which are azimuthally aligned with respect to the close-packed rows of the oxide (lattice mismatch: 7.8%, $[1\bar{1}0]_{Pd}//\vec{b}_2$, see Fig. 10). In fact, they have the same epitaxial relationship as the rare Rh(111) aggregates. This result has also been corroborated by a spot profile analysis of the (00) LEED beam. As shown in Fig. 25, the halfwidth of the diffuse part of the profile clearly depends on the energy. Since the corresponding minima and maxima appear at in-phase and out-of-phase energies, with respect to the Pd(111) interlayer distance, this proves the existence of Pd(111) steps.

At 90 K, on the other hand, the growth behaviour is rather similar to Rh. Even at high coverages, no extra spots were visible. Moreover, the spot profiles depicted in Fig. 25 show only minor variations as a function of energy either. Apparently, the particles are disordered like their Rh counterparts. It is worthwhile noting that the shoulder has the shape of a ring here as well, revealing the generation of a peaked island distance distribution in both cases.

On the basis of the quantitative evaluation of the SPA-LEED data described in Section 2, the particle diameters plotted in Fig. 26 have been determined. In addition, Fig. 26 contains plots of the island density and the average number of atoms per particle, as calculated from the diameters with the help of the total amount of metal deposited. In analogy to Rh, the regime of nucleation and growth and the regime of coalescence can be distinguished at 300 K. The saturation density of particles, however, is reached at a significantly higher exposure, as compared to Rh. At 90 K, the situation is different. Here, a very

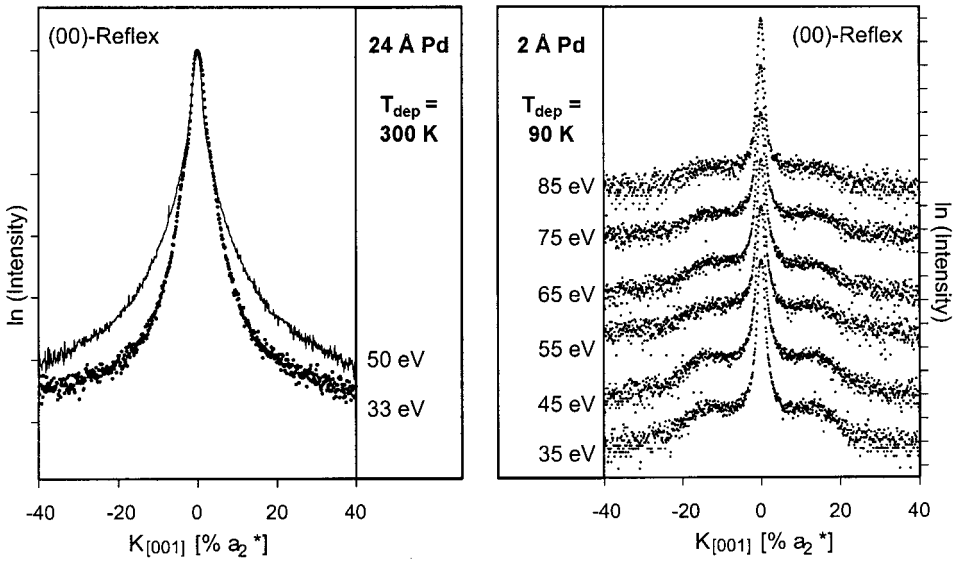

Fig. 25. Profiles of the (00) spot along the [001] direction of the NiAl substrate after deposition of Pd onto Al_2O_3/NiAl(110) at 300 K (left) and 90 K (right). (1 Å Pd = 6.8×10^{14} atoms cm^{-2}).

high island density is already observed at very low coverages. Coalescence sets in at an early stage accompanied by a steady decrease of the island density. As the initial density is nearly identical to the saturation density found for Rh at 90 K ($\sim 1.5 \times 10^{13}$ cm^{-2}), such a behaviour strongly points to a very efficient heterogeneous nucleation mechanism which is obviously not operative at 300 K. As a consequence of these different growth modes, it is possible to prepare very small clusters ($\sim$10 atoms) at 90 K, whereas only comparatively large particles are obtainable at room temperature ($>$1000 atoms).

In order to study the structure and morphology of the Pd(111) aggregates grown at 300 K in more detail, the SPA-LEED results have been complemented by an STM investigation. Fig. 27 shows an image of about 5000 × 5000 Å giving an impression of the particle arrangement on a large scale [117]. In agreement with their crystalline structure, many particles have a flat top and a regular triangular or hexagonal shape. Resembling the behaviour of Rh, the majority of aggregates is threaded along the antiphase and reflection domain boundaries of the alumina film. It may be surprising in this context that Pd, though also decorating the antiphase domain boundaries, does not give rise to an anisotropic shoulder of the LEED spots, which is due to the fact that the Pd particles are noticeably larger. In this way, the overall arrangement is much closer to an isotropic distribution than in the case of Rh.

In spite of the problems mentioned in Section 2, it has also been possible to image individual aggregates with atomic resolution [118]. The two pictures displayed in Fig. 28 beautifully prove that the aggregates indeed expose (111)

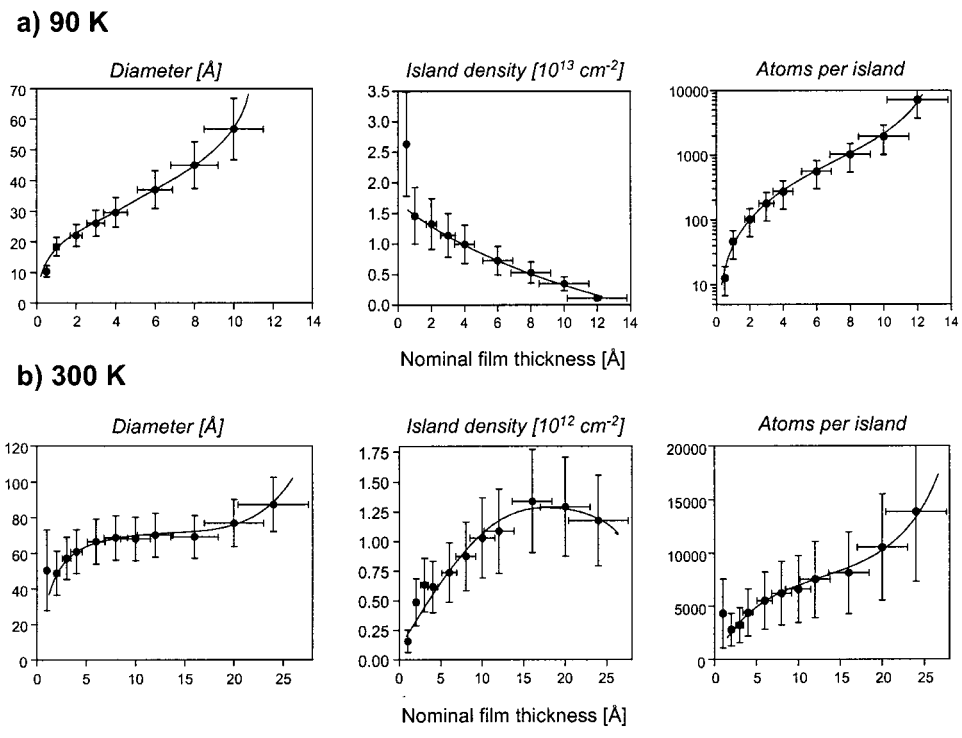

Fig. 26. Plots of the average island size, the island density and the average number of atoms per particle as a function of the nominal film thickness (1 Å Pd = 6.8×10^{14} atoms cm^{-2}) for deposition of Pd onto Al_2O_3/NiAl(110) at 90 K (a) and 300 K (b) as derived from SPA-LEED.

facets. On the top facet, the hexagonal arrangement of the atoms is clearly resolved. Sometimes, atomic resolution could even be achieved on the side facets. As demonstrated in Fig. 28(b), the larger facets exhibit a (111) orientation as well. Unfortunately, it has still been impossible to take atomically resolved images of the smaller (100) facets. The shape of the particles as derived from these experiments is schematically depicted in Fig. 29. Surprisingly, it is close to the equilibrium shape expected for supports with hexagonal symmetry. Usually, this is only observed at considerably higher temperatures [3].

4.1.3. Cobalt

The nucleation and growth behaviour of Co has been characterised within a larger temperature range than those of Pd and Rh [100,119,218]. The most important results can be inferred from the four STM images presented in Fig. 30:

- In analogy to Rh (and Pd), deposition of Co at 90 K (a) results in an isotropic arrangement of particles on the alumina surface. Since island densities at low coverages are very similar to those observed for Rh (Co: 5.6×10^{12} cm^{-2}, Rh

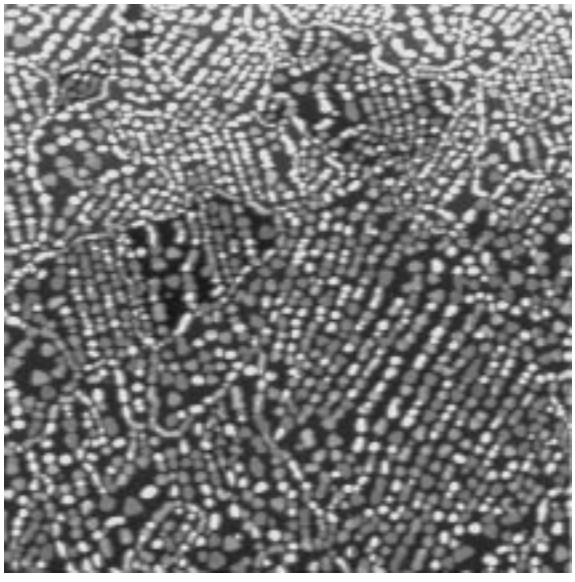

Fig. 27. STM image (CCT, 5000 × 5000 Å) of Pd particles (nominal film thickness: 4.4 Å Pd) grown on the thin alumina film at 300 K.

4.5×10^{12} cm^{-2} at 0.1 Å nominal film thickness), it is reasonable to assume that heterogeneous nucleation at point defects of the support predominates here, too. Moreover, Co shows the same tendency to form 3D particles.

- At 300 K (b) and 470 K (c), the situation changes slightly. Although the particle arrangement still seems random on the terraces, a preferred nucleation at step edges is evident. Furthermore, weak decoration of the domain

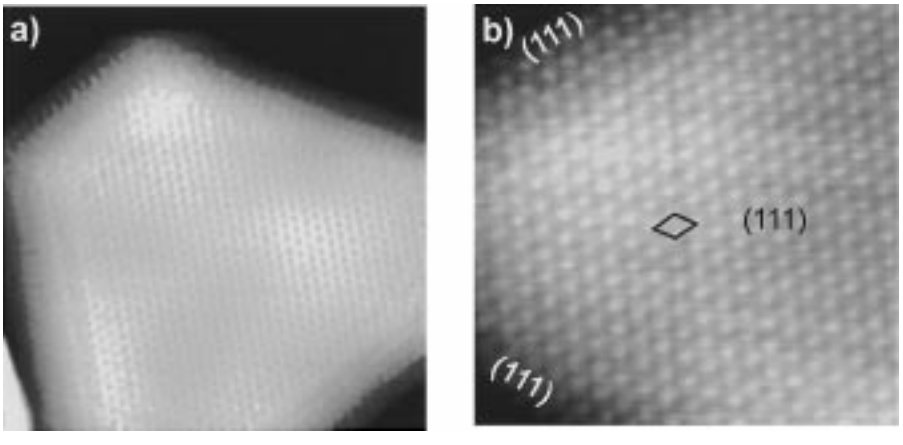

Fig. 28. STM images (CCT, (a): 100 × 100 Å) of two Pd aggregates grown on Al_2O_3/NiAl(110) at 300 K with atomic resolution on the top facet (a and b) as well as on the side facet (b) [118].

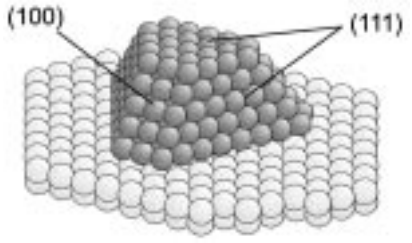

Fig. 29. Schematic drawing of the Pd(111) crystallites growing at 300 K on Al_2O_3/NiAl(110).

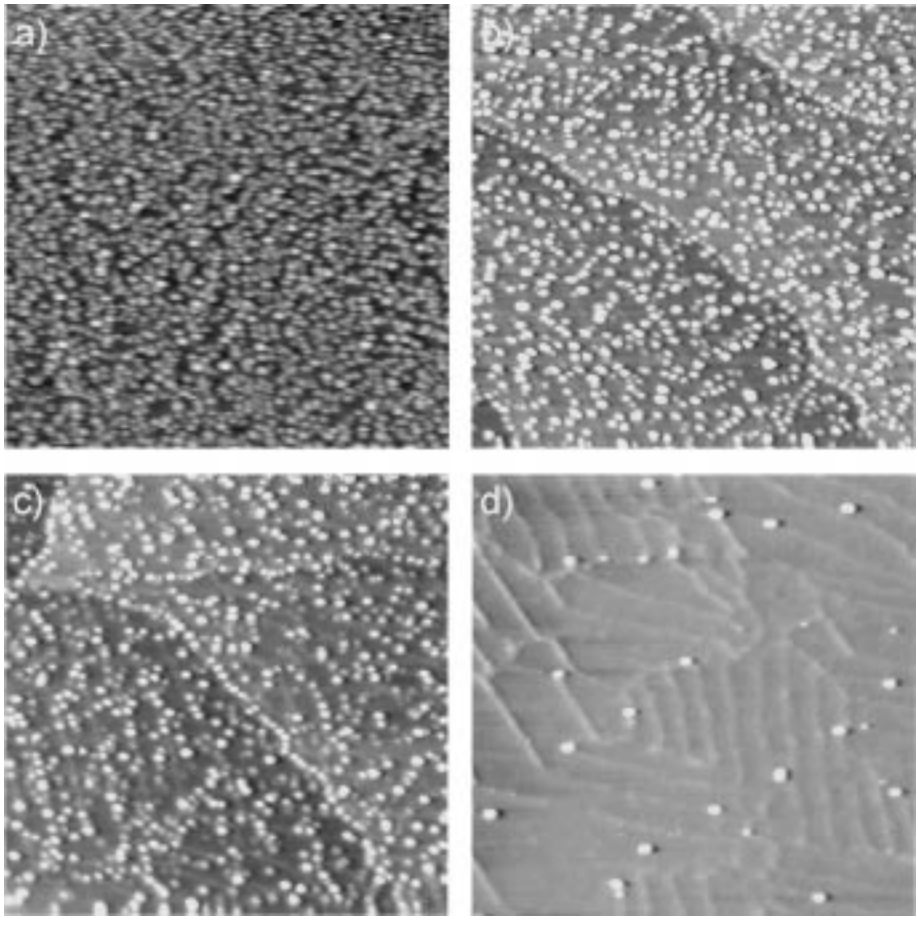

Fig. 30. STM images (CCT, 2000 × 2000 Å) showing the growth behaviour of Co on Al_2O_3/NiAl(110) ((a and b): 0.1 Å Co, (c and d): 0.3 Å Co, 1 Å Co = 7.8×10^{14} atoms cm^{-2}) as a function of temperature: (a) 90 K (6 V, 0.4 nA); (b) 300 K (5.0 V, 0.5 nA); (c) 470 K (8.4 V, 0.5 nA) and (d) 570 K (8.0 V, 0.4 nA).

boundaries can be discerned. Compared to 90 K, the island density is reduced, especially at 470 K. Concomitantly, the particle heights and diameters appear to be larger, i.e. bigger particles are formed as expected.

- If the deposition temperature is finally increased to 570 K (d), a drastic change takes place. Just a few particles can be detected on the surface. Although an increased desorption rate is certainly also responsible for the drastic loss of material, diffusion through the oxide into the NiAl substrate is probably the more important channel (see also Section 4.2). The structure of the film, however, is only damaged to a minor extent by this process.

In summary, the results suggest that the influence of the line defects on the nucleation of Co increases with increasing deposition temperature. Nevertheless, it is obvious that the antiphase domain boundaries have not nearly the same significance for the growth behaviour as in the case of Rh and Pd.

4.1.4. Platinum

For Pt deposition, SPA-LEED measurements have provided evidence of a specific metal–support interaction clearly differentiating this system from the other metals [120,121]. The most important data are compiled in Fig. 31(a). Especially striking is the strong damping of the oxide substrate beams. Already after deposition of 0.25 Å Pt at 300 K, which roughly corresponds to a tenth of a *monolayer* (ML), a reduction to 20% of the original intensity is found. Upon deposition of 1 Å Pt, the oxide spots finally vanish completely. Even if a strictly 2D growth mode is supposed, it is not possible to explain this strong attenuation of the oxide LEED pattern. Consequently, the only reasonable interpretation is a modification of the substrate in the vicinity of the deposits resulting in a loss of the characteristic structure of the film. At 90 K, the situation is very similar, although the damping is less drastic (upon deposition of 0.25 Å Pt a reduction

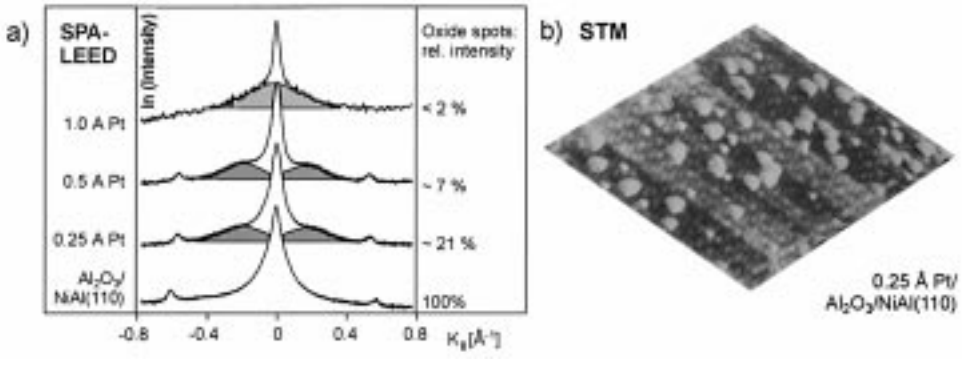

Fig. 31. $Pt/Al_2O_3/NiAl(110)$: (a) comparison of (00) spot profiles (45 eV, recorded along the $[1\bar{1}0]$ direction of the NiAl crystal) after deposition of various amounts of Pt (the satellites visible at 0.6 $Å^{-1}$ are superstructure spots of the oxide); (b) STM image (CCT, −4.0 V, 0.8 nA, 400 × 400 Å) of the alumina film covered with 0.25 Å Pt.

amounts to 43%). This is not too surprising, since a weaker interaction might be expected at the lower temperature.

According to the series of (00) spot profiles shown in Fig. 31 (the profiles at 90 K are nearly identical), the formation of these modified areas gives rise to a diffuse shoulder which, at low coverages, strongly resembles the shoulders observed for Pd and Rh at 90 K which suggests that the point defects of the support are involved here, too. Taking the structural impact of the deposit into account, it is reasonable to assume that any incorporation of Pt at these sites is connected with a corresponding distortion of the oxide superstructure. This idea is also supported by CO TDS experiments (see Section 6) pointing to the formation of an oxidised Pt species at low coverages. In order to estimate the size of the modified areas, a quantitative analysis of the spot profiles has been carried out yielding an average size of about 12 Å for the lowest amount deposited (0.25 Å Pt).

The SPA-LEED results for the growth behaviour of Pt have, in principle, been corroborated by a later STM investigation [122]. The image in Fig. 31(b), taken after deposition of 0.25 Å Pt, indeed proves the formation of small particles. The only discrepancy concerns the structural modification of the support, which is found with SPA-LEED but not STM. (According to the SPA-LEED evaluation, about half of the surface should be modified by the deposit, at this coverage.) The reason for this difference could be that LEED is much more sensitive to the small distortions caused by the Pt deposits than STM.

In addition to the experiments at 90 and 300 K, growth at 500 K has been studied with SPA-LEED as well [120,121]. In this case, however, only higher coverages (10 Å Pt) have been considered. The results show that now Pt crystallites with an (111)-orientation form on the alumina film. On the one hand, extra spots appear in the LEED pattern, which are compatible with the lattice constant of Pt(111). On the other hand, an energy dependence of the (00) spot profile is observed, which is in full agreement with the existence of monoatomic Pt(111) steps. It should be mentioned that, in contrast to Pd, deposition of larger amounts at room temperature have supplied no indications for the formation of ordered aggregates. Obviously, higher temperatures are necessary to establish crystalline order in the case of Pt.

In several cases of deposited metal particles, significant lattice contractions have been observed for very small aggregates, which are usually explained by surface stress inducing a pressure inside the cluster (see Ref. [3] and references therein). This question has also been subject of a TEM investigation in the present case [63]. On the basis of numerous HRTEM images and a subsequent analysis of the Moiré periodicities, it has been possible to calculate the lattice constants as a function of particle size. The corresponding plot is depicted in Fig. 32 and indeed proves that the atomic distances continuously decrease to 90% of the bulk value at a cluster size of 10 Å. On the other hand, the lattice constant approaches the Pt bulk value already at a diameter of 30 Å. A lattice contraction has also been detected for Ta and Pd clusters on the thin alumina film, but it seems to be less pronounced in these cases [123,124].

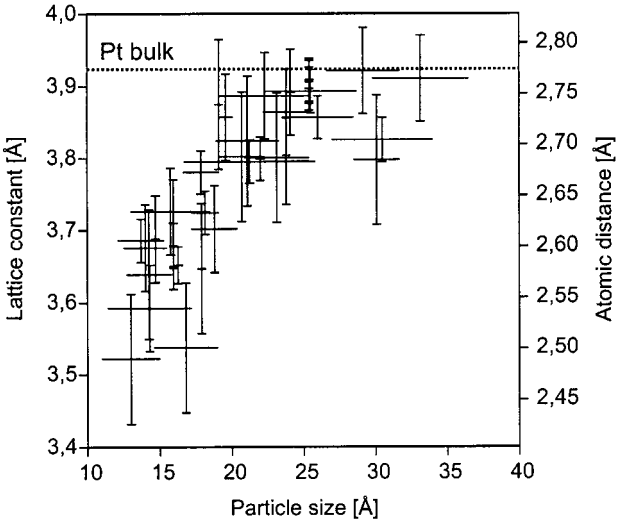

Fig. 32. Lattice constants and interatomic distances of Pt particles grown on Al_2O_3/NiAl(110) as a function of their size (the ends of the horizontal bars represent the width and the length of the particular clusters, respectively; while the vertical bars are error bars).

4.1.5. Vanadium

The last example, which we would like to discuss here, is vanadium. As an early transition metal, it is expected to interact more strongly with the oxide support than the mid to late transition metals considered so far. Fig. 33 contains two STM images for 0.04 Å (a) and 0.16 Å V (b) deposited at room temperature [125]. The pictures prove that vanadium prefers a Volmer–Weber type growth mode like all other metals studied on this support. Regarding the particle density ($\backsim 1.0 \times 10^{13}$ cm^{-2} at 0.16 Å V), the situation is strongly reminiscent of the Rh system at 90 K. This may be taken as an indication that heterogeneous nucleation at the point defects of the film governs the growth here as well.

According to the line scans, two types of aggregates can be distinguished for the smaller coverage, one of which is 3–4 Å thick, the other 6–7 Å. It has to be taken into account, however, that, at the tunneling voltages applied here (<4 V), the metal particles appear to be thicker than they are, since the alumina film itself does not contribute to the signal (see Section 2 and cf. Ref. [122]). Consequently, the measured particle height has to be corrected by the thickness of the film. That means that aggregates of the first type are probably incorporated in the film (including the possibility of a compound formation: see Section 5), while the second type is just one layer thick. Turning to the second image, particles consisting of 2 layers (8–9 Å) now can be found as well. At even higher coverages, thick 3D particles are finally formed. Although the initial incorporation is compatible with a strong interaction between V and the alumina support, the system switches rather early to a 3D growth mode.

In contrast, deposition at 600 K or higher temperatures results in highly

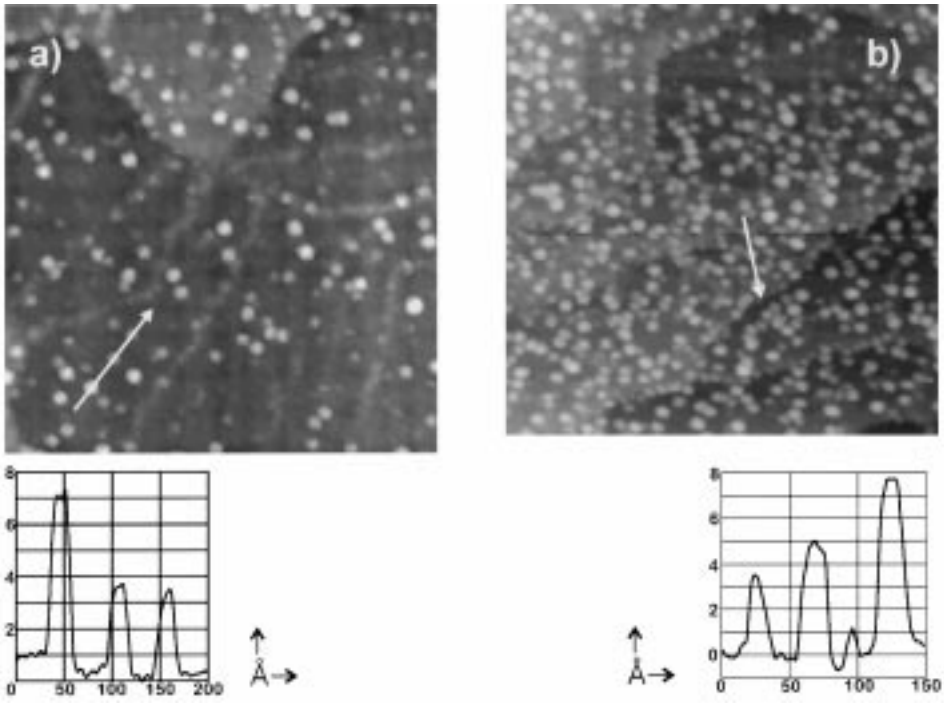

Fig. 33. STM images and line scans (CCT, 2.0 V, 750 × 750 Å) of V deposited onto Al_2O_3/NiAl(110) at 300 K: (a) 0.04 Å; (b) 0.16 Å V [125].

disordered surface structures [125]. Since even the LEED pattern of the film vanishes completely with this treatment, it can be concluded that the vanadium rapidly reacts with the alumina, leaving a severely distorted surface behind. If compared to the corresponding experiment with Co (no destruction of the film), the higher reactivity of V clearly becomes evident. Interestingly, a very diffuse hexagonal LEED pattern is still visible, showing that some long-range order is still preserved.

4.1.6. Comparison and overview

The above case studies reveal a number of interesting trends and common features which should be finally summarised:

4.1.6.1. Nucleation. The nucleation behaviour of all metals studied on the thin alumina film is apparently dominated by the defects of the support under the experimental conditions applied (UHV, deposition rates up to 1ML/min). Moreover, the results demonstrate that the defects of the support can play a varying role as a function of temperature. The most prominent examples, in this respect, are Rh, Pd and, to a minor extent, Co, i.e. metals with a medium metal–support interaction (see below). While at 90 K, point defects are the primary nucleation centres,

the line defects, such as step edges and domain boundaries, come to the fore at higher temperatures. This points to a stronger interaction with the adatoms, which, however, only comes into play if the thermal mobility is sufficient to reach them. By making use of this temperature controlled nucleation behaviour, the island density and, thus, the average particle size can be varied within a large range, giving access to very small clusters, as well as rather large aggregates (see Figs. 22 and 26).

In this context, it is worth mentioning that a series of investigations on different MgO substrates, similarly suggested that nucleation is strongly influenced by defects of the substrate [108]. Furthermore, a temperature dependence was also observed. Here, it was interpreted in terms of competitive homogeneous nucleation, though [108]. Presumably, heterogeneous nucleation is an important process on many oxide supports, as they often exhibit a considerable defect density (in particular point defects). This conclusion is also supported by recent theoretical studies [126].

4.1.6.2. Growth mode. All metals investigated on the alumina film clearly show a Volmer–Weber like growth mode. As mentioned before, this behaviour is generally expected on the basis of the surface free energies involved (see Eq. (4) and following argumentation as well as Ref. [127]). However, taking a kinetic model, such as the one in Fig. 18, into account, the strong tendency to form thick 3D particles very early, even at 90 K, is a little surprising. On the one hand, this may be due to the fact that self-thickening processes are already operative at low temperatures. On the other hand, it can be speculated as to whether the requirements of the model are fulfilled in the present cases. If ΔE, for example, exceeded E_i (see Fig. 18), there would be no stable sites at the island edges any longer, so that the driving force for spreading vanishes [4].

4.1.6.3. Particle size. Including Ag, which actually forms the largest 3D aggregates of all metals studied on the alumina film so far [7,128,190], the following rough trend concerning the particle sizes found at 300 K can be recognised: $Ag > Pd > Rh > Co > Pt \backsim V$. In principle, this series is in agreement with the prediction based on the enthalpies of formation of the oxides as an indicator for the respective metal oxide interaction. With an increasing interaction, the deposits should become flatter (see Eqs. (5) and (6)) and smaller (due to higher diffusion barriers). In fact, such correlations have also been observed for a number of transition metals on TiO_2 [6,129,189] and oxidised W single crystals [112]. An exception seems to be Pt in the present case. At least, according to the enthalpy of formation of the oxide, it should rank above the early and mid transition metals. This may be taken as an indication that an interaction with specific sites, presumably the point defects of the support, is decisive here.

4.1.6.4. Particle morphology. In all cases, only disordered particles are obtained after deposition at liquid nitrogen temperature. Naturally, kinetic limitations are responsible for this behaviour [3,4]. At higher temperatures, however, kinetic fac-

tors are less important and the formation of crystalline aggregates becomes possible [3]. This has indeed been observed for Pd, Pt and Rh. For Pt and Rh, which are more strongly interacting with the support than Pd, temperatures of about 500 to 600 K are necessary, whereas crystalline Pd aggregates are already found at room temperature. The crystallites of all three metals grow in the (111)-orientation, which is obviously enforced by the quasi hexagonal arrangement of the oxygen ions of the substrate. It is interesting to note that the polyhedral shape of the Pd crystallites, as imaged by STM, is one of the expected equilibrium shapes for a supported fcc metal particle with (111)-orientation (truncated tetrahedron, see Ref. [3], Fig. 22).

4.2. Thermal stability

Upon annealing, the structure of small deposited metal particles may change, due to a number of different processes, such as (a) diffusion into the substrate, (b) changes of the particle morphology and (c) sintering, i.e. growth of larger particles at the expense of smaller ones [2,3,5,254]. In the case of *thin oxide films*, diffusion through the film into the metallic substrate can limit the thermal stability significantly (see, for example, Refs. [10,191]). As demonstrated in Fig. 34, this aspect is also of importance in the present case, setting a limit to experiments at elevated temperatures. The STM images shown have been taken for Rh particles prepared at 90 K and annealed to the indicated temperatures [100,218]. An ensemble of very small aggregates has been chosen, since these should be most sensitive to the thermal treatment. Evidently, no major changes are visible up to 570 K; even a quantitative evaluation of the island density reveals no difference. Annealing to 770 K, on the contrary, brings about major structural modifications. On the one hand, the island density is noticeably decreased and, on the other hand, the particle height distribution becomes somewhat broader (see insets). After the next annealing step to 870 K, nearly all particles have eventually disappeared from the surface. (Note that the structure of the film is almost restored.) Since desorption at this temperature can be safely excluded, diffusion must play the predominant part. On top of that, sintering seems to contribute to the events in the temperature range from 600 to 900 K as well. This is the only explanation for the few particles which gained size at 770 K.

In summary, for Rh, diffusion and sintering can be neglected up to about 600 to 700 K on the thin alumina film. For Co, sintering processes have been shown to be significant from 600 K onward, resulting in a loss of the smallest islands [100,218]. At 800 K, diffusion through the oxide film sets in. Here, STM experiments proved that the process actually is defect mediated. Loss of material was mainly observed in the vicinity of the antiphase domain boundaries, thus acting as an important diffusion channel [100,218]. In the case of Pt, SPA-LEED experiments revealed an increasing destruction of the oxide superstructure upon thermal treatment [120]. According to *X-ray photoelectron spectroscopy* (XPS), this is also connected with a progressive oxidation of the diffusing Pt species [92]. Both findings are compatible with an initial incorporation of Pt into the film, probably

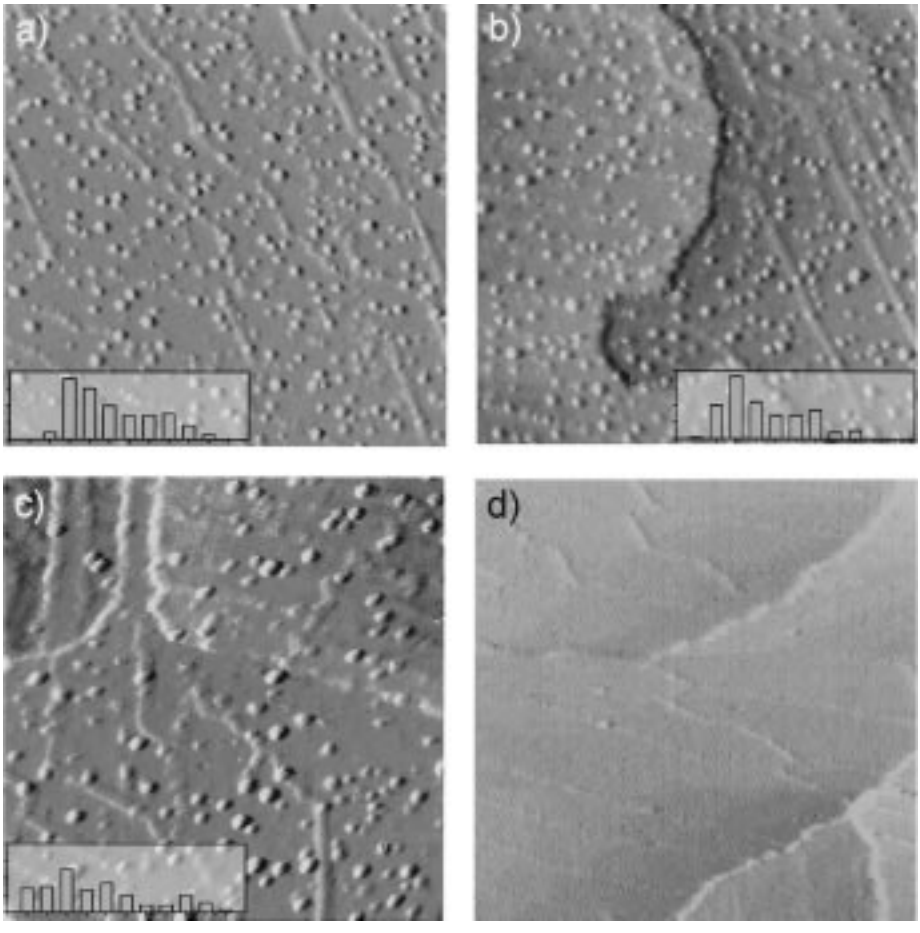

Fig. 34. Series of STM images (CCT, (a–c): 5.0 V, (d): 4.3 V, 1000 × 1000 Å) showing the thermal stability of Rh particles (0.05 Å Rh) on the thin alumina film: (a) as prepared at 90 K; (b) annealed to 570 K; (c) 770 K and (d) 870 K (pictures taken at 300 K). Insets: height distribution (*x*-axis: height [0–6 Å], *y*-axis: number of islands [0–40]).

starting at the point defects. Annealing to 1100 K, however, leads to a restoration of the film structure.

Due to the difficulty of achieving atomic resolution on individual particles, it is often impossible to trace thermally induced changes of the particle morphology with STM. Instead, the use of vibrational spectroscopies with suitable probe molecules can be very advantageous. Fig. 35 presents a case study for such an experiment [83]. Here, small Rh particles prepared at 90 K (average size ∽20 and 100 atoms per particle) on Al_2O_3/NiAl(110) have been annealed to 300 and 500 K, respectively. Subsequently, they have been cooled down to 90 K again, exposed to CO and studied with IRAS.

The spectra in Fig. 35 only show the bands resulting from terminally bound

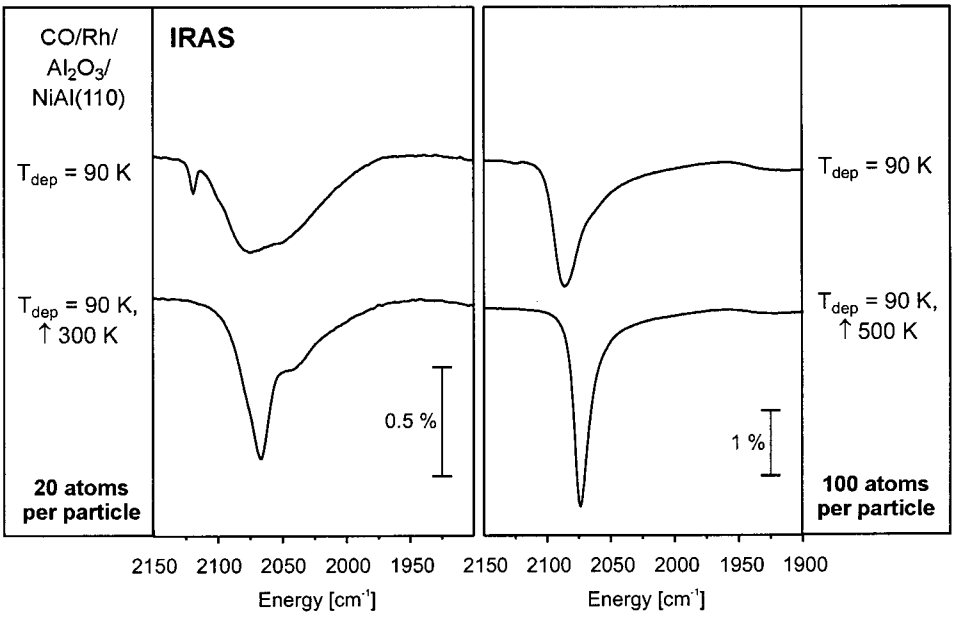

Fig. 35. Temperature induced morphology changes of small Rh particles on Al_2O_3/NiAl(110) as detected by IR spectroscopy with CO as a probe molecule. Upper spectra: taken immediately after deposition; lower spectra: after annealing to indicated temperatures (data acquisition at 90 K).

CO. In comparison to the spectra of the unannealed deposits, several changes are clearly detectable. First, the sharp signal at $\backsim$2120 cm^{-1}, visible for the smaller coverage, vanishes and, secondly, the intensity of the low-frequency shoulder, which is a common feature of both coverages, is significantly reduced after the thermal treatment. The interpretation of the latter observation is straightforward, if it is taken into account that CO molecules bound to defect sites on transition metals often exhibit a reduction in vibrational stretching frequency as compared to terrace molecules [131]. Therefore, the changes point to a certain loss of low co-ordinated metal atoms, i.e. a thermally induced ordering of the individual Rh particles.

The sharp band at $\backsim$2120 cm^{-1} has been ascribed to isolated Rh dicarbonyl species trapped at point defects of the substrate [83,130]. Hence, IRAS with CO as a probe molecule is also capable of detecting the nuclei of heterogeneous Rh nucleation at 90 K. Upon annealing to room temperature, these Rh atoms apparently migrate to larger Rh aggregates, resulting in the absence of the corresponding IR band after CO dosage.

4.3. Growth in ambient gas atmospheres

It has long been recognised that the treatment with certain gases can change the structure and morphology of deposited metal particles considerably [2]. In

technical catalysis, for example, calcination (oxidation) and reduction cycles are used to enhance the dispersion of supported-metal catalysts. Another example is the disruption of alumina-supported Rh catalysts by CO, resulting in the formation of isolated Rh gem-dicarbonyl species [132,133]. Meanwhile, it has been possible to duplicate this process in model catalytic systems as well [79,134,135,223,224].

In addition, such gases might also control the growth process itself, if present during the deposition of the metal [3,4,7,190]. Here, thermodynamic as well as kinetic factors can be of importance. The first situation is encountered when the adsorbate changes the surface free energies (cf. Eq. (4)) involved (see, for example, Ref. [136], where increased wetting is reported), the second, if the energetics of the elementary steps are altered [137,225]. In both cases, it is possible to obtain structures, which are otherwise not accessible.

This has indeed been observed for Pd deposition at 90 K in an ambient CO atmosphere of about 2×10^{-6} mbar [137,225]. Under these conditions, the formation of a binary compound of Pd and CO is found, giving rise to the TD spectra presented in Fig. 36(a). The characteristic sharp peak at about 190 K is due to the primary decomposition of this compound on the surface. The following peaks can then be assigned to subsequent decomposition steps and CO desorption

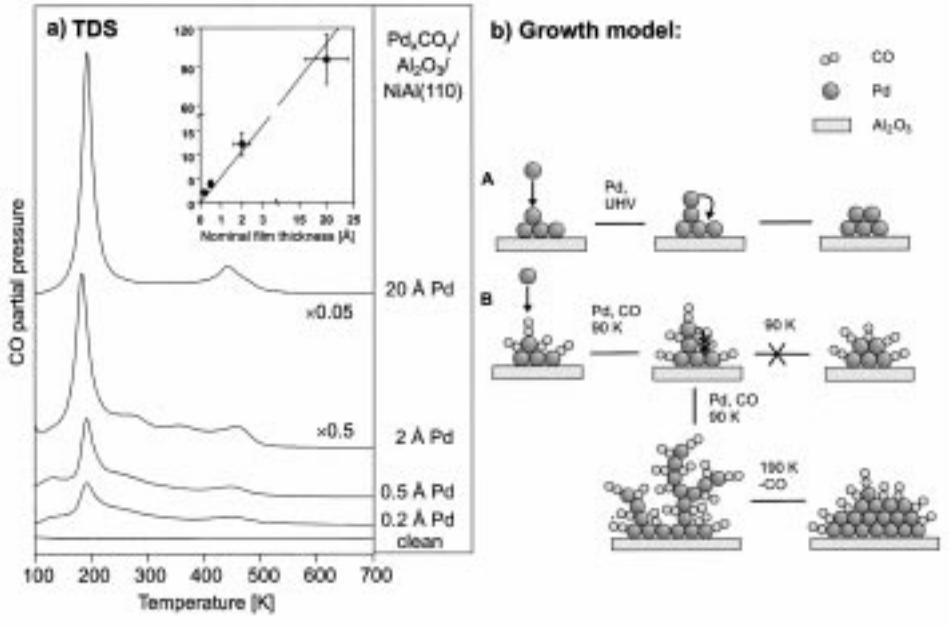

Fig. 36. (a) CO TD spectra for increasing amounts of Pd deposited onto Al_2O_3/NiAl(110) in an ambient CO atmosphere of 2×10^{-6} mbar at 90 K. Inset: total amount of desorbing CO as a function of Pd exposure. (b) Growth model.

from compact Pd aggregates left on the surface. Note that the total amount of desorbing CO is proportional to the amount of Pd deposited. From XPS measurements, a Pd/CO ratio of about 1:2 has been determined [137,225] and, according to IRAS, the compound contains terminally, as well as bridge-bonded, CO molecules with an intensity ratio of about 1:1 [138]. As inferred from PES data, an increasing number of metal–metal bonds is formed during growth, excluding the formation of isolated carbonyl species [137,225]. On the basis of all experimental results a growth model (*random-rain model* [139]) has been proposed which assumes kinetically inhibited diffusion of the incoming metal atoms to energetically more favourable sites, i.e. sites with more adjacent metal atoms [137,225]. As schematically depicted in Fig. 36(b), the development of a highly ramified structure instead of compact metal aggregates, can be conclusively explained in this way.

Apart from Pd, Rh deposition also leads to the generation of a carbonyl compound on the alumina film, if carried out in an ambient CO atmosphere [115]. Here, however, larger amounts of deposited material are necessary to observe the characteristic sharp thermal desorption feature occurring for Rh at 345 K.

Changes of the growth behaviour to such an extent are, of course, an extreme situation. In other cases, only alterations of the particle morphology or the particle sizes may be detectable. Effects of that kind have been discovered for the system $Co/Al_2O_3/NiAl(110)$ [100,218]. By deposition in an ambient CO atmosphere (3×10^{-7} mbar), a modified particle-size distribution is created, which is distinguished by a reduced number of very small particles. This hints at an increased mobility of the adatoms on the surface, i.e. a lowering of the diffusion barriers, due to the adsorbate.

5. Metal particles: electronic structure

Essentially, the electronic structure of small deposited metal particles can be influenced by two factors, differentiating them from the bulk material: (a) their limited size and (b) specific metal–support interactions. We deal with both issues separately, in the course of the following two subsections.

5.1. Particle size effects

For metal particles not too large, it can be expected that distinct changes of the electronic structure occur as a function of size. In the VB, for example, discrete energy levels should be observable for very small clusters and, in the gas phase, it has indeed been possible to detect such a behaviour (see Refs. [140,226] and references therein). This phenomenon, called *quantum size effect*, is limited to sizes of up to about 100 atoms. Beyond this size, a band of states will be formed, the width of which roughly scales with the square root of the average co-ordination number in the aggregate [66,208].

For supported-metal clusters, however, the evolution of discrete states cannot

usually be observed, even for very small cluster sizes. This is probably due to the coupling to the substrate (e.g. to the phonons in the case of oxide supports) coming into play here. Nevertheless, clear variations of the shape and width of the *valence band* have been reported for supported clusters as well (see, for example, Refs. [66,141,208,227–229]). In Fig. 37, an example is taken from our own work [95]. The figure shows valence photoemission spectra, which have been recorded for increasing amounts of Pd deposited onto the thin alumina film at 90 and 300 K. Starting with the growth at 90 K (left), already at the smallest coverage a new feature emerges at 3.5 eV, which can be attributed to the Pd 4d states. In following the course of the spectra, three trends are discernible: (a) the width of the VB increases from about 2.5 to 5 eV, (b) the structure of the band becomes more pronounced and (c) the Fermi energy of the deposits shifts to lower BE (i.e. towards the Fermi edge of the NiAl crystal) as the exposure increases. While the first findings can be easily understood on the basis of the considerations mentioned above, the shift of the Fermi energy reflects the shift of the core levels, discussed in the next paragraph [65]. Since much larger aggregates are formed at 300 K, the development of the Pd induced features is different here. In this series (on the right), the Pd 4d states seem to evolve progressively with the amount of metal deposited. Moreover, intensity at the Fermi edge (of the NiAl substrate) is already detected for the smallest coverages, in sharp contrast to the situation at

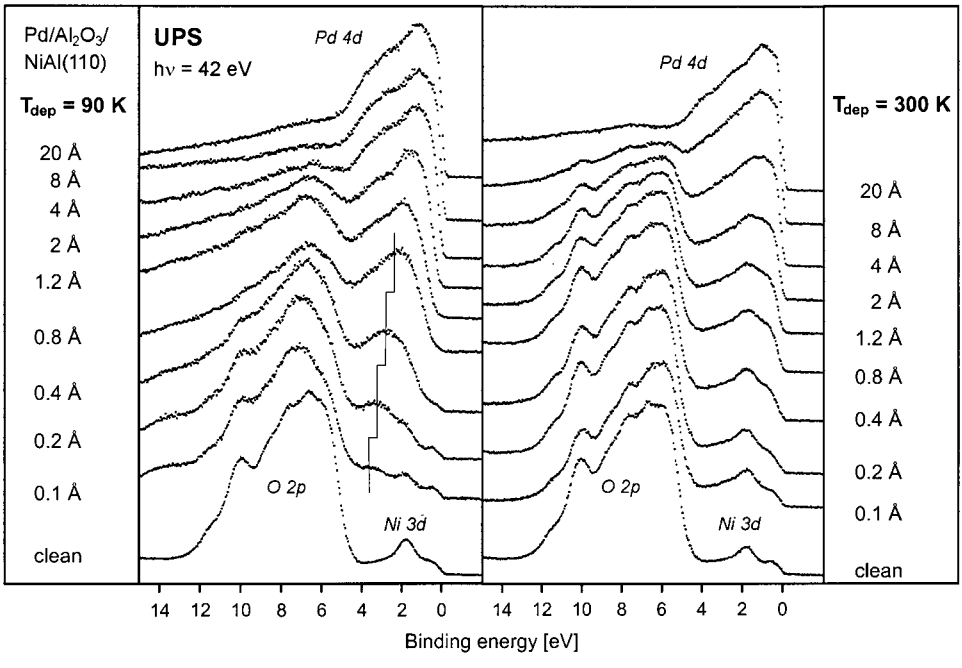

Fig. 37. Valence photoemission spectra (grazing emission) of Pd deposited onto Al_2O_3/NiAl(110) at 90 K (left) and 300 K (right).

90 K. (Note that at 90 K this is not the case up to a nominal film thickness of at least 0.4 Å.)

As mentioned in Section 2.4, the core levels are often subject to size-dependent alterations as well. For the system $Pd/Al_2O_3/NiAl(110)$, this is demonstrated in Fig. 38 containing the Pd 3d spectra for three different preparations: 0.2 Å and 2 Å Pd deposited at 90 K, as well as 12 Å deposited at 300 K with and without adsorbed CO [142]. Note that, for the 12 Å deposit, bulk and surface component are clearly separated after CO saturation, due to an adsorbate induced increase of the surface core level shift from −0.3 to +0.8 eV [142]. Since for the smaller particles no discernible splitting of the peaks occurs upon CO adsorption, it can be concluded that the bulk component is negligible (∽7% for 2 Å and 0% for 0.2 Å) [142]. The trend observed for the clean as well as for the CO covered particles is a clear BE shift to higher values accompanied by a considerable line broadening as their size decreases.

In principle, initial and final state effects can be responsible for BE shifts as a function of the particle size. In the present case, the behaviour seems to be largely determined by the latter effect. If the BEs are plotted as a function of the reciprocal particle diameter (see Fig. 38b), a straight line is found, suggesting that the Coulomb energy of the final state is decisive [7,190]. As expected, the effect is

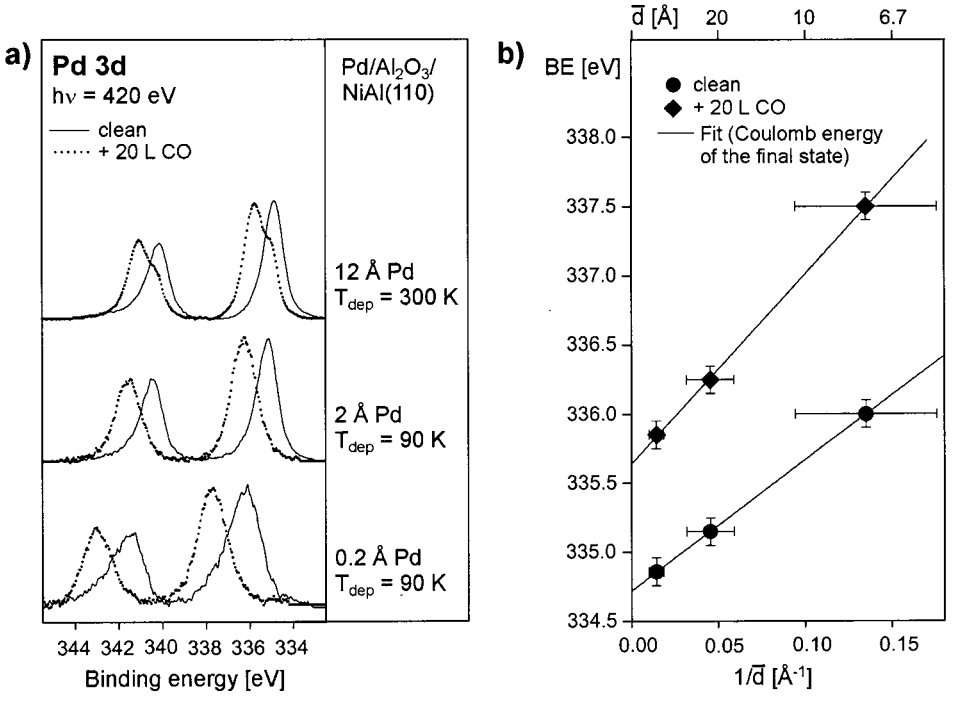

Fig. 38. (a) Pd 3d photoelectron spectra of Pd deposits on $Al_2O_3/NiAl(110)$ with and without adsorbed CO (spectra taken at 90 K). (b) Binding energy as a function of the reciprocal particle diameter $\bar{d}$.

more pronounced after CO adsorption, since this reduces the density of states near the Fermi level, and therefore the screening ability of the clusters.

Concerning the line broadening, several origins have to be taken into account. Due to the $\langle d \rangle^{-1}$ dependence of the BE, the width of the particle-size distribution plays a crucial role of course [66,208]. In the same way, all other features which increase the variety of BEs, will contribute, such as differently co-ordinated metal atoms or atoms with different surroundings (metal atoms inside the particle vs. atoms at the interface). On the other hand, the line width is strongly influenced by the screening ability, and hence, by the VB structure. It has been proven, for instance, that a reduced VB width will actually lead to a broadening of the core levels [143,230].

Apart from Pd, Rh deposits on the thin alumina film also show a $\langle d \rangle^{-1}$ dependence of the BEs (with and without CO), as is illustrated in Fig. 39. It is important to note, however, that the BEs of the smallest CO covered clusters are already in a regime which is typical for deposited carbonyl *compounds* [144]. In this context, we refer to results presented in Section 6, which suggest that a transition of the electronic structure from a metallic to a more molecular character takes place. The fact that the BEs still follow the $\langle d \rangle^{-1}$ law represents no contradiction, as proven by recent theoretical calculations of Rösch and co-workers [145].

5.2. Metal–support interaction

The interaction of metals with oxide surfaces is an important issue in all technological areas which rely on metal–ceramic interfaces. Obviously, one central question refers to the nature and strength of the metal–oxide bonding, as factors which determine the adhesion energy, for example [146]. Generally speaking, two borderline cases can be envisioned, i.e. localised chemical bonds (ionic/covalent) or a charge redistribution between the metal overlayer and the oxide support (or the metal–substrate, if a thin oxide film is used). Whereas characteristic chemical shifts of the states involved, result in the first case, a simultaneous shift of all core and valence levels of the substrate should be detectable in the latter case (*band bending effect*), due to the change of the electrostatic potential.

In many experimental studies of metal deposition onto oxides, electron transfer between the metal and the oxide, resulting from one or other mechanism have been encountered. As gathered from the review of Campbell [4], the formation of cationic metal species is not unusual for small coverages up to 0.1ML (see also Refs. [147–149,231–236]), although charge transfer from the oxide to the metal has occasionally been described as well [150,151,237]. In case of easily reducible oxides, such as TiO_2, oxidation of the metal is, of course, not unexpected. For early transition metals, this is consistent with thermodynamic predictions [4]. Partial oxidation, however, has also been reported for deposition onto oxides, such as alumina, which are not easily reduced [149,235,236]. For the thin alumina film, for instance, vanadium deposition results in a cationic species with an oxidation state between $+1$ and $+2$ in the coverage regime up to 0.1ML [125]. At

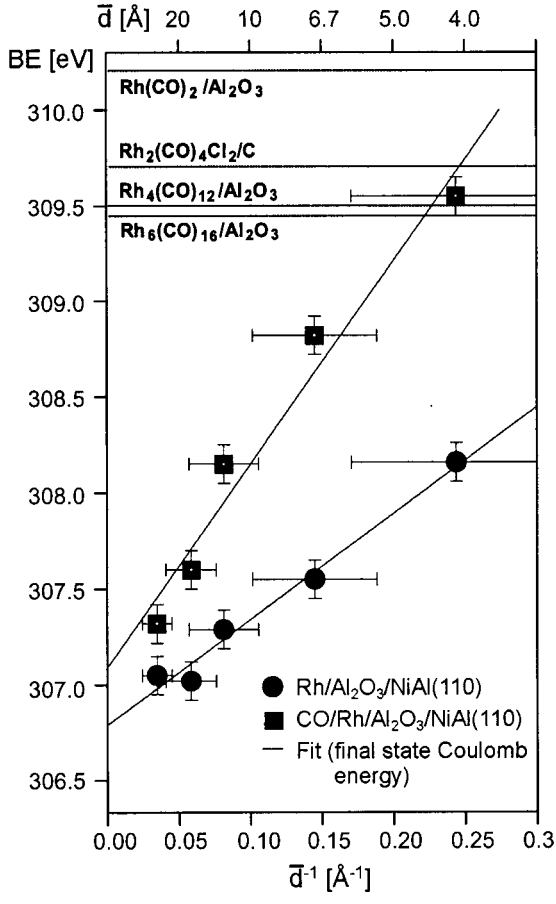

Fig. 39. Rh 3d binding energies as a function of the reciprocal diameter $\bar{d}$ for clean and CO saturated Rh particles on Al_2O_3/NiAl(110). The binding energies for the deposited carbonyl compounds have been taken from [144].

higher coverages, on the other hand, a metallic overlayer is formed. Another example is the system $Al/Al_2O_3/NiAl(110)$. Here, it was clearly demonstrated that a charge transfer from the aluminium to the metallic interface takes place, giving rise to the band-bending effect alluded to above [152].

Although a conclusive picture of the interaction between metals and supports, such as alumina and magnesia, is still missing, most theoretical studies suggest that the primary interaction takes place between the oxygen 2p bands and the d and sp states of the metal [153,154,238–242]. Due to the increasing occupation of the d states, this interaction becomes repulsive for the late transition metals [153,154,238–242], in line with the observation of decreasing adhesion energies. It is interesting to note that some recent theoretical investigations have revealed

substantial ionicity, in case of metal deposits on alumina. In a calculation of Pacchioni and Rösch, for example, partial oxidation has been predicted for small Ni clusters on alumina [155]. For isolated metal atoms, up to a coverage of 1/3 ML, Jennison and co-workers have found strong ionic bonding in the case of several metals on sapphire, as well as on a thin alumina film [156,243]. On the other hand, the calculations clearly demonstrate that the metal–substrate bonds are always weaker than the metal–metal bonds, in line with the 3D growth mode generally found on these supports (see Section 4) [154,240–242].

6. Metal particles: adsorption behaviour

Small deposited metal particles can exhibit strongly size-dependent adsorption and catalytic properties, sometimes differing substantially from the behaviour of single-crystal surfaces [1]. In order to explain this, we have to distinguish between two possible origins. On the one hand, features of the particles directly affecting the interaction with the admolecule have to be taken into account. On the other hand, the structural heterogeneity of the composite system can be the origin of an extraordinary adsorption and reaction behaviour, i.e. it can be governed by adsorption effects on the support or characteristic diffusion controlled kinetic effects.

In various cases, it has, for instance, been shown that physisorbed gas molecules diffusing on the oxide support act as precursors for the adsorption on the metal particles themselves, thus changing the adsorption probability [157,158,244,245]. If reactions are studied on such systems, spill over processes, diffusion between different facets or between facets and corner sites might result in new and unique kinetic phenomena [159,246]. Issues of this kind, however, are not considered in the following.

We essentially focus on the first aspect, i.e. factors which influence the bonding of an adsorbate to a deposited metal particle of varying size. Here, electronic as well as geometric features can be of importance:

- Electronic effects: for very small metal clusters, the adsorption behaviour or the catalytic activity might be directly related to the particular electronic structure of the deposits. In fact, this has been observed in studies with deposited mass selected clusters consisting of just a few atoms ($N < 20$) [84]. However, even if the particles are larger and quantum-size effects are not of relevance, it has to be kept in mind that the electronic structure could still be rather different from the bulk electronic structure. Furthermore, a strong interaction between the metal and the support can, of course, lead to an unusual behaviour, as well. In particular, this should be the case for 2D islands, where all metal atoms are in direct contact with the support.
- Geometric effects: apart from the overall electronic properties, the local electronic structure, i.e. the local density of states, at an adsorption (or reaction) site is certainly an important factor which, in turn, depends on the

local geometric arrangement of the surface atoms at that site [160]. It is, for example, possible that a reaction can only occur if an ensemble of atoms in a particular geometry is available on a surface [1]. Since small metal aggregates expose a large variety of differently co-ordinated surface atoms, strong size effects can be the consequence. Of course, this is especially expected in case of disordered aggregates exhibiting a high defect density, i.e. a large number of co-ordinatively unsaturated metal atoms. But geometric effects have to be taken into consideration for crystalline aggregates as well, since the number of edge and corner sites increases with decreasing size [1]. Furthermore, the proportion of facets with different crystallographic orientations may be subject to changes.

In the following, we give a few examples based on the above systems, which illustrate some of these effects. We have chosen CO as a probe molecule for our studies, since the literature provides a large fund of knowledge regarding the adsorption behaviour of this molecule on single-crystal surfaces, which thus offers the advantage of a direct comparison. In addition, CO is an interesting candidate, because its dissociation ability on transition metals provides a simple test of the reactivity as a function of particle size and structure.

6.1. CO adsorption

The adsorption of gases on metal surfaces is, of course, coverage dependent. While at low coverages the bonding to the substrate is decisive, adsorbate–adsorbate interactions increasingly add to this at higher coverages. For CO adsorption on small Pd particles, Henry and co-workers have demonstrated, for example, that, in the *low coverage regime*, the adsorption energy increases with decreasing particle size [161]. This is consistent with the intuitive expectation of tighter binding sites on low co-ordinated metal atoms being characteristic of very small aggregates. Apart from the low coverage regime, however, it is interesting to study the adsorption properties at *higher coverages* as well, where collective phenomena may finally lead to a totally different behaviour as a function of particle size. Thus, the studies presented here deal with the regime near saturation.

6.1.1. Platinum

The adsorption properties of the Pt deposits on Al_2O_3/NiAl(110) have been investigated by means of various methods [121,162]. In this context, however, we wish only to discuss the TD spectra compiled in Fig. 40. Starting with the highest exposure, features are found that resemble the desorption spectra of Pt single crystals, which are displayed for comparison [163,164]. Obviously, the spectrum contains peaks of the low-index Pt(111), as well as peaks typical for strongly stepped surfaces, which reveals an appreciable amount of step and other defect sites. In fact, a similar behaviour has also been reported for small Pt particles on α-Al_2O_3 [165].

If the exposure is decreased, the fine structure of the spectrum is lost and the maximum of the broad feature shifts to higher temperatures. Moreover, a new

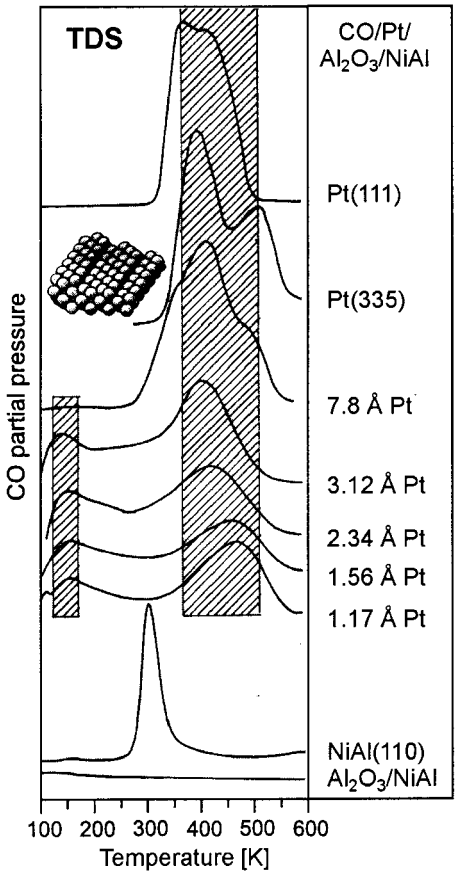

Fig. 40. Thermal desorption spectra for the system $CO/Pt/Al_2O_3/NiAl(110)$. For comparison, the TD spectra of two Pt single crystal surfaces [163,164] as well as the spectra for the clean alumina film and the NiAl substrate are included.

desorption feature at around 150 K is observed, which is not compatible with CO desorbing from *metallic* Pt. Since the structural characterisation of the system points to a rather strong interaction with the support, it is reasonable to attribute this feature to a modified electronic structure of the deposit, i.e. a partial oxidation resulting, for example, from an incorporation into the first layer of the alumina film. Such an explanation is corroborated by CO adsorption experiments on transition-metal oxide surfaces yielding desorption temperatures in the range between 150 and 200 K [166,247,248].

6.1.2. Palladium

Starting with the TD spectra for different particle sizes first (see Fig. 41b), it is interesting to notice that a low-temperature desorption peak (between 150 and

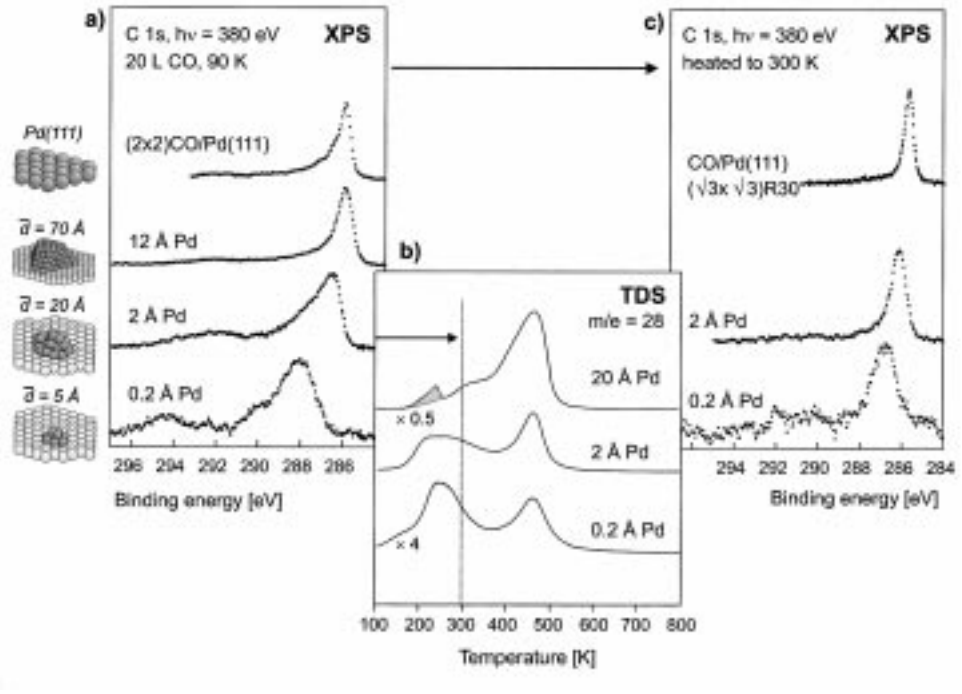

Fig. 41. CO adsorption on Pd particles of different size deposited onto Al_2O_3/NiAl(110): (a) C 1s spectra (taken at 90 K after CO saturation) including the spectrum of (2 × 2) CO/Pd(111) [169]; (b) TD spectra (feature marked grey is an experimental artefact); (c) C 1s spectra taken after heating to 300 K (measurement at 90 K) together with the spectrum for $(\sqrt{3} \times \sqrt{3})$CO/Pd(111) [169].

350 K) again evolves as the particle size decreases [116]. Incidentally, these spectra are reminiscent of data reported by other groups for small Pd particles on various alumina supports [168,249,250]. (Although the TD spectra shown in these publications were recorded with a starting temperature of 300 K, the authors also observe shoulders below 500 K, which become the predominating peaks as the particle size decreases.) The spectrum obtained for the highest exposure at 300 K, on the other hand, essentially corresponds to the desorption behaviour of a Pd(111) surface [167], in line with the formation of large (111)-crystallites under these conditions. Since, in contrast to Pt, our experiments concerning the electronic and geometric structure provided no evidence for a specific metal–support interaction, more elaborate experiments have been carried out in order to investigate the origin for this distinct size dependence.

Fig. 41(a) shows a series of high resolution C 1s core level spectra for different particle sizes prepared at 90 and 300 K [74,95,142]. For comparison, the spectrum for a CO (2 × 2) overlayer on Pd(111) ($\theta = 0.75$) is included [169]. Three aspects are conspicuous in this series: (a) a shift of the peak towards higher BEs as the particles size decreases, (b) an increasing line broadening connected with the development of a strong asymmetry on the high BE side and (c) a clear increase

of the shake-up intensity (at about 6 eV higher BE). The first effect, which is due to the Coulomb energy of the final state, has already been dealt with in Section 5. Concerning the second observation, it is important to note that even the spectrum for the single crystal exhibits a slight asymmetry. Since different CO adsorption sites can lead to BE shifts of about 0.5–1 eV with more highly co-ordinated sites showing lower BE [170,251], this has been interpreted in terms of molecules adsorbed in different adsorption geometries, as previously identified by vibrational spectroscopies (on-top and three-fold hollow site: see below) [142]. Therefore, the broader peaks for the 90 K deposits can, to a certain extent, be explained by a multitude of adsorption sites becoming available on the smaller and disordered aggregates growing under these conditions. It should be borne in mind, however, that some of the effects discussed in Section 5.1 may contribute to the broadening as well. The third point sheds light on the metal CO interaction itself. Since stronger satellites are normally found for more weakly bonded adsorbates [171,172,252], the increasing shake-up intensity indicates a decreasing CO–Pd interaction strength, which is, of course, supported by the CO TD spectra.

If that part of the CO molecules desorbing below 300 K is removed, some informative changes in the C 1s spectra take place. The corresponding spectra for the 90 K deposits as well as the spectrum for the $(\sqrt{3} \times \sqrt{3})$ phase of CO/Pd(111) ($\theta = 0.33$) [169], are presented in Fig. 41(c). (Based on the changes in the peak intensities, it can be estimated that about 60% of the original coverage desorbs from the particles.) On the one hand, the peaks become significantly narrower and more symmetric. This points to a decrease in the number of different CO adsorption sites. It can be speculated that it is the highly co-ordinated CO which remains on the particles, since, on Pd(111) the vanishing of the shoulder at the high BE site reveals the loss of the low co-ordinated species, in line with vibrational spectroscopic (see below) and *X-ray photoelectron diffraction* (XPD) results [173]. On the other hand, a clear reduction of intensity of the shake-up satellite is detected. According to the above arguments, this suggests that the CO–Pd interaction is stronger for the remaining species.

Further information about the latter aspect can be derived from the X-ray absorption spectroscopy (XAS) data depicted in Fig. 42 [74]. The spectra have been recorded at the position of the so-called π *resonance* resulting from the excitation of a C 1s electron into the empty 2π orbital of the CO molecule. Since the bonding of CO on transition metals gives rise to a broadening of the π orbital, due to the hybridisation between the CO 2π orbital and the metal d band, the width of the resonance can be correlated with the adsorbate–substrate interaction [174,253]. (Note that, in principle, this correlation is strictly valid only for the core-excited state, but it may be taken as a measure for the ground-state interaction as well.) Thus, the series corroborates the above findings, namely, that the Pd–CO interaction weakens with decreasing particle size and increases again after diluting the CO overlayer by annealing. Obviously, the latter effect is most pronounced for the smallest aggregates, thus distinguishing themselves by a strong CO coverage dependence of the chemisorption strength.

Combining the XPS and XAS results, gives further insight into the electronic

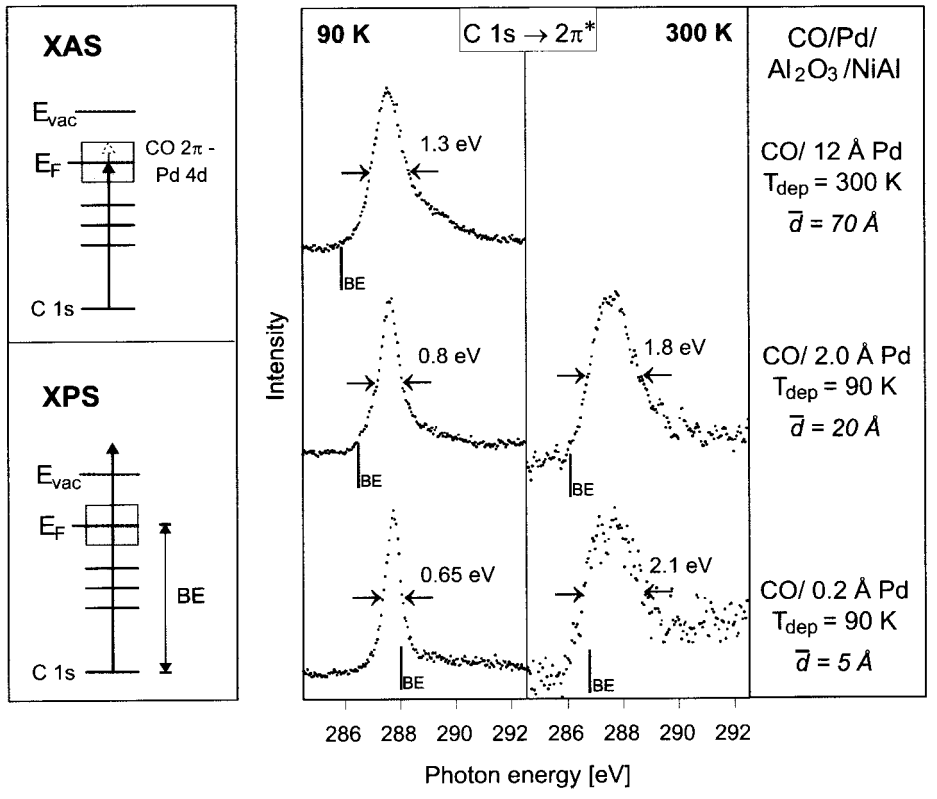

Fig. 42. C 1s → 2π* XA spectra of the system CO/Pd/Al_2O_3/NiAl(110) after CO saturation at 90 K and after annealing to 300 K (spectra taken at 90 K). The lines indicate the positions of the XPS BE. The relationship between XPS BE and XAS PE for a metallic system is illustrated on the left.

structure of the CO covered particles, since the relative positions of the XPS BE (relative to the Fermi level) and the XAS edge are determined by the ability of the system to screen the core hole created during the photoemission process. This ability is, of course, dependent on whether the aggregates have metallic or rather molecular character. In fact, it was found that for CO adsorbed on metals, the XPS BE if measured relative to the Fermi energy always appears near the onset of the XAS peak [174,253]. This relation is a consequence of the hybridisation between the electronic levels of the adsorbate and the metal allowing for efficient charge transfer screening of the core ionised molecule. In this case, the fully screened state having the lowest energy is the one with a core hole and a screening electron at the Fermi level. On the other hand, this also represents, of course, the final state of the XAS process, leading to the above relationship. In contrast, this correlation does not hold for molecular systems.

In Fig. 42, the XPS BEs have been marked with lines and it is obvious that the XPS BE gradually moves from a position at the onset to a position slightly above

the maximum of the resonance for the smallest particles. Accordingly, the larger particles indicate their metallic character, as expected. For decreasing particle sizes, however, a transition to a more molecule-like behaviour seems to take place, although this is only the case at saturation coverage. The screening provided for the species, which are left after desorption of more than half of the overlayer, is again similar to a metallic system.

Naturally, the question arises why such strong differences regarding the adsorption properties are observed for the small Pd particles. In this respect, the quantitative evaluation of the integral TDS intensities and the XPS intensities supply an important piece of information [175]. On the basis of these intensities and the structural data, it is possible to calculate the number of adsorbed CO molecules per Pd surface atom increasing from $\backsim 1$ (cf. the saturation coverage for Pd(111): 0.75) to about 1.5 to 2 for the smallest particles studied here. It is easy to imagine that this higher co-ordination of the metal atoms induces stronger repulsive CO–CO interactions and a weakening of the Pd–CO bond and also a reduced screening ability.

In order to tackle the question of adsorption sites in more detail, the electron spectroscopic measurements have been complemented by an IRAS study [82,212]. Before turning to these results, which are displayed in Figs. 43 and 44, it is helpful to recall what is known for Pd single crystals first. For coverages between $\theta = 0.1$ to 0.5, the preferred adsorption site on Pd(111) is the three-fold hollow site [173] with CO stretching frequencies ranging from 1830 to 1920 cm^{-1} [86,176]. If the coverage is increased to 0.6–0.7, the site changes and bridge-bonded species with stretching frequencies between 1960 and 1970 cm^{-1} are observed [177,178]. Raising θ to the saturation coverage of 0.75, two intense bands at 1894 and 2110 cm^{-1} are finally detected, which are attributed to terminally-bonded CO (2110 cm^{-1}) accompanied by a species in three-fold hollow sites (1894 cm^{-1}) [177,178]. This is in sharp contrast to the Pd(100) surface, on which a CO stretching frequency of 1997 cm^{-1} is measured at saturation coverage [179].

Fig. 43 provides an overview of the spectra taken for different particle sizes prepared at 90 and 300 K after CO saturation. Starting with the spectra for the large aggregates grown at 300 K, essentially three bands are visible: 1953, 1994 and 2105 cm^{-1}. As the deposits are crystalline (see Section 4.1), the first peak can be assigned to bridge-bonded CO on (111) facets, whereas the last feature is obviously caused by terminally-bonded CO. Regarding the remaining band, it is tempting to ascribe it to CO on Pd(100) facets, as previously done in the literature [85]. Taking, however, the particle morphology into account (see Figs. 28 and 29), this interpretation seems unlikely, because the (100) facets are in the minority. Therefore, the suggestion has been put forward that this band is mainly due to bridge-bonded CO molecules on the particle edges. The only puzzling detail then is its high intensity, which can be explained by intensity borrowing from the adjacent line at 1953 cm^{-1} [131]. It is worth noting in this context that there is a difference with respect to the Pd(111) single crystal surface exhibiting no bridge-bonded CO but a species in a three-fold hollow site at saturation coverage. In

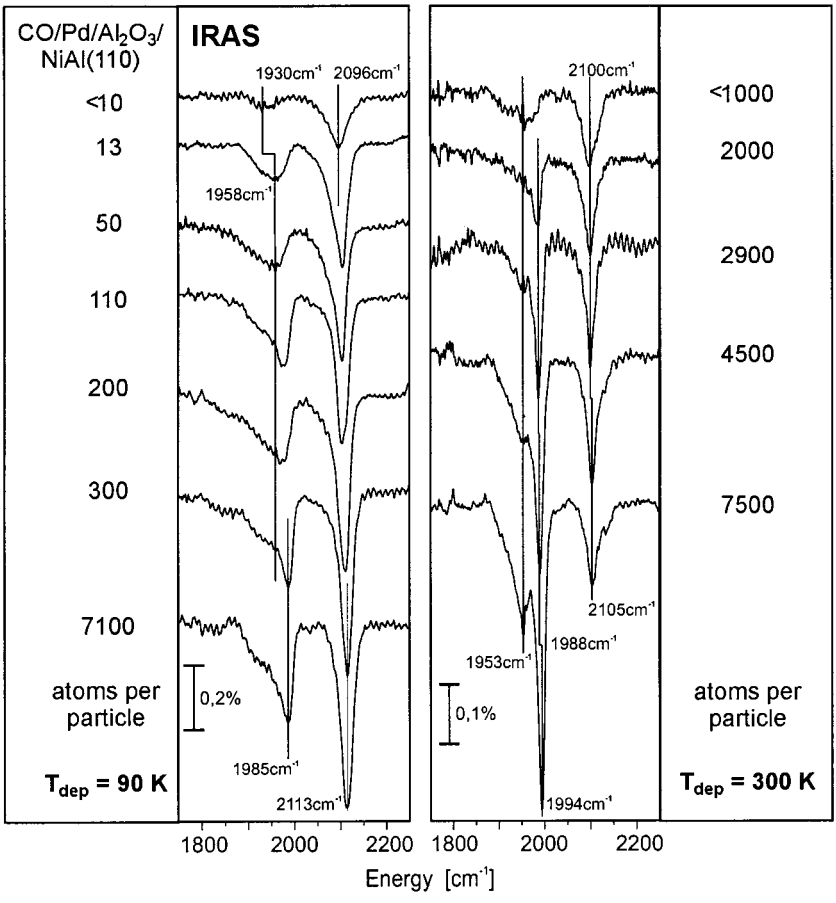

Fig. 43. IR spectra of CO adsorbed on Pd particles of various size grown on Al_2O_3/NiAl(110) at 90 and 300 K (CO saturation coverage, spectra taken at 90 K).

fact, the aggregates rather resemble the behaviour of a roughened, less ordered Pd(111) surface [179].

Proceeding to the spectra of the smaller particles prepared at 300 K and the series for the 90 K deposits, the positions of the bands are comparable, but their half widths increase, especially for the 90 K deposits. The latter observation again underlines the higher degree of heterogeneity with respect to the available adsorption sites on the less ordered aggregates formed at 90 K. It is interesting to see that the absorption band for on-top CO clearly increases as the particle size decreases. Apparently, the occupation of terminally-bonded CO is strongly preferred on small aggregates, and it might be speculated whether this is for steric or electronic reasons. Anyhow, this preference is a rather general phenomenon for at least Rh, Pd and Ni deposits, as proven by a number of similar reports in the

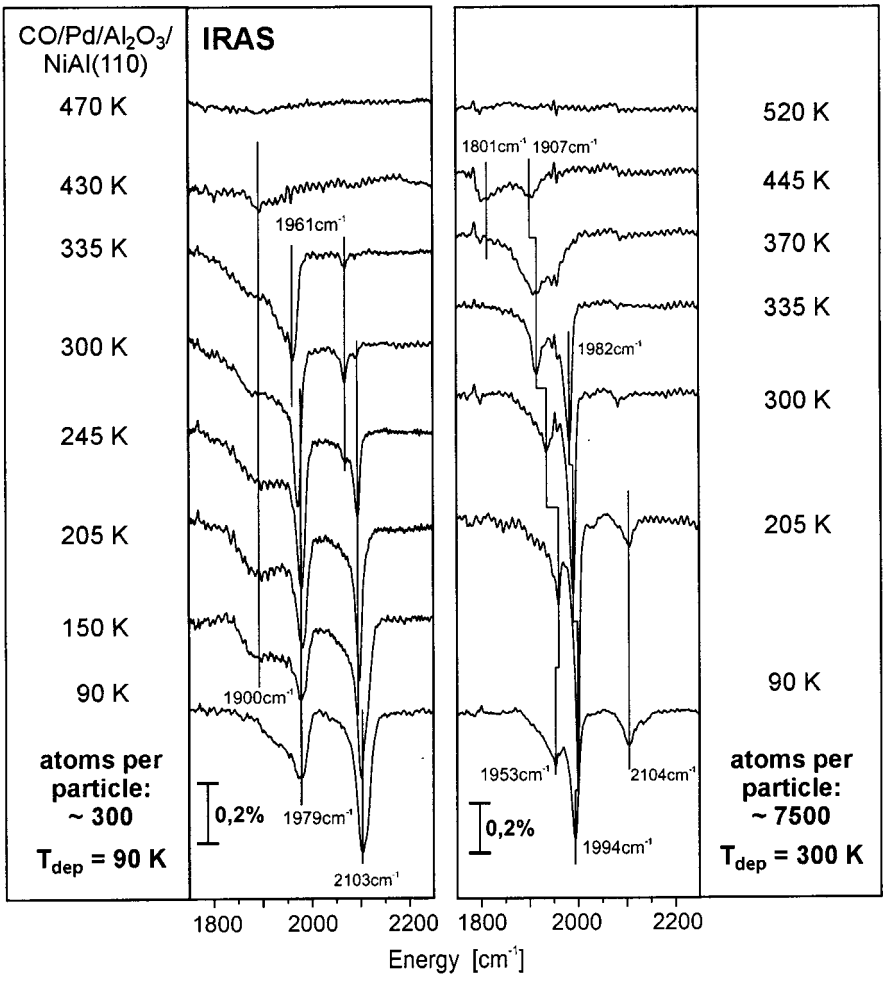

Fig. 44. IR spectra of CO adsorbed on Pd particles grown at 90 and 300 K after saturation at 90 K (20 L) and annealing to the indicated temperatures (spectra taken at 90 K).

literature (see Ref. [4] as well as Refs. [10,180,191]) and our own studies on Rh particles [181].

Fig. 44 shows a temperature series for a 90 and 300 K preparation. Without going into details, the spectra clearly demonstrate that indeed the terminally-bonded CO species desorb first, as already tentatively inferred from the XPS data. For the smaller particles grown at 90 K, this behaviour is particularly pronounced. In case of the 300 K deposits, the next desorbing species are the bridge-bonded molecules on the edges. Apart from the remaining bridge-bonded CO on the terraces, another species appears at 445 K, which can be identified as CO on a three-fold hollow site in analogy to CO/Pd(111).

6.2. CO dissociation

From a single-crystal study on Rh(210), it is known that CO adsorbs dissociatively on stepped Rh surfaces [182], whereas no dissociation occurs on the close-packed Rh(100) [183] and Rh(111) [184] faces. Thus, defects, i.e. co-ordinatively unsaturated Rh atoms, are decisive for the CO dissociation activity on Rh. According to a classification introduced by Boudart [185], this points to a 'structure sensitive' reaction, suggesting that a strong particle-size dependence may be expected. In order to follow up this question, a detailed XPS study of the CO adsorption properties on $Rh/Al_2O_3/NiAl(110)$ has been conducted, which we now discuss here [186–188][2].

As shown in Fig. 45, the dissociation process can be clearly traced in the C 1s spectra taken after CO saturation at 90 K and subsequent annealing to the indicated temperatures. Due to molecularly adsorbed CO, a peak at about 286 – 287 eV is initially visible in the spectrum. This gradually transforms into a new feature at 284 eV, which is typical for atomic carbon. (Note that some minor carbon contaminations were already detectable at 90 K probably caused by dissociation of background CO). Finally, a 600 K, no molecularly adsorbed CO is present on the surface any more.

Naturally, *two* processes contribute to the loss of CO in the course of the temperature series carried out here: desorption and dissociation. In order to quantify the dissociation fraction, the area of the atomic carbon peak at 600 K (diminished by the area of carbon contributions at 90 K) and the area of the original CO peak have been determined. The ratio of the first to the second area then represents the dissociated part. In Fig. 46, this quantity is plotted as a function of the average number of atoms per particle revealing a maximum for Rh particles of about 200 atoms. Accordingly, the dissociation activity does indeed exhibit a strong size dependence, passing a maximum for *medium sized aggregates*.

Although electronic effects cannot completely excluded for very small particles, an explanation for this behaviour on the basis of the structural properties of the system seems most likely. Since the Rh deposits are basically disordered, it is easy to imagine that aggregates of medium size exhibit a maximum defect density in terms of steps, kinks and other low co-ordinated surface atoms. Smaller units should contain less defects, in particular, if they are still 2D. In addition, spatial constraints may play a role here as well (accommodation of C and O on adjacent sites, see Fig. 45). At high exposures, the step density is reduced, due to coalescence processes. For deposition at 300 K, the observed tendency to form crystalline aggregates in the high-coverage regime is another factor contributing to

[2] Remark: There is a discrepancy between the data discussed in Ref. [186] and the more recent results presented here. According to the older work, the maximum of the CO dissociation activity is found at somewhat larger particle sizes ($\sim$1000 atoms per particle as compared to 200 atoms, see Fig. 46). This was due to a miscalibration of the metal evaporator used in our first experiments. A corresponding erratum has been submitted to Chem. Phys. Lett.

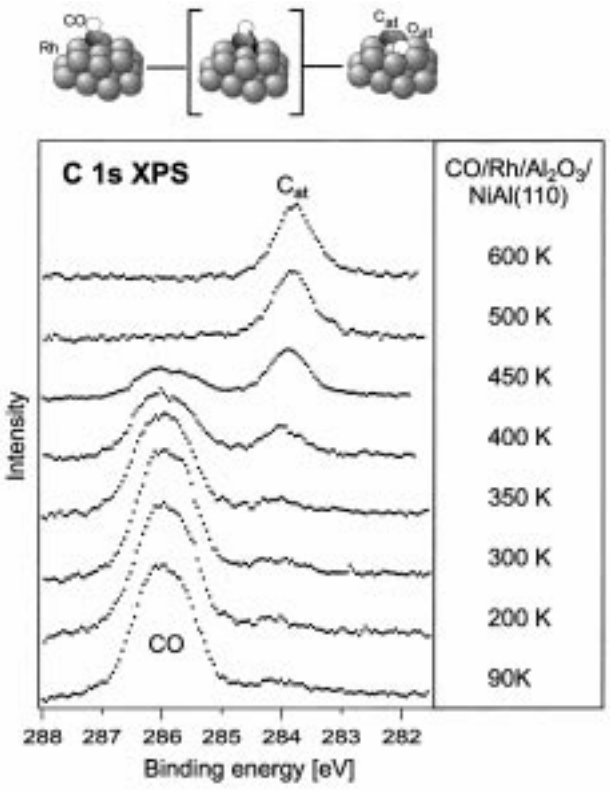

Fig. 45. CO dissociation on $Rh/Al_2O_3/NiAl(110)$: representative series of C 1s spectra taken after CO saturation at 90 K and heating to the indicated temperatures (data acquisition at 90 K).

a lower defect density. This is consistent with the observation that the dissociation activity declines much faster in this case (see Fig. 46).

An interesting detail concerning the dissociation process has been discovered by a closer inspection of the C 1s emission of the molecularly adsorbed CO [187]. As demonstrated in Fig. 47(a), the peak actually consists of two components, denoted by A and B. The intensity ratio of both components is temperature and particle size depended. At 300 K, the fraction of the total intensity found for component B passes a maximum as a function of particle size [187]. If compared to the fraction of CO finally dissociating (see Fig. 46), it turns out that the evolution of these two quantities is identical, i.e. the maximum is found at the same point [187]. Thus, B seems to be a kind of dissociation precursor. At 90 K, however, the situation is different. Here, the relative intensity attributed to B is nearly the same for all particle sizes [187]. Consequently, it is the heating step which causes a shift of intensity from component A to component B, i.e. an increase of the B species which is most pronounced for the medium-sized particles. Interestingly, this

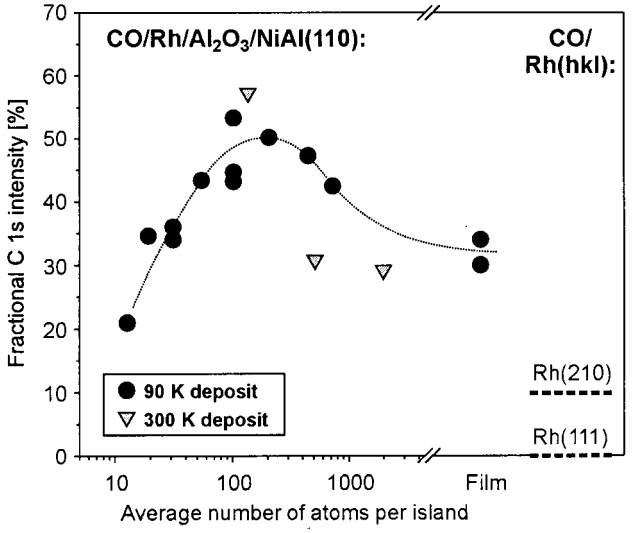

Fig. 46. CO dissociation activity on Rh particles deposited on Al_2O_3/NiAl(110) as determined by XPS. According to [186,187] the dissociation activity also passes a maximum for the 300 K deposits, i.e. the activity decreases in the regime of small particle sizes reflecting the behaviour of the 90 K deposits.

conversion is irreversible. Cooling down to 90 K does *not* lead to an intensity redistribution again.

The conclusion that B is indeed a dissociation precursor is additionally corroborated by Fig. 47(b), showing the intensity changes for the A and B peaks as well as the losses which result either from desorption or dissociation [188]. Unambiguously, the desorption curve follows the curve for component A, whereas, the dissociation curve mimics the development of the component B.

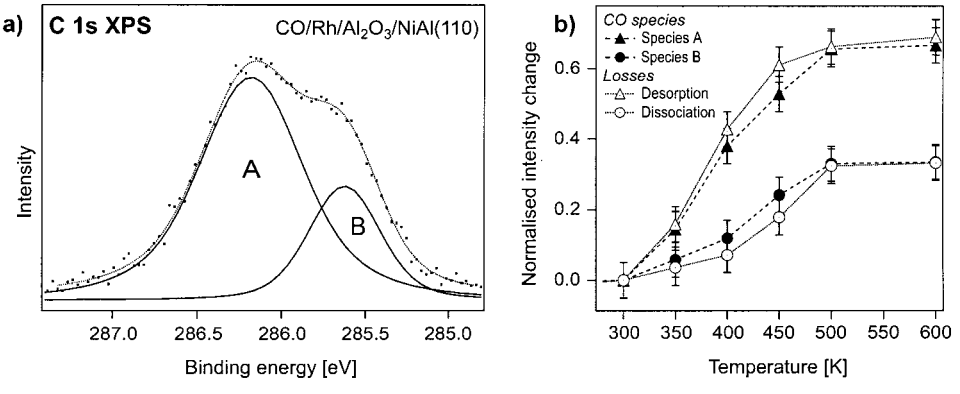

Fig. 47. (a) C 1s spectrum of CO adsorbed on Rh particles after saturation at 90 K; (b) Intensity changes for the components A and B as well as the intensity losses due to dissociation and desorption as a function of the annealing temperature (average particle size: $\sim 10^4$ atoms).

Unfortunately, the results allow no further statement as to the nature of the A and B species. It can be assumed, however, that the B species is connected with CO adsorbed on defects. Based on the fact that higher co-ordinated CO species give rise to lower C 1s BEs (see above), it may be also speculated as to whether B is associated with CO in a higher co-ordination, as compared to the A species.

7. Concluding remarks

Without a doubt, metal–oxide interfaces, metal coatings or dispersed metals on oxide supports play an important part in many technological areas. One of them is heterogeneous catalysis, where supported metal catalysts are used to increase the activity or control the selectivity of industrial reaction processes. Nevertheless, there is still a lack of fundamental knowledge about the essential properties of thin metal films and small metal particles on oxide supports, although a deeper understanding could help to improve the electronic, mechanical or catalytic performance of such systems. Some of the questions which need to be answered in this respect refer to the following topics:

- Electronic properties of deposited metal clusters and thin films: how does the electronic structure develop with increasing size/thickness?
- Metal–oxide interface: what is the nature and strength of the bonding?
- Adsorption and adhesion energies.
- Diffusion of metal atoms on oxide supports.
- Nucleation and growth: what are the activation energies for the elementary steps involved? What is the prevailing nucleation mechanism? Under which conditions are ordered/disordered particles formed? Is the growth process influenced by an ambient of certain gases?
- Interaction with gases: in which way does the interaction strength/adsorption energy change with size? Is the particle shape altered by gas adsorption?
- Catalytic activity: how does the activity/selectivity change with dispersion. Are metal–support interactions of relevance?

It has long been recognised that some of the above questions can be successfully tackled by taking advantage of the large potential of modern surface science techniques. As mentioned in the introduction, a number of different approaches have been proposed and explored since then aiming at the preparation of suitable model systems.

In this review, we have discussed the possibility of using thin, well-ordered oxide films as supports for the study of deposited metal particles. This approach offers the advantage of allowing the unrestricted application of all experimental methods, which rely on a good electrical or thermal conductivity of the sample, such as PES, LEED, STM or TDS. With the help of several examples taken from our own work on a thin alumina film, we have shown that it is feasible to characterise such systems on a microscopic level with respect to all relevant structural, electronic and adsorption properties. In this way, correlations between

these features can be established, thus helping us, to understand the particular chemistry and physics of small metal aggregates.

Acknowledgements

The authors would like to use this opportunity to express their thanks to a number of co-workers who have made essential contributions to the work reviewed in this article: Martin Frank, Michael Heemeier, Ralf Kühnemuth, Jörg Libuda, Matthias Naschitzki, Anders Sandell and Sascha Stempel. Furthermore, we would like to thank the following groups for very successful and enjoyable collaborations in the last years: H. Neddermeyer (Halle, Germany), N. Mårtensson (Uppsala, Sweden) and F. Besenbacher/I. Stensgaard (Aarhus, Denmark). For financial support of our work, we are grateful to a number of agencies: Deutsche Forschungsgemeinschaft (DFG), Bundesministerium für Bildung und Forschung (BMBF), Fonds der Chemischen Industrie and NEDO International Joint Research Grant on Photon and Electron Controlled Surface Processes. This work has also been supported, in part, by Synetix, a member of the ICI group, through their Strategic Research Fund. Regarding the manuscript, we thank M. Frank for critical reading and H. Neddermeyer and C.T. Campbell for allowing to use their figures.

References

[1] M. Che, C.O. Bennett, Adv. Catal. 20 (1989) 153.
[2] P.L.J. Gunter, J.W.H. Niemantsverdriet, F.H. Ribeiro, G.A. Somorjai, Catal. Rev. Sci. Eng. 39 (1997) 77.
[3] C.R. Henry, Surf. Sci. Rep. 31 (1998) 231.
[4] C.T. Campbell, Surf. Sci. Rep. 27 (1997) 1.
[5] D.W. Goodman, Surf. Rev. Lett 2 (1995) 9.
[6] U. Diebold, J.-M. Pan, T.E. Madey, Surf. Sci. 331–333 (1995) 845.
[7] H.-J. Freund, Angew. Chem. Int. Ed. Engl. 36 (1997) 452.
[8] U. Heiz, F. Vanolli, L. Trento, W.-D. Schneider, Rev. Sci. Instrum. 68 (1997) 1986.
[9] H.-J. Freund, Phys. Status Solidi (b) 192 (1995) 407.
[10] J.G. Chen, J.E. Crowell, J.T. Yates Jr., Surf. Sci. 185 (1987) 373.
[11] D.N. Belton, S.J. Schmieg, Surf. Sci. 199 (1988) 518.
[12] F. Rochet, S. Rigo, M. Froment, C. d'Anterroches, C. Maillot, H. Roulet, G. Dufour, Adv. Phys. 35 (1986) 237.
[13] M. Bäumer, D. Cappus, H. Kuhlenbeck, H.-J. Freund, G. Wilhelmi, A. Brodde, H. Neddermeyer, Surf. Sci. 253 (1991) 116.
[14] H. Kuhlenbeck, C. Xu, B. Dillmann, M. Haßel, B. Adam, D. Ehrlich, S. Wohlrab, H.-J. Freund, U.A. Ditzinger, H. Neddermeyer, M. Neuber, M. Neumann, Ber. Bunsenges. Phys. Chem. 96 (1992) 15.
[15] D.W. Goodman, J. Vac. Sci. Technol. A 14 (1996) 1526.
[16] R.M. Jaeger, H. Kuhlenbeck, H.-J. Freund, M. Wuttig, W. Hoffmann, R. Franchy, H. Ibach, Surf. Sci. 259 (1991) 235.
[17] J. Libuda, F. Winkelmann, M. Bäumer, H.-J. Freund, Th. Bertrams, H. Neddermeyer, K. Müller, Surf. Sci. 318 (1994) 61.

[18] P. Gassmann, R. Franchy, H. Ibach, Surf. Sci. 319 (1994) 95.
[19] R. Franchy, J. Masuch, P. Gassmann, Appl. Surf. Sci. 93 (1996) 317.
[20] U. Bardi, A. Atrei, G. Rovida, Surf. Sci. 268 (1992) 87.
[21] C. Becker, J. Kandler, H. Raaf, R. Linke, T. Pelster, M. Dräger, M. Tanemura, K. Wandelt, J. Vac. Sci. Technol. A 16 (1998) 1000.
[22] H. Graupner, L. Hammer, K. Heinz, D.M. Zehner, Surf. Sci. 380 (1997) 335.
[23] Ch. Uebing, Ber. Bunsenges. Phys. Chem. 102 (1998) 1156.
[24] C. Xu, D.W. Goodman, Chem. Phys. Lett. 263 (1996) 13.
[25] M.-C. Wu, J.S. Corneille, C.A. Estrada, J.-W. He, D.W. Goodman, Chem. Phys. Lett. 182 (1991) 472.
[26] M.C. Gallagher, M.S. Fyfield, J.P. Cowin, S.A. Joyce, Surf. Sci. 339 (1995) L909.
[27] J. Wollschläger, D. Erdös, K.M. Schröder, Surf. Sci. 402–404 (1998) 272.
[28] S.K. Purnell, X. Xu, D.W. Goodman, B.C. Gates, J. Phys. Chem. 98 (1994) 4076.
[29] R.-P. Blum, D. Ahlbehrendt, H. Niehus, Surf. Sci. 396 (1998) 176.
[30] Y. Wu, E. Garfunkel, T.E. Madey, J. Vac. Sci. Technol. A 14 (1996) 2554.
[31] Y. Wu, E. Garfunkel, T.E. Madey, Surf. Sci. 365 (1996) 337.
[32] P.J. Chen, D.W. Goodman, Surf. Sci. 312 (1994) L767.
[33] M.-C. Wu, D.W. Goodman, J. Phys. Chem. 98 (1994) 9874.
[34] D. Cappus, C. Xu, D. Ehrlich, B. Dillmann, C.A. Ventrice Jr., K. Al-Shamery, H. Kuhlenbeck, H.-J. Freund, Chem. Phys. 177 (1993) 533.
[35] C.A. Ventrice Jr, Th. Bertrams, H. Hannemann, A. Brodde, H. Neddermeyer, Phys. Rev. B 49 (1994) 5773.
[36] C.M. Truong, M.-C. Wu, D.W. Goodman, J. Chem. Phys. 97 (1992) 9447.
[37] W. Weiss, M. Ritter, Phys. Rev. B 59 (1999) 5201.
[38] H.C. Galloway, J.J. Benítez, M. Salmeron, Surf. Sci. 298 (1993) 127.
[39] X.-G. Wang, W. Weiss, Sh.K. Shaikhutdinov, M. Ritter, M. Petersen, F. Wagner, R. Schlögl, M. Scheffler, Phys. Rev. Lett. 81 (1998) 1038.
[40] W. Weiss, A. Barbieri, M.A. Van Hove, G.A. Somorjai, Phys. Rev. Lett. 71 (1993) 1848.
[41] M. Haßel, H. Kuhlenbeck, H.-J. Freund, S. Shi, A. Freitag, V. Staemmler, S. Lütkehoff, M. Neumann, Chem. Phys. Lett. 240 (1995) 205.
[42] A.B. Boffa, H.C. Galloway, P.W. Jacobs, J.J. Benítez, J.D. Batteas, M. Salmeron, A.T. Bell, Surf. Sci. 326 (1995) 80.
[43] V. Maurice, M. Salmeron, G.A. Somorjai, Surf. Sci. 237 (1990) 116.
[44] R. Wichtendahl, M. Rodriguez-Rodrigo, U. Härtel, H. Kuhlenbeck, H.J. Freund, G.A. Somorjai, Phys. Stat. Sol. (a) 173 (1999) 93.
[45] M. Henzler, in: H. Ibach (Ed.), Electron Spectroscopy for Surface Analysis, Topics in Current Physics, 4, Springer, Berlin, 1977.
[46] J. Wollschläger, Defect and Diffusion Forum 164 (1998) 37.
[47] U. Scheithauer, G. Meyer, M. Henzler, Surf. Sci. 178 (1986) 441.
[48] J. Wollschläger, J. Falta, M. Henzler, Appl. Phys. A 50 (1990) 57.
[49] C.S. Lent, P.I. Cohen, Surf. Sci. 139 (1984) 12.
[50] M. Henzler, H. Busch, G. Friese, in: M.G. Lagally (Ed.), Kinetics of Ordering and Growth at Surfaces, Plenum Press, New York, 1990.
[51] P.R. Pukite, C.S. Lent, P.I. Cohen, Surf. Sci. 161 (1985) 39.
[52] R. Wiesendanger, Scanning Probe Microscopy and Spectroscopy, Cambridge University Press, Cambridge, 1994.
[53] D.A. Bownell, Prog. Surf. Sci. 57 (1998) 187.
[54] U. Diebold, in: A.W. Czanderna, C.J. Powell, T.E. Madey (Eds.), Specimen Handling, Treatments, Beam Effects and Depth Profiling, Plenum Press, New York, in press.
[55] Th. Bertrams, A. Brodde, H. Neddermeyer, J. Vac. Sci. Technol. B 12 (1994) 2122.
[56] U. Dürig, O. Zuger, D.W. Pohl, J. Microsc. 152 (1988) 259.
[57] D. Keller, Surf. Sci. 253 (1991) 353.
[58] S. Stempel, M. Bäumer, H.-J. Freund, Surf. Sci. 402–404 (1998) 424.

[59] P. Gallezot, C. Lequercq, in: B. Imelik, J. Vedrine (Eds.), Catalysis Characterization, Plenum Press, New York, 1994, p. 521.
[60] H. Poppa, Catal. Rev.-Sci. Eng. 35 (1993) 359.
[61] M.J. Yacaman, T. Ocana, Phys. Status Solidi (a) 42 (1977) 571.
[62] S.A. Nepijko, M. Klimenkov, H. Kuhlenbeck, H.-J. Freund, J. Vac. Sci. Technol. A, 17 (1999) 577.
[63] M. Klimenkov, S. Nepijko, H. Kuhlenbeck, M. Bäumer, R. Schlögl, H.J. Freund, Surf. Sci. 391 (1997) 27.
[64] M. Klimenkov, S. Nepijko, H. Kuhlenbeck, H.-J. Freund, Surf. Sci. 385 (1997) 66.
[65] G.K. Wertheim, Z. Phys. B 66 (1987) 53.
[66] G.K. Wertheim, S.B. DiCenzo, D.N.E. Buchanan, Phys. Rev. B 33 (1986) 5384.
[67] M.G. Mason, Phys. Rev. B 27 (1983) 748.
[68] M. Cini, M. De Crescenzi, F. Patella, N. Motta, M. Sastry, F. Rochet, R. Pasquali, A. Balzarotti, C. Verdozzi, Phys. Rev. B 41 (1990) 5685.
[69] V. Vijayakrishnan, C.N.R. Rao, Surf. Sci. Lett. 255 (1991) L516.
[70] I. Jirka, Surf. Sci. 232 (1990) 307.
[71] G.K. Wertheim, S.B. DiCenzo, S.E. Youngquist, Phys. Rev. Lett. 51 (1983) 2310.
[72] Y. Wu, E. Garfunkel, T.E. Madey, J. Vac. Sci. Technol. A 14 (1996) 1662.
[73] G.K. Wertheim, Phys. Rev. B 36 (1987) 9559.
[74] A. Sandell, J. Libuda, P.A. Brühwiler, S. Andersson, M. Bäumer, A.J. Maxwell, N. Mårtensson, H.-J. Freund, Phys. Rev. B. 55 (1997) 7233.
[75] A. Klekamp, E. Umbach, Surf. Sci. 284 (1993) 291.
[76] R.P. Eischens, W.A. Pliskin, S.A. Francis, J. Chem. Phys. 22 (1954) 1786.
[77] C. Goyhenex, M. Croci, C. Claeys, C.R. Henry, Surf. Sci. 352–354 (1996) 475.
[78] O. Krauth, G. Fahsold, A. Pucci, J. Chem. Phys. 110 (1999) 3113.
[79] J. Evans, B.E. Hayden, F. Mosselmans, A. Murray, Surf. Sci. 301 (1994) 61.
[80] J. Evans, G. Lu, B.E. Hayden, Surf. Sci. 360 (1996) 61.
[81] K. Coulter, X. Xu, D.W. Goodman, J. Phys. Chem. 98 (1994) 9242.
[82] K. Wolter, O. Seiferth, H. Kuhlenbeck, M. Bäumer, H.-J. Freund, Surf. Sci. 399 (1998) 190.
[83] M. Frank, R. Kühnemuth, M. Bäumer, H. J. Freund, Surf. Sci., 427–428 (1999) 288.
[84] U. Heiz, W.-D. Schneider, in: K.-H. Meiwes-Broer (Ed.), Cluster-Solid Surface Interaction, Springer, Berlin, 1999.
[85] D.R. Rainer, M.C. Wu, D.I. Mahon, D.W. Goodman, J. Vac. Sci. Technol. A 14 (1996) 1184.
[86] F.M. Hoffmann, Surf. Sci. Rep. 3 (1983) 107.
[87] B.E. Hayden, in: J.T. Yates Jr., T.E. Madey (Eds.), Methods of Surface Characterization, 1, Plenum Press, New York, 1987, p. 267.
[88] J. Heidberg, E. Kampshoff, O. Schönekäs, H. Stein, H. Weiss, Ber. Bunsenges. Phys. Chem. 94 (1990) 112.
[89] M. Frank, R. Kühnemuth, M. Bäumer, H. J. Freund, unpublished results.
[90] J.E. Crowell, J.G. Chen, J.T. Yates Jr., Surf. Sci. 165 (1986) 37.
[91] J.L. Erskine, R.L. Strong, Phys. Rev. B 25 (1982) 5547.
[92] F. Winkelmann, Ph.D. thesis, Ruhr-Universität Bochum, 1994.
[93] J.-P. Jacobs, S. Reijne, R.J.M. Elfrink, S.N. Mikhailov, H.H. Brongersma, M. Wuttig, J. Vac. Sci. Technol. A 12 (1994) 2308.
[94] H. Isern, G.R. Castro, Surf. Sci. 211/212 (1989) 865.
[95] A. Sandell, J. Libuda, P. Brühwiler, S. Andersson, A. Maxwell, M. Bäumer, N. Mårtensson, H.-J. Freund, J. Electron Spectrosc. Relat. Phenom. 76 (1995) 301.
[96] C.F. McConville, D.L. Seymour, D.P. Woddruff, S. Bao, Surf. Sci. 188 (1987) 1.
[97] S. Andersson, Ph.D. thesis, Uppsala University, 1998.
[98] R.M. Jaeger, J. Libuda, M. Bäumer, K. Homann, H. Kuhlenbeck, H.-J. Freund, J. Elect. Spect. Rel. Phen. 64/65 (1993) 217.
[99] F.S. Ohuchi, R.H. French, J. Vac. Sci. Technol. A 6 (1988) 1695.
[100] S. Stempel, Ph.D. thesis, Freie Universität, Berlin, 1998.
[101] R. Jaeger, Ph.D. thesis, Ruhr-Universität, Bochum, 1992.

[102] A.L. Diaz, W.W.C. Quigley, H.D. Yamamoto, M.E. Bussell, Langmuir 10 (1994) 1461.
[103] Th. Risse, H.-J. Freund, unpublished results.
[104] M. Adelt, S. Nepijko, W. Drachsel, H.-J. Freund, Chem. Phys. Lett. 291 (1998) 425.
[105] M. Zinke-Allmang, L.C. Feldman, M.H. Grabow, Surf. Sci. Rep. 16 (1992) 377.
[106] J.A. Venables, G.D.T. Spiller, M. Hanbücken, Rep. Prog. Phys. 47 (1984) 399.
[107] D.G.V. Campen, J. Hrbek, J. Phys. Chem. 99 (1995) 16389.
[108] C.R. Henry, C. Chapon, S. Giorgio, C. Goyhenex, in: R.M. Lambert, G. Pacchioni (Eds.), Chemisorption and Reactivity on Supported Clusters and Thin Films, NATO ASI Series E, 331, Kluwer, Dordrecht, 1997, p. 117.
[109] E. Bauer, Z. Kristallogr. 110 (1958) 372.
[110] S.H. Overbury, P.A. Bertrand, G.A. Somorjai, Chem. Rev. 75 (1975) 547.
[111] D. Chatain, L. Coudurier, N. Eustathopoulos, Rev. Phys. Appl. 23 (1988) 1055.
[112] C.H.F. Peden, K.B. Kidd, N.D. Shinn, J. Vac. Sci. Technol. A 9 (1991) 1518.
[113] K.H. Ernst, A. Ludviksson, R. Zhang, J. Yoshihara, C.T. Campbell, Phys. Rev. B 47 (1993) 13782.
[114] J.T. Stuckless, D.E. Starr, D.J. Bald, C.T. Campbell, J. Chem. Phys. 107 (1997) 5547.
[115] M. Bäumer, M. Frank, J. Libuda, S. Stempel, H.-J. Freund, Surf. Sci. 391 (1997) 204.
[116] M. Bäumer, J. Libuda, A. Sandell, H.-J. Freund, G. Graw, Th. Bertrams, H. Neddermeyer, Ber. Bunsenges. Phys. Chem. 99 (1995) 1381.
[117] M. Frank, R. Kühnemuth, M. Bäumer, H.-J. Freund, unpublished results.
[118] K.H. Hansen, T. Worren, S. Stempel, E. Lægsgaard, M. Bäumer, H.-J. Freund, F. Besenbacher, I. Stensgaard, submitted to Phys. Rev. Lett.
[119] Th. Hill, M. Mozaffari-Afshar, J. Schmidt, Th. Risse, S. Stempel, M. Heemeier, H.-J. Freund, Chem. Phys. Lett. 292 (1998) 524.
[120] J. Libuda, M. Bäumer, H.-J. Freund, J. Vac. Sci. Technol. A 12 (1994) 2259.
[121] F. Winkelmann, S. Wohlrab, J. Libuda, M. Bäumer, D. Cappus, M. Menges, K. Al-Shamery, H. Kuhlenbeck, H.-J. Freund, Surf. Sci. 307–309 (1994) 1148.
[122] Th. Bertrams, F. Winkelmann, Th. Uttich, H.-J. Freund, H. Neddermeyer, Surf. Sci. 331–333 (1995) 1515.
[123] S.A. Nepijko, M. Klimenkov, H. Kuhlenbeck, D. Zemlyanov, D. Herein, R. Schlögl, H.-J. Freund, Surf. Sci. 413 (1998) 192.
[124] S.A. Nepijko, M. Klimenkov, M. Adelt, H. Kuhlenbeck, R. Schlögl, H.J. Freund, Langmuir, in press.
[125] M. Bäumer, J. Biener, R.J. Madix, Surf. Sci., submitted for publication.
[126] N. Lopez, F. Illas, G. Pacchioni, J. Am. Chem. Soc. 121 (1999) 813.
[127] R. Kern, G. Le Lay, J.J. Metois, in: E. Kaldis (Ed.), Current Topics in Material Science, 3, North Holland, Amsterdam, 1979, p. 131.
[128] H.-J. Freund, B. Dillmann, D. Ehrlich, M. Haßel, R.M. Jaeger, H. Kuhlenbeck, C.A. Ventrice Jr., F. Winkelmann, S. Wohlrab, C. Xu, Th. Bertrams, A. Brodde, H. Neddermeyer, J. Mol. Catal. 82 (1993) 143.
[129] T.E. Madey, in: R.M. Lambert, G. Pacchioni (Eds.), Chemisorption and Reactivity on Supported Clusters and Thin Films, NATO ASI Series E, 331, Kluwer, Dordrecht, 1997, p. 105.
[130] M. Frank, R. Kühnemuth, M. Bäumer, H.-J. Freund, unpublished results.
[131] P. Hollins, Surf. Sci. Rep. 16 (1992) 51.
[132] H.F.J. van't Bilk, J.B.A.D. van Zon, T. Huizinga, J.C. Vis, D.C. Koningsberger, R. Prins, J. Am. Chem. Soc. 107 (1985) 3139.
[133] F. Solymosi, M. Pásztor, J. Phys. Chem. 89 (1985) 4789.
[134] A. Berkó, G. Ménesi, F. Solymosi, J. Phys. Chem. 100 (1996) 17732.
[135] P. Basu, D. Panayotov, J.T. Yates Jr., J. Phys. Chem. 91 (1987) 3133.
[136] H.P. Steinrück, F. Pesty, L. Zhang, T.E. Madey, Phys. Rev. B 51 (1995) 2457.
[137] J. Libuda, A. Sandell, M. Bäumer, H.-J. Freund, Chem. Phys. Lett. 240 (1995) 429.
[138] K. Wolter, O. Seiferth, J. Libuda, H. Kuhlenbeck, M. Bäumer, H.-J. Freund, Chem. Phys. Lett. 277 (1997) 513.

[139] B. Caprile, A.C. Levi, L. Liggieri, in: L. Pietronero, E. Tosatti (Eds.), Fractals in Physics, Elsevier, Amsterdam, 1986.
[140] K.-H. Meiwes-Broer, Appl. Phys. A 55 (1992) 430.
[141] R. Unwin, A.M. Bradshaw, Chem. Phys. Lett. 58 (1978) 58.
[142] A. Sandell, J. Libuda, P.A. Brühwiler, S. Andersson, A.J. Maxwell, M. Bäumer, N. Mårtensson, H.-J. Freund, J. Vac. Sci. Technol. A 14 (1996) 1546.
[143] K.S. Schönhammer, O. Gunnarsson, Solid State Commun. 23 (1977) 691.
[144] B.G. Frederick, G. Apai, T.N. Rhodin, J. Am. Chem. Soc. 109 (1987) 4797.
[145] O.D. Häberlen, S.-C. Chung, M. Stener, N. Rösch, J. Chem. Phys. 106 (1997) 5189.
[146] F. Ernst, Mater. Sci. Eng. R 14 (1995) 97.
[147] Z. Zhang, V.E. Henrich, Surf. Sci. 277 (1992) 263.
[148] J.-M. Pan, U. Diebold, L. Zhang, T.E. Madey, Surf. Sci. 295 (1993) 411.
[149] Y.S. Chaug, N.J. Chou, Y.H. Kim, J. Vac. Sci. Technol. A 5 (1987) 1288.
[150] S. Ogawa, S. Ichikawa, Phys. Rev. B 51 (1995) 17231.
[151] T.J. Sarapatka, J. Phys. Chem. 97 (1993) 11274.
[152] J. Libuda, M. Frank, A. Sandell, S. Andersson, P.A. Brühwiler, M. Bäumer, N. Mårtensson, H.-J. Freund, Surf. Sci. 384 (1997) 106.
[153] K.H. Johnson, S.V. Pepper, J. Appl. Phys. 53 (1982) 6634.
[154] G. Pacchioni, N. Rösch, J. Chem. Phys. 104 (1996) 7329.
[155] G. Pacchioni, N. Rösch, Surf. Sci. 306 (1994) 169.
[156] C. Verdozzi, D.R. Jennison, P.A. Schultz, M.P. Sears, Phys. Rev. Lett. 82 (1999) 799.
[157] C.R. Henry, C. Chapon, C. Duriez, J. Chem. Phys. 95 (1991) 700.
[158] I. Stara, V. Nehasil, V. Matolin, Surf. Sci. 365 (1996) 69.
[159] V.P. Zhdanov, B. Kasemo, J. Catal. 170 (1997) 377.
[160] C. Mottet, G. Tréglia, B. Legrand, Surf. Sci. 352–354 (1996) 675.
[161] C.R. Henry, C. Chapon, C. Goyhenex, R. Monot, Surf. Sci. 272 (1992) 283.
[162] S. Wohlrab, F. Winkelmann, J. Libuda, M. Bäumer, H. Kuhlenbeck, H.-J. Freund, in: R.J. MacDonald, E.C. Taglauer, K.R. Wandelt (Eds.), Surface Science: Principles and Current Applications, Springer, Berlin, 1996, p. 1.
[163] H. Steininger, S. Lehwald, H. Ibach, Surf. Sci. 123 (1982) 264.
[164] J.S. Luo, R.G. Tobin, D.K. Lambert, G.B. Fisher, C.L. DiMaggio, Surf. Sci. 274 (1992) 53.
[165] E.I. Altman, R.J. Gorte, Surf. Sci. 195 (1988) 392.
[166] D. Cappus, J. Klinkmann, H. Kuhlenbeck, H.-J. Freund, Surf. Sci. Lett. 325 (1995) L421.
[167] X. Guo, J.T. Yates Jr., J. Chem. Phys. 90 (1989) 6761.
[168] H. Cordatos, T. Bunluesin, R.J. Gorte, Surf. Sci. 323 (1995) 219.
[169] J.N. Andersen, E. Lundgren, R. Nyholm, unpublished.
[170] H. Antonsson, A. Nilsson, N. Mårtensson, I. Panas, P.E.M. Siegbahn, J. Electron Spectrosc. Relat. Phenom. 54/55 (1990) 601.
[171] E.W. Plummer, W.R. Salaneck, J.S. Miller, Phys. Rev. B 18 (1978) 1673.
[172] H. Tillborg, A. Nilsson, N. Mårtensson, J. Electron Spectrosc. Relat. Phenom. 62 (1993) 73.
[173] V. Fernandez, T. Gießel, O. Schaff, K.-M. Schindler, A. Theobald, C.J. Hirschmugl, S. Bao, A.M. Bradshaw, C. Baddeley, A.F. Lee, R.M Lambert, D.P. Woodruff, V. Fritzsche, Z. Phys. Chem. 198 (1997) 73.
[174] O. Björneholm, A. Nilsson, E.O.F. Zdansky, A. Sandell, B. Hernnäs, H. Tillborg, J.N. Andersen, N. Mårtensson, Phys. Rev. B 46 (1992) 10353.
[175] J. Libuda, Ph.D. thesis, Ruhr-Universität, Bochum, 1996.
[176] A. Ortega, Ph.D. thesis, Berlin, 1980.
[177] M. Tüshaus, W. Berndt, H. Conrad, A.M. Bradshaw, B. Persson, Appl. Phys. A 51 (1990) 91.
[178] M. Tüshaus, Ph.D. thesis, Berlin, 1990.
[179] A. Ortega, F.M. Hoffmann, A.M. Bradshaw, Surf. Sci. 119 (1982) 79.
[180] G. Chen, J.E. Crowell, J.T. Yates Jr., Surf. Sci. 187 (1987) 243.
[181] M. Frank, R. Kühnemuth, M. Bäumer, H.-J. Freund, unpublished results.
[182] M. Rebholz, R. Prins, N. Kruse, Surf. Sci. Lett. 259 (1991) L797.
[183] Y. Kim, H.C. Peebles, J.M. White, Surf. Sci. 114 (1982) 363.

[184] J.T. Yates Jr, E.D. Williams, W.H. Weinberg, Surf. Sci. 91 (1980) 562.
[185] M. Boudart, Adv. Catal. 20 (1969) 153.
[186] M. Frank, S. Andersson, J. Libuda, S. Stempel, A. Sandell, B. Brena, A. Giertz, P.A. Brühwiler, M. Bäumer, N. Mårtensson, H.-J. Freund, Chem. Phys. Lett. 279 (1997) 92.
[187] S. Andersson, M. Frank, A. Sandell, A. Giertz, B. Brena, P.A. Brühwiler, N. Mårtensson, J. Libuda, M. Bäumer, H.-J. Freund, J. Chem. Phys. 108 (1998) 2967.
[188] S. Andersson, M. Frank, A. Sandell, J. Libuda, B. Brena, A. Giertz, P.A. Brühwiler, M. Bäumer, N. Mårtensson, H.J. Freund, Vacuum 49 (1998) 167.
[189] R. Persaud, T.E. Madey, in: D.A. King, D.P. Woodruff (Eds.), Growth and Properties of Ultrathin Epitaxial Layers, Elsevier, Amsterdam, 1997, p. 407.
[190] M. Bäumer, J. Libuda, H.-J. Freund, in: R.M. Lambert, G. Pacchioni (Eds.), Chemisorption and Reactivity on Supported Clusters and Thin Films, NATO ASI Series E, 331, Kluwer, Dordrecht, 1997, p. 61.
[191] J.G. Chen, M.L. Colaianni, W.H. Weinberg, J.T. Yates Jr., Surf. Sci. 279 (1992) 223.
[192] S.T. Pantelides (Ed.), The Physics of SiO_2 and its Interfaces, Pergamon Press, New York, 1978.
[193] F. Rohr, M. Bäumer, H.-J. Freud, J.A. Meijas, V. Staemmler, S. Müller, L. Hammer, K. Heinz, Surf. Sci. 372 (1997) L291.
[194] R. Franchy, G. Schmitz, P. Gassmann, F. Bartolucci, Appl. Phys. A 65 (1997) 551.
[195] M.C. Wu, C.M. Truong, D.W. Goodman, Phys. Rev. B 46 (1992) 12688.
[196] J.S. Corneille, J.W. He, D.W. Goodman, Surf. Sci. 306 (1994) 269.
[197] F. Rohr, K. Wirth, J. Libuda, D. Cappus, M. Bäumer, H.-J. Freund, Surf. Sci. 315 (1994) L977.
[198] M. Ritter, W. Ranke, W. Weiß, Phys. Rev. B 57 (1998) 7240.
[199] Sh.K. Shaikhutdinov, W. Weiss, Surf. Sci. Lett., in press.
[200] M. Ritter, W. Weiss, Surf. Sci., in press.
[201] M. Henzler, Appl. Surf. Sci. 11–12 (1982) 450.
[202] M. Henzler, Appl. Phys. A 34 (1984) 205.
[203] J. Wollschläger, E.Z. Luo, M. Henzler, Phys. Rev. B 44 (1991) 13031.
[204] J. Wollschläger, Surf. Sci. 328 (1995) 325.
[205] H.-J. Güntherodt, R. Wiesendanger (Eds.), Scanning Tunneling Microscopy I, Springer Series in Surface Science, 20, Springer, Berlin, 1992.
[206] Th. Bertrams, Ph.D. thesis, Ruhr-Universität, Bochum, 1996.
[207] B.C. Gates, L. Guczi, H. Knözinger (Eds.), Metal Clusters in Catalysis, Studies in Surface Science and Catalysis, 29, Elsevier, Amsterdam, 1986.
[208] G.K. Wertheim, Z. Phys. D 12 (1989) 319.
[209] S.B. DiCenzo, G.K. Wertheim, Comments Solid State Phys. 11 (1985) 203.
[210] R.P. Eischens, S.A. Francis, W.A. Pliskin, J. Phys. Chem. 60 (1956) 194.
[211] X. Xu, P. Chen, D.W. Goodman, J. Phys. Chem. 98 (1994) 1245.
[212] K. Wolter, O. Seiferth, J. Libuda, H. Kuhlenbeck, M. Bäumer, H.-J. Freund, Surf. Sci. 402–404 (1998) 428.
[213] D.J. Dai, G.E. Ewing, J. Elect. Spect. Rel. Phen. 64/65 (1993) 101.
[214] J.G. Chen, J.E. Crowell, J.T. Yates Jr., Phys. Rev. B 33 (1986) 1436.
[215] R.L. Strong, J.L. Erskine, J. Vac. Sci. Technol. A 3 (1985) 1428.
[216] C. Berg, S. Raaen, A. Borg, J.N. Andersen, E. Lundgren, R. Nyholm, Phys. Rev. B 47 (1993) 13063.
[217] S. Andersson, P.A. Brühwiler, A. Sandell, J. Schnadt, L. Patthey, B. Brena, A. Giertz, N. Mårtensson, submitted for publication.
[218] M. Bäumer, S. Stempel, M. Heemeier, H.-J. Freund, to be published.
[219] J.B. Zhou, H.C. Lu, T. Gustafsson, E. Garfunkel, Surf. Sci. 293 (1993) L887.
[220] X. Xu, D.W. Goodman, Appl. Phys. Lett. 61 (1992) 1799.
[221] C.T. Campbell, A. Ludviksson, J. Vac. Sci. Technol. A 12 (1994) 1825.
[222] J.T. Stuckless, N.A. Frei, C.T. Campbell, Rev. Sci. Instrum. 69 (1998) 2427.
[223] A. Berkó, F. Solymosi, J. Catal., in press.
[224] P. Basu, D. Panayotov, J.T. Yates Jr., J. Am. Chem. Soc. 110 (1988) 2074.
[225] A. Sandell, J. Libuda, M. Bäumer, H.-J. Freund, Surf. Sci. 346 (1996) 108.

[226] M. Gausa, R. Kaschner, G. Seifert, J.H. Faehrmann, H.O. Lutz, K.-H. Meiwes-Broer, J. Chem. Phys. 104 (1996) 9719.
[227] S.-T Lee, G. Apai, M.G. Mason, R. Benbow, Z. Hurych, Phys. Rev. B 23 (1981) 505.
[228] V. de Gouveia, B. Bellamy, Y. Hadj Romdhane, A. Mason, M. Che, Z. Phys. D 12 (1989) 587.
[229] Ch. Kuhrt, M. Harsdorff, Surf. Sci. 245 (1991) 173.
[230] K.S. Schönhammer, O. Gunnarsson, Z. Phys. B 30 (1978) 297.
[231] D. Robba, D.M. Ori, P. Sangalli, G. Chiarello, L.E. Depero, F. Parmigiani, Surf. Sci. 380 (1997) 311.
[232] U. Diebold, H.-S. Tao, N.D. Shinn, T.E. Madey, Phys. Rev. B 50 (1994) 14474.
[233] U. Diebold, N.D. Shinn, Surf. Sci. 343 (1995) 53.
[234] J.T. Mayer, U. Diebold, T.E. Madey, E. Garfunkel, J. Elect. Spect. Rel. Phen. 73 (1995) 1.
[235] M. Gautier, J.P. Duraud, L. Pham, Van, Surf. Sci. Lett. 249 (1991) 327.
[236] B. Ealet, E. Gillet, Surf. Sci. 367 (1996) 221.
[237] T.J. Sarapatka, Chem. Phys. Lett. 212 (1993) 37.
[238] R.V. Kasowski, F.S. Ohuchi, R.H. French, Phys. B 150 (1988) 44.
[239] K. Nath, A.B. Anderson, Phys. Rev. B 39 (1989) 1013.
[240] I. Yudanov, G. Pacchioni, K. Neyman, N. Rösch, J. Phys. Chem. B 101 (1997) 2786.
[241] I.V. Yudanov, S. Vent, K. Neyman, G. Pacchioni, N. Rösch, Chem. Phys. Lett. 275 (1997) 245.
[242] A.V. Matveev, K.M. Neyman, G. Pacchioni, N. Rösch, Chem. Phys. Lett. 299 (1999) 603.
[243] A. Bogicevic, D.R. Jennison, in preparation.
[244] I. Jungwirthova, I. Stara, V. Matolin, Surf. Sci. 377–379 (1997) 644.
[245] V. Nehasil, I. Stara, V. Matolin, Surf. Sci. 377–379 (1997) 813.
[246] V.P. Zhdanov, B. Kasemo, Phys. Rev. Lett. 81 (1998) 2482.
[247] H. Kuhlenbeck, C. Xu, B. Dillmann, M. Haßel, B. Adam, D. Ehrlich, S. Wohlrab, H.-J. Freund, U.A. Ditzinger, H. Neddermeyer, M. Neuber, M. Neumann, Ber. Bunsenges. Phys. Chem. 96 (1992) 15.
[248] R. Wichtendahl, M. Rodriguez-Rodrigo, U. Härtel, H. Kuhlenbeck, H.-J. Freund, Surf. Sci. 427 (1999) 288.
[249] S. Ladas, H. Poppa, M. Boudart, Surf. Sci. 102 (1981) 151.
[250] I. Stará, V. Matolín, Surf. Sci. 313 (1994) 99.
[251] O. Björneholm, A. Nilsson, H. Tillborg, P. Bennich, A. Sandell, B. Hernnäs, C. Puglia, N. Mårtensson, Surf. Sci. 315 (1994) L983.
[252] H.-J. Freund, E.W. Plummer, Phys. Rev. B 23 (1981) 4859.
[253] A. Nilsson, O. Björneholm, E.O.F. Zdansky, H. Tillborg, N. Mårtensson, J.N. Andersen, R. Nyholm, Chem. Phys. Lett. 197 (1992) 1892.
[254] D.W. Goodman, Surf. Sci. 299–300 (1994) 837.
[255] D.N. Belton, S.J. Schmieg, Surf. Sci. 202 (1988) 238.
[256] F. Rohr, M. Bäumer, H.-J. Freund, J.A. Meijas, V. Staemmler, S. Müller, L. Hammer, K. Heinz, Surf. Sci. 389 (1997) 391.
[257] J.G. Chen, J.E. Crowell, J.T. Yates Jr., Phys. Rev. B 35 (1987) 5299.